2018

Thermo-Mechanical Coupling for Ablation

Rui Fu
University of Kentucky, coolfurui@gmail.com
Digital Object Identifier: https://doi.org/10.13023/ETD.2018.113

STUDENT AGREEMENT:

I represent that my thesis or dissertation and abstract are my original work. Proper attribution has been given to all outside sources. I understand that I am solely responsible for obtaining any needed copyright permissions. I have obtained needed written permission statement(s) from the owner(s) of each third-party copyrighted matter to be included in my work, allowing electronic distribution (if such use is not permitted by the fair use doctrine) which will be submitted to UKnowledge as Additional File.

I hereby grant to The University of Kentucky and its agents the irrevocable, non-exclusive, and royalty-free license to archive and make accessible my work in whole or in part in all forms of media, now or hereafter known. I agree that the document mentioned above may be made available immediately for worldwide access unless an embargo applies.

I retain all other ownership rights to the copyright of my work. I also retain the right to use in future works (such as articles or books) all or part of my work. I understand that I am free to register the copyright to my work.

REVIEW, APPROVAL AND ACCEPTANCE

The document mentioned above has been reviewed and accepted by the student's advisor, on behalf of the advisory committee, and by the Director of Graduate Studies (DGS), on behalf of the program; we verify that this is the final, approved version of the student's thesis including all changes required by the advisory committee. The undersigned agree to abide by the statements above.

Rui Fu, Student

Dr. Alexandre Martin, Major Professor

Dr. Haluk E. Karaca, Director of Graduate Studies

Thermo-Mechanical Coupling for Ablation

DISSERTATION

A dissertation submitted in partial
fulfillment of the requirements for
the degree of Doctor of Philosophy
in the College of Engineering at the
University of Kentucky

By
Rui Fu
Lexington, Kentucky

Director: Dr. Alexandre Martin, Professor of Mechanical Engineering

Lexington, Kentucky 2018

ABSTRACT OF DISSERTATION

Thermo-Mechanical Coupling for Ablation

In order to investigate the thermal stress and expansion as well as the associated strain effect on material properties caused by high temperature and large temperature gradient, a two-way thermo-mechanical coupling solver is developed. This solver integrates a new structural response module to the Kentucky Aerothermodynamics and Thermal response System (KATS) framework. The structural solver uses a finite volume approach to solve either hyperbolic equations for transient solid mechanics, or elliptic equations for static solid mechanics. Then, based on the same framework, a quasi-static approach is used to couple the structural response and thermal response to estimate the thermal expansion and stress within Thermal Protection System (TPS) materials.

To better capture the thermal expansion and study its impacts on material properties such as conductivity and porosity, a moving mesh scheme is also developed and incorporated into the solver. Grid deformation is transferred among different modules in the form of variations of geometric parameters and strain effects. By doing so, a bi-direction information loop is formed to accomplish the two-way strong thermo-mechanical coupling.

Results revealed that the thermal stress experienced during atmospheric re-entry concentrates in a banded area at the edge of the pyrolysis zone and its magnitude can be large enough to cause the failure of the TPS. In addition, thermal expansion causes the whole structure to deform and the changes in material properties. Results also indicated that the impacts coming from structural response should not be ignored in thermal response.

KEYWORDS: Thermo-mechanical coupling, atmospheric entry, thermal expansion, ablation, two-way coupling

Author's signature: Rui Fu

Date: March 6, 2018

Thermo-Mechanical Coupling for Ablation

By
Rui Fu

Director of Dissertation: Alexandre Martin

Director of Graduate Studies: Haluk E. Karaca

Date: March 6, 2018

Dedicated to my family.

ACKNOWLEDGMENTS

My greatest and deepest gratitude go to my dear supervisor, Dr. Alexandre Martin. It is my great honor and luck to be one of his students in computation science and TPS modeling. The story begins at a discussion on 'stress' as my research goal in one mysterious afternoon. Frankly speaking, at that moment I though it was some psychological terms. As my journey began at that time, I know little about this area and how to communicate with advisor. It is the patience and great care from Dr. Martin that enable me to keep on this journey. Furthermore, I want to appreciate his forgiveness on my frequent absence in our Lab. I am never a typical good student, but Dr. Martin understands my weird working time and we work very well. In addition, his strictness and academic attitudes toward research deeply surprised me as a young man. These experience, is invaluable for my future career either in academy or others.

I would like to thank Dr. James McDonough as my first supervisor for opening the door to numerical simulation. The experience and knowledge I obtained in his lectures as Numerical Analysis, Turbulence and Incompressible CFD are invaluable fortunes in my research. Also, the gratitude goes to my co-supervisor Dr. Jonathan Wenk. My first exposure to solid mechanics occurs at his course in Finite Element Method. In addition, I would like to thank the members of my doctorate committee, Dr. Kaveh A. Tagavi, Dr. Matthew J. Beck and Dr. Olivier Thibault. Their suggestion on the scope of my thesis helped a lot.

Also, special thanks goes to Dr. Haoyue Weng and Dr. Huaibao Zhang for their generous help on programming problems and the first introduction of our framework. I also wish to acknowledge my lab mates, Dr. Zhiyong Li, Raghava Davuluri, Ali Omidy, Umran Duzel, Olivia M. Schroeder, Chris Meek, Tingting Tang, Wenwei

Zeng, Justin M. Cooper, Christen Setters and Devin Sparks. For all the fun, humor, hard working and barbecue we shared together.

I want to thank my parents, Jimin Fu and Yan Wong for their never-ending support on my life since I was born. I am never a typical good kid, often making stupid mistakes. They will always be ready to forgive and love. The same thank to my cousins, uncles and grandparents as a big family for supporting me since I was a little kid.

I also want to thank for my beloved one, Jinjue Zhou as my confidant and spiritual therapist, driver and closest companion, lover and friend, mentor and intimate. Doing research is like walking on an endless journey to better truth. Most of the time, the hardest part is not the research itself, but the insistent attitude, the unremitting determination and a well-directed purpose. Those deep talks never fail to encourage me to face new problems; those laughter and sorrow always enlighten me to pull my self together; those happiness and positive thinking continue giving me power to conquer new challenges in life and work. We share both joy and pain, worries and happiness, loneliness and togetherness. You mean a lot to me and this work cannot be finished without you!

TABLE OF CONTENTS

LIST OF FIGURES

LIST OF TABLES

Nomenclature

Subscripts

c	char
n	relative to time step n
s	solid
v	virgin
ref	reference
T	transpose

Greek

β	degree of char
$\boldsymbol{\alpha}$	coefficient of thermal expansion (CTE), m/m·K
$\boldsymbol{\sigma}$	Cauchy stress tensor, N/m^2
$\boldsymbol{\varepsilon}$, $\boldsymbol{\varepsilon}_T$	strain and thermal strain tensors, m/m
λ	Second Lamé parameters, N/m^2
μ	First Lamé parameters, N/m^2
ν	Poisson's ratio
ρ	density, kg/m^3

Symbols

$\boldsymbol{f}$	body force per unit mass, N/kg
$\boldsymbol{n}$	normal vector of the computing face
$\boldsymbol{\mathcal{F}}$	vector of advective flux
$\boldsymbol{\mathcal{F}}_d$	vector of diffusive flux
$\boldsymbol{\mathcal{I}}$	identity matrix
$\boldsymbol{Q}$	vector of conservative variables

$\boldsymbol{R}$	sum of right hands side terms
$\boldsymbol{S}$	vector of source terms
$\boldsymbol{u}$	solid displacement vector, m
$\boldsymbol{v}$	solid velocity vector, m/s
$\boldsymbol{v}_g$	gas velocity vector, m/s
$\dot{q}''_w$	surface heat flux per unit area, W/m^2
E	Young's modulus, N/m^2
L^2	Euclidean norm
n	number of time step
p	pressure, N/m^2
s	number of time step between structural response updates
t	time, s
t_f	final time, s
x, y, z	spatial coordinates, m
A	area of the computing unit (face), m^2
V	volume of computing unit (cell), m^3

Chapter 1: Introduction

1.1 Motivation

Long before the first launch of rocket into sky, space exploration has been a magnet for human kind seeking ultimate knowledge, investigating the boundary of science, or simply make a better life for future generations. Nations, organizations and individuals are driven to make contributions to this remarkable journey. The process of exploration is slow but undoubtedly unremitting with the painful tragedy [1] and the exciting success of reusable rocket [2]. From the first rocket to the first satellite orbiting earth, the cooperation between nations and scientists keeps forward to the promise of a better world.

In this process, various branches of science and technologies have been boosted to an unparalleled level such as material science, chemistry and computer science, etc. In order to either harness more power from the chemical fuel, or withstand the heat produced during the atmospheric entry, many applications have been utilized to protect the structural integrity from extremely high temperature and radically elevated temperature gradient. At the same time, these applications must have reasonable weight to achieve a economic balance [3]. And the most important system that contributes to this task is the Thermal Protection System (TPS) [4].

Convergent-Divergent (CD) nozzle is another application where TPS technology is used [7]. In order to create high Mach flow field for experiments or powering payload, the converge part of nozzle first increases the pressure of the flow and then the flow to Mach 1 at the throat. The divergent part accelerates the flow to higher Mach number. To maintain a stable and precise Mach number, the wall of the chamber is coated with special material as a thermal protection layer [8]. It protects the nozzle from

aerodynamic heating and maintains a relatively low deformation ratio. In this case, the design of TPS must also consider the thermal expansion effects when choosing material as well as the high pressure may impact the nozzle walls [9]. Underestimating the thermal expansion will result in bias and errors in experiments and impairing the overall performance.

Another application can be found is the heat shield for atmospheric re-entry vehicles [10]. During the entry process, because of the extremely high velocity, the effect of aerodynamic heating can be catastrophic. At the surface of the vehicle, temperature can reach up to 3,000 K with a heat flux up to 1,000 W/cm^2 [11]. In this case, the TPS must first have extremely low conductivity to slower the energy transfer; then, it must maintain structural integrity under a large thermal stress introduced by temperature gradient [12]. In addition, TPS used by re-entry vehicles should be as light as possible so that more payload can be carried on for a space mission [13].

Although far more applications can be found as the utilization of TPS, this research will focus on the atmospheric entry vehicles.

1.1.1 Ablation

Generally speaking, there are two types of TPS, active and passive [14]. For active TPS, more complex cooling system is needed to keep the system at relatively low temperature [15]. The cooling system of internal combustion engine can be viewed as a type of active TPS [16]. Therefore, due to the complicated cooling components, the cost of the active cooling TPS is usually much higher than the passive one [17] and possibly less reliable compared to passive TPS.

Ablation is a mechanism used by passive thermal protection system. During ablation, the dynamic energy is transferred into heat, and at the same time, the ablative material itself is being burned and decomposed into char and pyrolysis gas [18]. In this process, large amount of heat is removed by chemical reactions and the payload

is protected by the TPS. Many recent space missions launched by NASA and Space-X used ablative materials as the key component of their heat shield [19]. To manufacture large TPS, ablative materials are normally assembled into tiles to form the whole heat shield and attached on the surface of the capsule [20].

The process of ablation raises a lot of problems on how to evaluate the thermo-mechanical performance of TPS. Under such extreme condition, the materials must first have low enough conductivity so that energy transfer is slowed [21]. Then, TPS material must have relatively low coefficient of thermal expansion (CTE) [22]. In addition, because of the unavoidable induced thermal stress, the material must have a high ultimate strength so that the structural integrity is maintained [23]. Finally, the properties of this TPS material, should be stable enough with respect to temperature and thermal expansion since these two factors are entwined closely during the entry process [24].

1.1.2 Thermal expansion and stress

Thermal expansion and induced stress are general phenomena can be observed in multiple facets of life. On any large bridge, for instance, there will be expansion joints built as buffer spaces for the thermal expansion [25]. The same design can be found on railway constructions [26]. Another example is the performance of internal combustion engine in cold temperature. In winter, the output of vehicle will be 'lagging' because metals are still in a contracting state so that a lot of spaces will undermine the sealings among different components [27]. The temperature changes in those examples are very limited with no more than 800 K (for automobile engine). With respect to TPS, much wider range of temperature is expected up to 3,000 K [28]. It is a must to carefully analyze the thermal expansion and stress in design and test stages.

The expansions and stresses result from the changes in temperature. Temperature

is the average of overall molecular kinetic energy of a substance. When an object is heated, the kinetic energy increases and results in more vibrations and movements of molecules. As a result, distances among the molecules become larger and the overall shape deforms [22]. Most natural materials have positive proportional thermal expansion coefficients, which means they expand under heating and contract under cooling. If this heated object is constraint by certain conditions, like contacting with a wall, the molecules react to each other and stress is then induced.

To study this thermally induced stress in TPS, this research will focus on numerical simulations for the fundamental equilibrium equations.

1.2 Literature review

1.2.1 Stress and thermal stress

Thermal processing on metal can be traced back to thousands of years [29]. At that time, there were no necessary tools to describe the real physics behind the performance of materials and forces. Cauchy presented the first rigorous model for stress in continuous solid media [30]. Based on that, several branches of solid mechanics had been formed for different kinds of stress analysis and applications, and they are still evolving.

The history of investigation on thermal stress can be dated back on 1835 by Duhamel on the temperature effects on elasticity problem [31]. He studied the formulations of elasticity with temperature as a variation parameter. Fueled by the Industrial Revolution, science related to thermal power has been booming. More and more analytical solutions have been found for specific geometries such as curved beam, rings and frames [22]. With the aid of modern computer and the evolution of numerical methods such as Finite Different Method (FDM), Finite Element Method (FEM) and Finite Volume Method (FVM), the realm of computation of thermal stress has expanded greatly to almost any geometry, with any boundary conditions [32]. The

problems, however, still remain unresolved for situations where a multi-physics coupling scenario with more than two sets of equations are coupled together, especially for the re-entry problem.

1.2.2 Structural response simulation

The mathematical foundation in solid mechanics is to solve either a set of elliptic partial different equations (PDEs) for static problems, or a set of hyperbolic PDEs for transient problems [22]. Among various numerical methods, Finite Element Method is in a dominant role in solid mechanics solvers [33]. Some of the most famous commercial FEM packages are ANSYS [34], COMSOL [35] and Nastran [36]. In this research, a large amount of verification cases are verified against ANSYS results.

The ability to couple different physics together for more complex problem varies in different packages. FEM calculates everything on node while the FVM on cell center. To perform a thermo-mechanical coupling analysis between different framework, interpolations are needed between cell nodes and cell centers. Consider the long physical time of a specific problem, errors can become large due to the multiple times of interpolations. Even within a same framework, the requirements of computational grid varies a lot due to different governing equations [37]. More discussions of the coupling schemes can be found in the following chapter.

More limitations prevent this research to use the FEM solver especially for the re-entry problem. Atmospheric entry involves hypersonic flow field and an in-depth material response. To do a fully coupled numerical modeling, all the relative modules need to be coupled together. In order to facilitate coupling with existing solvers, the structural response solver is developed in a FVM framework.

1.2.3 Thermo-mechanical coupling for ablation

To accurately model the mechanical performance of TPS during entry, a coupled thermo-mechanical solver is needed. The purposes of developing such solver is to estimate the magnitude and location of the thermal stress caused by temperature gradient. Dating back in 1960s, NASA has studied the thermal and mechanical performance of various ablator materials mainly through experiments [38]. At that time, measurements on the mechanical performance were very limited since the cost of the tests were not trivial. Attempts at calculating the thermal stress of the space shuttle orbiter wing skin panel were also conducted [39]. The main methods to estimate the thermal stress induced by temperature distribution were theoretical mathematical derivations and simplification to some specific geometries. As the power of modern computer became increasingly promising and economic, numerical studies were emerging on this topic. Wei H. Ng and Anthony M. Waas estimated the thermal stress of space shuttle using ABAQUS [40] and found out the magnitude of the maximum von Mises stress was around 500 MPa at the constrained underlying structure [41]. Due to the limits of the commercial code, no material response was involved and the impacts of thermal expansion were not considered.

During the ablation, the internal pressure produced by the produced pyrolysis gas may also have structural impacts. These impacts are rarely estimated. Similar studies, however, can be found in the theory of poroelasticity by Biot in his series of paper [42, 43]. In this study, a exploratory study will be presented to investigate the structural performance of the internal pressure produced by fluid within the porous media.

The effects of thermal expansion due to large temperature gradient can be disastrous. Experiments and numerical modeling show that the thermal expansion in less intense environment such as CD nozzle dose have impacts on the performance of the nozzle. In a study by Qiang and Shanyi Du et al., a more accurate estimation

of thermal expansion can lead to redesign of the structural and reduce the maximum stress by 14% [44]. In a lastest study for the HIPPO nozzle, Boyd et al. shows that neglecting thermal expansion can lead to large errors in evaluating the surface recession [45].

Another challenge is the previously mentioned material recession during ablation. TPS material not only expands because of the high temperature distribution, but also keeps losing material because of the shear stress and charring process. This nature of geometric deformation requires a solver to capture the expansion and at the same time, the surface recession. Such complex process has never been numerically studied before.

In thermo-mechanical coupling, it is also important to identify the approach of handling the information transferring between different modules. Usually, large variations of temperature and possible changes in density, information of temperature, density and all the geometric parameters such as face areas, relative distances and cell volumes are needed to be shared with structural response module. In one-way coupling, an uni-direction information transfer path, from thermal response to structural response, is used to simplify the simulation process. Details of this process will be presented in Chapter 3.

Unlike one-way coupling, two-way coupling features a bi-directional information transfer between different modules. This process usually does not gain popularity because of the complicated mathematical treatments and instability problems. It is, however, very useful for the situations where structural changes may result in large impacts on material properties and shapes of the objects. With respect to the ablation problem, the thermal expansion and strain effects on the material properties are changing the behaviors of material response. In this research, thermal expansion is captured with a moving mesh scheme and transferred back into the material response code. In addition, strain effects on conductivity will also be investigated based on a

linear relationship.

1.3 Structures of research

In Chapter 2, the mathematical foundation of thermo-mechanical coupling will be discussed with detailed governing equations and boundary-conditions. Then, the uniqueness of a solution for fully coupled problem is proved by mathematical derivations. Next, discussions on conditions where inertial and mechanical coupling terms can be neglected are provided, which leads to the framework of quasi-static framework.

In Chapter 3, verifications cases on the structural response are presented as well as the coupling case. Then, the developed framework will be applied to an ablation case to investigate the distribution of displacement and von Mises stress.

Chapter 6 shows the process of development of a 1D two-way thermo-mechanical solver. 1D code has many merits such as fast-prototyping and computationally cheap. The 1D code is then verified using ANSYS results to demonstrate the correct implementation. Followed by that, some preliminary results for strain effects on a heat conduction case are also provided.

Chapter 7 shows the development of a 3D fully coupled two-way strong thermo-mechanical solver. The verification process is conducted by cross-valiadation with the developed 1D solver and ANSYS result through a coupled heating case. Then, a series of test cases are presented to show how thermal expansion and strain effect impact on the performance of TPS.

Chapter 2: Thermo-mechanical Coupling

2.1 Introduction

Rapidly elevated temperature and extreme temperature gradient occur a large variety of engineering problems. In most cases, thermal deformations and stress are produced. Understanding these stresses is of significant importance to the safety and life of the materials and overall system. One typical example can be found is atmospheric entry process, where space vehicles suffer from extreme aerodynamic heating resulted from high-speed flight. Requirements on the materials can be complex for weight, porosity and conductivity. Moreover, safety is always the primary concern for overall system evaluation. To design such thermal protection system, accurate temperature distribution and possible thermal deformation must be carefully examined. Thus, it is crucial to investigate the relationship between these two closely entwined phenomena.

Although computer simulation and modeling currently dominate the early stages of research and development, it is crucial to understand the mathematical foundations behind these fancy tools. Otherwise, results and analysis provided by computational tool cannot be trustworthy and reliable. In order to obtain better understanding and more accuracy, mathematical foundations must be studied thoroughly. In this chapter, fundamental laws that governed the thermal dynamics and solid mechanics are investigated.

2.2 Fully coupled thermoelastic and uniqueness theorem

The fundamental equations used for a coupled thermo-mechanical problem can be derived from principles of solid mechanics and thermodynamics. It is very important to examine the equations, which will be solved simultaneously, with an unique existing

solution under a general conditions. This section serves as a mathematical foundation for the rest of the thesis.

2.2.1 Problem definition

Given a volume of arbitrary material in space $\mathbf{V}+\mathbf{B}$ with $\mathbf{B}$ as the boundary. Then, there exists at most one set of single-valued functions $\sigma_{ij}(\mathbf{x},t)$ and $\epsilon_{ij}(\mathbf{x},t)$ of class $C^{(1)}$, and $T(\mathbf{x},t)$ and $u_i(\mathbf{x},t)$ of class $C^{(2)}$, for $\mathbf{x}=(x_1,x_2,x_3)$ in $\mathbf{V}+\mathbf{B}$, $t\geq 0$, which satisfy the following equations as a complete coupled thermo-mechanical problem for $\mathbf{x}$ in $\mathbf{V}$, $t\geq 0$:

$$kT_{mm} = \rho c\dot{T} + mT_0\dot{\epsilon}_{kk} \tag{2.1a}$$

$$\sigma_{ij,j} = \rho\ddot{u}_i \tag{2.1b}$$

and with the strain equation and stress-strain relation for $\mathbf{x}$ in $\mathbf{V}$, $t\geq 0$,

$$\epsilon_{ij} = \frac{1}{2}(u_{i,j}+u_{j,i}) \tag{2.2a}$$

$$\sigma_{ij} = \delta_{ij}\lambda\epsilon_{kk} + 2\mu\epsilon_{ij} - \delta_{ij}m(T-T_0) \tag{2.2b}$$

with boundary conditions for $\mathbf{x}$ on $\mathbf{B}$, $t>0$,

$$T = T_{bc}(\mathbf{x},t) \tag{2.3a}$$

$$u_i = U_{i,bc}(\mathbf{x},t) \tag{2.3b}$$

and with initial conditions for $\mathbf{x}$ in $\mathbf{V}$, $t=0$,

$$T = T_{ic}(\mathbf{x},t) \tag{2.4a}$$

$$u_i = U_{i,ic}(\mathbf{x},t) \tag{2.4b}$$

$$\dot{u}_i = \dot{U}_{i,ic}(\mathbf{x},t) \tag{2.4c}$$

where the quantities k, c, ρ, $3\lambda+2\mu$, $m=(3\lambda+2\mu)\alpha$ and T_0 are all positive. All the initial and boundary condition functions are known. A function, for instance,

$u(x_1, x_2, \cdots, x_n)$ is said to be continuous of class $C^{(n)}$ if the function itself and all its partial derivatives of order up to and including n are continuous functions of $(x_1, x_2, \cdots, x_n)$.

Problem proof

Assuming there exists two different such sets of functions, $\sigma_{ij}^{(1)}$ and $\sigma_{ij}^{(2)}$, $\epsilon_{ij}^{(1)}$ and $\epsilon_{ij}^{(2)}$ etc., and introduce the difference functions as,

$$\sigma_{ij}^* = \sigma_{ij}^{(1)} - \sigma_{ij}^{(2)} \tag{2.5a}$$

$$\epsilon_{ij}^* = \epsilon_{ij}^{(1)} - \epsilon_{ij}^{(2)} \tag{2.5b}$$

$$u_i^* = u_i^{(1)} - u_i^{(2)} \tag{2.5c}$$

$$T^* = T^{(1)} - T^{(2)} \tag{2.5d}$$

Because of the linearity of the problem, these difference functions should also satisfy Eqs. 2.1 to Eqs. 2.2a and the homogeneous counterpart of Eqs. 2.2b to Eqs. 2.4. In the next few paragraphs, detailed derivations will be provided to show that, with certain amount of mathematical transformation, these differential terms can only be zero, which is the proof of an uniqueness solution.

Starting with the integral from of Eqs. 2.29a,

$$\int_V kT_{mm}^* \, dV = \int_V \rho c \dot{T}^* \, dV + \int_V mT_0 \dot{\epsilon}_{kk}^* \, dV \tag{2.6}$$

For both hand sides, multiply with T^*,

$$\int_V kT^* T_{mm}^* \, dV = \int_V \rho c T^* \dot{T}^* \, dV + \int_V mT_0 T^* \dot{\epsilon}_{kk}^* \, dV \tag{2.7}$$

the left hand side can be construct with additional term as,

$$\int_V kT^* T_{mm}^* \, dV + \int_V kT_m^* T_m^* \, dV = \int_V (kT^* T_m^*)_m \, dV \tag{2.8}$$

The right hand side, by employing divergence theorem, becomes,

$$\int_V (kT^*T^*_m)_m \, dV = \int_B kT^*T^*_m n_m \, dA \tag{2.9}$$

Since T^* on boundary is 0, thus,

$$\int_V (kT^*T^*_m)_m \, dV = \int_B kT^*T^*_m n_m \, dA = 0 \tag{2.10}$$

Thus, the Eqs. 2.6 can be written as

$$\int_V \rho c T^* \dot{T}^* \, dV + \int_V m T_0 T^* \dot{\epsilon}^*_{kk} \, dV + \int_V k T^*_m T^*_m \, dV = 0 \tag{2.11}$$

The first term on left hand side can further be re-written as,

$$\int_V \rho c T^* \dot{T}^* \, dV = \frac{\rho c}{2} \int_V \frac{\partial}{\partial t} T^{*2} \, dV \tag{2.12}$$

the Eqs. 2.29a, combined with boundary condition Eqs. 2.3a, is derived as,

$$\frac{\rho c}{2} \int_V \frac{\partial}{\partial t} T^{*2} \, dV + \int_V m T_0 T^* \dot{\epsilon}^*_{kk} \, dV = - \int_V k T^*_m T^*_m \, dV \tag{2.13}$$

Next, the second term on the left hand side must be derived with a form of square function to complete this proof. Let T_0 be 0 and multiply the Eqs. 2.2b with $\dot{\epsilon}^*_{kk}$ in integral form as,

$$\int_V \sigma^*_{ij} \dot{\epsilon}^*_{ij} \, dV = \int_V \delta_{ij} \lambda \epsilon^*_{kk} \dot{\epsilon}^*_{ij} \, dV + \int_V 2\mu \epsilon^*_{ij} \dot{\epsilon}^*_{ij} \, dV - \int_V \delta_{ij} m T^* \dot{\epsilon}^*_{ij} \, dV \tag{2.14}$$

For the first left term in the above equation, it can be re-written in terms of time derivative of displacement as,

$$\int_V \sigma^*_{ij} \dot{\epsilon}^*_{ij} \, dV = \int_V \sigma^*_{ij} \dot{u}^*_{i,j} \, dV = \int_V \left[(\sigma^*_{ij} \dot{u}^*_i)_{,j} - (\sigma^*_{ij,j} \dot{u}^*_i) \right] dV \tag{2.15}$$

For the first term in the right hand side, by utilizing the divergence theorem and the boundary condition Eqs. 2.3b, it can be written as,

$$\int_V (\sigma^*_{ij} \dot{u}^*_i)_{,j} \, dV = \int_B \sigma^*_{ij} \dot{u}^*_i n_j \, dA = 0 \tag{2.16}$$

And to derive the second term on the right hand side, using the equilibrium equation, in a square form as,

$$\int_V \sigma^*_{ij,j}\dot{u}^*_i \, dV = \int_V \rho\ddot{u}^*_i\dot{u}^*_i \, dV = \int_V \frac{\partial}{\partial t}(\frac{1}{2}\rho\dot{u}^*_i\dot{u}^*_i) \, dV \tag{2.17}$$

Then, the Eqs. 2.15 can be written as,

$$\int_V \sigma^*_{ij}\dot{\epsilon}^*_{ij} \, dV + \int_V \frac{\partial}{\partial t}(\frac{1}{2}\rho\dot{u}^*_i\dot{u}^*_i) \, dV = 0 \tag{2.18}$$

To complete the whole derivation, the alternative form of stress and strain tensor in terms of mean and deviatoric components are introduced,

$$s_{ij} = \sigma_{ij} - \delta_{ij}\sigma \tag{2.19a}$$

$$e_{ij} = \epsilon_{ij} - \delta_{ij}\epsilon \tag{2.19b}$$

where s_{ij} represents stress tensor, e_{ij} represents the strain tensor, $\sigma = \frac{1}{3}\sigma_{ii}$ and $\epsilon = \frac{1}{3}\epsilon_{ii}$. Using the Eqs. 2.19, the first term in Eqs. 2.18 can be written as,

$$\int_V \sigma^*_{ij}\dot{\epsilon}^*_{ij} \, dV = \int_V 3\sigma^*\dot{\epsilon}^* \, dV + \int_V s^*_{ij}\dot{e}^*_{ij} \, dV \tag{2.20}$$

With an additional relationship between the mean value of stress and strain as,

$$\sigma = (3\lambda + 2\mu)[\epsilon - \alpha(T - T_0)] \tag{2.21}$$

Remove T_0 as a constant and with $s_{ij} = 2\mu e_{ij}$, the Eqs. 2.20 can be written as,

$$\int_V \sigma^*_{ij}\dot{\epsilon}^*_{ij} \, dV = \int_V 3(3\lambda + 2\mu)\epsilon^*\dot{\epsilon}^* \, dV + 2\mu e^*_{ij}\dot{e}^*_{ij} - \int_V mT^*\dot{\epsilon}^*_{kk} \, dV \tag{2.22}$$

Combine with the Eqs. 2.18, the final form is,

$$\int_V \{\frac{\partial}{\partial t}\left[\frac{3}{2}(3\lambda + 2\mu)\epsilon^{*2} + \mu e^*_{ij}e^*_{ij} + \frac{1}{2}\rho\dot{u}^*_i\dot{u}^*_i\right] - mT^*\dot{\epsilon}^*_{kk}\} \, dV = 0 \tag{2.23}$$

Rewrite the Eqs. 2.13 as,

$$\frac{\rho c}{2}\int_V \frac{\partial}{\partial t}T^{*2} \, dV + \int_V mT_0T^*\dot{\epsilon}^*_{kk} \, dV = -\int_V kT^*_{,m}T^*_{,m} \, dV \tag{2.24}$$

By dividing the above equation by T_0, and substituting $mT^*\dot{\epsilon}^*_{kk}$, the equation of all the combined terms becomes,

$$\frac{\partial}{\partial t}\int\limits_V \left\{\frac{3}{2}(3\lambda+2\mu)\epsilon^{*2}+\mu e^*_{ij}e^*_{ij}+\frac{1}{2}\rho\dot{u}^*_i\dot{u}^*_i+\frac{\rho c}{2T_0}T^{*2}\right\}dV=-\frac{k}{T_0}\int\limits_V T^*_{,m}T^*_{,m}\,dV \quad (2.25)$$

Since all the differential terms are initially zero according to the initial condition, the time derivative can only be zero or positive. The right hand side, however, indicates that the value must be zero or negative since k and T_0 are positive. With this reasoning and inequality, the left hands side must be zero.

$$\frac{\partial}{\partial t}\int\limits_V \left\{\frac{3}{2}(3\lambda+2\mu)\epsilon^{*2}+\mu e^*_{ij}e^*_{ij}+\frac{1}{2}\rho\dot{u}^*_i\dot{u}^*_i+\frac{\rho c}{2T_0}T^{*2}\right\}dV=0,\ (t\geq 0) \quad (2.26)$$

Thus, all the differential terms must remain zero for the whole set of equations for all time. By proving the uniqueness of the coupled solutions, it is now ensured that the results from numerical simulation based on these equations are unique.

2.3 Discussion of a fully coupled formulation

In order to examine the behaviors of a coupled thermoelastic solution for possible simplification, a complete solution is presented. The solution comes from the classic textbook Theory of Thermal Stress [22]. Consider a bar of arbitrary material, initially at rest and at a uniform temperature. This bar is subjected to a prescribed internal heat of generation, $Q(x,t)$ per unit volume given by,

$$Q(x,t)=Q_0(t)cos(x/L) \quad (2.27)$$

where L represents the length of this bar. Constrains are imposed as,

$$u=u(x,t), \quad (2.28a)$$

$$v=w=0 \quad (2.28b)$$

u are displacement and T is temperature as primitive variables. The set of equations for a complete coupled thermoelastic problem can be written as,

$$k\frac{\partial^2 T}{\partial x^2} - \rho c_v \frac{\partial T}{\partial t} - \underbrace{(3\lambda + 2\mu)\alpha_1 T_0 \frac{\partial^2 u}{\partial x \partial t}}_{\text{mechanical coupling}} + Q = 0 \tag{2.29a}$$

$$(\lambda + 2\mu)\frac{\partial^2 u}{\partial x^2} - \underbrace{\rho \frac{\partial^2 u}{\partial t^2}}_{\text{inertial effects}} - (3\lambda + 2\mu)\alpha_2 \frac{\partial T}{\partial x} = 0 \tag{2.29b}$$

where k is conductivity, ρ is density, c_v is heat capacity, λ and μ are Lamé parameters, α_1 and α_1 are coefficients of thermal expansion. It should be noted that in a full coupling problem, both the mechanical coupling and inertial effects are taken into account. To better investigate the mathematical behavior, dimensionless forms of a list of parameters will be given. The solutions of displacement and temperature are,

$$u/L = \rho c_v/[\alpha(3\lambda + 2\mu)]F(\tau)sin(x/L) \tag{2.30a}$$

$$T/T_0 = G(\tau)cos(x/L) \tag{2.30b}$$

The following dimensionless parameters are also defined,

$$\tau = \frac{kt}{\rho c L^2} \tag{2.31a}$$

$$\delta = \frac{(3\lambda + 2\mu)^2 \alpha_1 \alpha_2 T_0}{(\lambda + 2\mu)\rho c_v} \tag{2.31b}$$

$$K = \frac{k}{L\rho c_v v_e} \tag{2.31c}$$

$$v_e = \sqrt{(\lambda + 2\mu)\rho} \tag{2.31d}$$

Where τ represents the time and v_e the solid velocity. δ is a parameter can be used to measure the extent of coupling. K is a coefficient to measure the thermal characteristic time versus the structural characteristic time.

2.4 Mechanical coupling in heat conduction

The mechanical coupling term in the heat conduction equation can capture strain-induced temperature rise. Consider an elastic steel bar being periodically pulled and

compressed. Usually this process results in an increase of entropy and energy in a mechanically irreversible process. This phenomenon is known as thermoelastic dissipation. The mechanical coupling term, thus, plays essential role in this kind of problem. However, if the strains and deformation are caused by non-uniform temperature distribution, the deformation should not have large impact on the temperature for most scenario. In such condition, the mechanical coupling term may be ignored.

With the definition of coupling parameter δ in Eqs. 2.31b, the heat equation may be re-written as,

$$k\frac{\partial^2 T}{\partial x^2} = \rho c_v \frac{\partial T}{\partial t}\left[1 + \underbrace{\delta(\frac{\lambda+2\mu}{3\lambda+2\mu})(\frac{\partial\epsilon/\partial t}{\alpha_1 \frac{\partial T}{\partial t}})}_{\text{mechanical coupling}}\right] + Q \tag{2.32}$$

If the value of coupling term is much less than unit, it is then negligible. The inequality is rewritten and provided as,

$$\frac{\dot{\epsilon}}{3\alpha_1 \dot{T}} \ll (\frac{\lambda+2\mu/3}{\lambda+2\mu})\frac{1}{\delta} \tag{2.33}$$

Setting $T_0 = 366$ K as environmental temperature and using the properties listed in Table 2.1, The value of δ can be calculated $\delta = 0.014$, thus, the value of coupling

Table 2.1: Steel Properties

Density, kg/m^3	Young's modulus, N/m^2	Poisson ratio
7850	2×10^{11}	0.3
Conductivity, W/(m· K)	Specific heat, J/(kg· K)	Coef. of thermal exp., m/(m·K)
60.5	434	12×10^{-6}

term will be very small if, approximately,

$$\frac{\dot{\epsilon}}{3\alpha_1 \dot{T}} \ll 50 \tag{2.34}$$

It should be noted that since the driving force of thermal strain is the non-uniform temperature distribution, it is safe to argue that the time rate of change of strain should be the same order as the time rate of change of temperature, which indicates

the following inequality as,

$$\dot{\epsilon} \simeq \alpha \dot{u} \simeq \alpha \dot{T} \tag{2.35}$$

The previous discussion makes it clear that the value of δ can be an indicator as a threshold value for whether or not the mechanical coupling should be taken into account for an temperature-driven thermal stress analysis. Generally, if $\delta \ll 1$, it is unnecessary to consider the mechanical coupling term in a thermo-mechanical coupling analysis.

2.5 Inertial term in equilibrium

The inertial term in the equilibrium can be tricky to handle numerically since it is a second order derivative with respect to time. Therefore, it is necessary to discuss the conditions when this term can be neglected. It should be noted that the time rate of change of temperature is generally slow compare to the dilitational waves and the time rate of change of displacement. Some important issues were studied thoroughly by Boley [22]. Thus, a quick summary will be provided to show the criterion for the elimination of inertial term in practical applications.

Consider a bar with length L is being heated by a constant heat flux. An arbitrary point P, where $0 < P < L$, has been chosen as a study position. At $t = t_1$, a thermo-mechanical expansion wave, caused by the initial heating of the surface, reaches at point P. This point will first be compressed and then relieve stress due to the expansion wave, and finally become tensile. To assess how strong the expansion wave, which represents the inertial effects, some dimensionless parameters are introduced as,

$$t_M = \frac{L}{v_e} \tag{2.36a}$$

$$t_T = \frac{L^2}{\kappa} \tag{2.36b}$$

$$H = \frac{\kappa h}{v_e k} \tag{2.36c}$$

where t_M represents the characteristic mechanical time and t_T the characteristic thermal time. κ is thermal diffusivity and H can be viewed as a ratio of mechanical time and thermal time, which will be discussed in greater length later. For steel, it is easy to observe that,

$$t_T \gg t_M \tag{2.37}$$

The above inequality indicates that the mechanical expansion waves respond much faster and reach its static state. That is one of the criterion can be used to assert the ignorance of inertial effect. Another one is the value of H. With no geometric irregularities such as holes or cracks, the maximum value of thermal stress can be written as,

$$\sigma_{xx,max} = -\frac{E\alpha\triangle T}{1-2v} \tag{2.38}$$

where E and v are Young's modulus and Poisson ratio. The absolute value of the change $\triangle\sigma$ caused by inertial effects can be related to the max stress, according to the Poisson effects, as

$$\triangle\sigma = v\left|\frac{E\alpha\triangle T}{1-2v}\right| = \frac{v}{1-2v}|\sigma| \tag{2.39}$$

For the solution of a fully coupled approach, as depicted in Ref. [22], for $H < 1$,

$$|\sigma| < \frac{H}{1-H} \tag{2.40}$$

Therefore, for this range of H, the possible maximum disturbance caused by inertial is

$$|\sigma| < \left(\frac{v}{1-2v}\right)\frac{H}{1-H} \tag{2.41}$$

For steel, it takes a value of 3×10^{-5}. With such small value, the cost of ignoring the inertial effects in the thermo-mechanical coupling is extremely small. For a heating-driven problem, the values of H and $\dfrac{t_M}{t_T}$ should be carefully examined to evaluate the importance of the inertial term.

2.6 Quasi-static thermo-mechanical coupling

Based on the preceding analysis, the effects of the mechanical coupling terms of energy equation and inertial terms of equilibrium equation can be neglected for a wide range of thermo-mechanical coupling problems.

2.6.1 Formulations and uniqueness

The simplified formulations for a 1D thermo-mechanical coupling problem are presented as,

$$k\frac{\partial^2 T}{\partial x^2} - \rho c_v \frac{\partial T}{\partial t} + Q = 0 \tag{2.42a}$$

$$(\lambda + 2\mu)\frac{\partial^2 u}{\partial x^2} - (3\lambda + 2\mu)\alpha\frac{\partial T}{\partial x} = 0 \tag{2.42b}$$

It should be noted that since the coupled equations have been simplified to two "separated" equations, the uniqueness of each equation can be guaranteed by the theory of partial differential equation (PDE). Those proof are straightforward and can be found in any classic PDE textbook.

2.6.2 Analytic solutions and remarks

With specific boundary condition and initial conditions mentioned before, an analytic solution can be found in Boley [22] as,

$$\frac{T(\tau)}{cos(x/L)}\left[\frac{k}{Q_0 L^2}\right] = 1 + \frac{e^{-\tau} - \tau_0 e^{-\tau/\tau_0}}{\tau_0 - 1} \tag{2.43a}$$

$$\frac{u(\tau)}{sin(x/L)}\left[\frac{(\lambda + 2\mu)k}{(3\lambda + 2\mu)Q_0 L^3 \alpha}\right] = 1 + \frac{e^{-\tau} - \tau_0 e^{-\tau/\tau_0}}{\tau_0 - 1} \tag{2.43b}$$

Several remarks should be noted for the above formulations and solutions. The first one is that by ignoring the inertial terms in equilibrium equation, there is no time derivative term in this equation, and this is the origin where the "quasi-static"

terminology comes from. The second observation is that although there is no time derivative of displacement, the solution is still time depend as $u(x, \tau)$ because of the time dependency of temperature distribution. This observation is important when investigating the ablation cases and two-way coupling.

Since displacement and stress are treated as quasi-static solutions, a question of when they should be calculated arises. The severeness of the variation in material properties and rapid temperature distribution both contribute to a rapid changes in stress distribution. Thus, in practical application, the frequency of updating the solution for $u(x, \tau)$ must be carefully examined.

2.7 General remarks and summary

Although various types of analytic solutions regarding the thermo-mechanical problem can be found with certain boundary conditions and initial conditions, in most practical problem, due to the temperature-dependent material properties, deforming shape and other factors, it is impossible to obtain an analytic solution. Therefore, with the power of modern high performance computer, such coupling problems have to be solved using numerical methods, such as Finite Element Method, Finite Difference Method or Finite Volume Method. In this study, the finite volume method is chosen for the framework of the numerical scheme. Because of the coupling needs, detailed formulations and discretization approach will be presented in later chapters.

Chapter 3: Thermo-mechanical One-way Coupling

3.1 Introduction

During hypersonic planetary entry, vehicles are exposed to extreme aerodynamic heating. To protect the payload, Thermal Protection Systems (TPS) are employed [46]. Modern TPS use low density ablative materials to effectively reduce the heat rate applied to the spacecraft through phase change and chemical phenomena, such as pyrolysis and ablation [47]. These two effects have been studied and modeled extensively since the 1960s. However, another ablation phenomenon, spallation, occurs when porous ablative materials are subjected to high enthalpy flows [48, 49, 50]. This phenomenon can be described as the ejection of material particles into the flow field. The particle ejection can lead to the formation of grooves which escalates aerodynamic heating, accelerates material recession and weakens the integrity of the TPS [51]. Material failures and catastrophic loss can be triggered by this process. It is also speculated that the ejected particles, traveling in high temperature regions of the flow, might block the radiative heating generated by the shock, and therefore reduce the energy reaching the surface [52]. The mechanisms that cause spallation are not well understood. For aerothermodynamic ablation, current state of the art techniques account for this process by multiplying the thermochemical ablation rate by a factor [53]. This correlation assumes that the thermochemical ablation is linked to spallation, which is not necessarily a bad assumption. However, there is clearly a need to better understand the spallation phenomenon.

One possible cause of spallation is material failure at the micro-scale resulting from exceeding the material stress limit. TPS are usually manufactured using a carbon

fiber reinforcement [54, 55, 4]. For most materials, their integrity is maintained when the mechanical stress is less than a certain threshold value (500 MPa for crossply carbon-fiber composites, for instance [56]). Once this stress limit has been exceeded, micro fractures appear on the fiber scale, leading to material failure. Numerous studies have been published on the mechanical behavior of porous ablators. One such study [57, 58] focuses on the fracture testing of virgin and charred PICA. It was observed that cracks were initiated and grew when a critical stress limit had been reached, separating the carbon fibers from the binder. Thus, it is reasonable to assert that spallation is a series of micro-fiber fractures caused by exceeding the material strength limit. The stress acting on the fiber resulted from a combination of thermal strain, internal pressure and shear stress of both flow field and pyrolysis gas blowing. Therefore, to correctly predict the leading factors of spallation and failure of the TPS, it is critical to accurately model both the distributions and magnitudes of stresses within materials in a strongly coupled approach.

High temperature gradients are not the only source of stress inside TPS materials. The complexity of this problem increases as chemical reactions and surface blowing is considered [59]. These two factors are entwined within the ablation process, resulting in density changes and production of pyrolysis gas [60, 61]. Transformation of TPS materials by chemical reactions results in radical changes in properties such as Young's modulus and the coefficient of thermal expansion (CTE). Transport of pyrolysis gas not only changes the temperature field, but also leads to internal pressure which can cause stress concentrations [62].

During re-entry, the extremely high temperatures cause the TPS to expand so that strain rate effects cannot be ignored [63]. This non-uniform distribution of temperature causes a non-uniform expansion, which in turn, can alter the material properties such as permeability, porosity and conductivity [64]. Moreover, if the variability of material properties is considered, thermal strain can cause local defects

that can lead to spallation.

Although extensive numerical studies have focused on the mechanism of ablation [49, 65, 66, 67, 68, 69] and chemical pyrolysis gas transport [70, 71, 72, 73], the ability to couple material response to structural response has only been briefly explored [74, 68]. Solid mechanical solvers are usually only coupled with heat conduction, and material changes and internal pressure within the material are not taken into account. Moreover, the effects of the structural response are not considered in thermal response solvers.

In solid mechanics modeling, the Finite Element Method (FEM) dominates both academia and industry, with popular codes such as ANSYS Mechanical [34] and Abaqus [40]. These commercial codes have been proven to be accurate and efficient for both static and dynamic problems. However, most hypersonic aerothermodynamics and material response codes use a different approach, which leads to difficulties in coupling schemes. Some hybrid methods have yielded satisfactory results, such as the Control Volume Finite Element Method (CVFEM) [75]. This method adapts a finite volume mesh and extracts nodes for computing [76]. However, the interpolations between computing units, cell center and grid node, are inevitable for a coupling scheme if a mixed finite volumes and finite elements are used. This situation may result in a lower computational efficiency and possible numerical errors. The use of a pure Finite Volume Method (FVM) has also been utilized to solve solid mechanics problems. Bijelonja and Demirdzic [77] proposed such an approach for the linear elasticity problem. The same approach was also used for coupled thermo-mechanical stress analysis, on a moving mesh [78]. To validate the approach, Fallah et al. [79, 80] offered comparisons of FEM and FVM results for different geometries and stress analysis. All of these studies demonstrated that FVM has equal accuracy, while being much simpler to implement mathematically and numerically.

The present work proposes a method of coupling multi-physics models for ablation

simulation, and investigates links between the distribution of stress and ablation phenomena. A structural response solver is developed using a Finite Volume Method. This method is chosen to facilitate the coupling with a FVM-based material response code, so that both codes can share the same structure and computational grid. The structural response code is capable of both static and transient problems such as vibrations. In this study, a quasi-static coupling strategy [81] is utilized for coupling both codes.

The following sections describe the numerical framework used to discretize the governing equations with related mathematical models. Then, a series of verification test cases are presented to demonstrate that the models are correctly and accurately implemented. Finally, a coupled thermo-mechanical test case for a 2D charring ablator sample is presented.

3.2 Governing equations and numerical implementation

3.2.1 Numerical framework

The solid mechanics and material response codes have both been developed within the Kentucky Aerothermodynamic and Thermal-response System (KATS) framework [70, 71, 72]. KATS has been used to solve hypersonic flows [48, 82], low-speed turbulent flows [83, 84], and material response [71, 70]. KATS is designed for massively parallellized computations, utilizing ParMETIS [85] for domain decomposition and openMPI [86] as the message passing interface. In KATS, the general time-dependent partial differential equations are written in the following form

$$\frac{\partial \boldsymbol{Q}}{\partial t} + \nabla \cdot (\boldsymbol{\mathcal{F}} - \boldsymbol{\mathcal{F}}_d) = \boldsymbol{S}\,, \tag{3.1}$$

where $\boldsymbol{Q}$ represents the conservative variables, $\boldsymbol{\mathcal{F}}$ the advective fluxes, $\boldsymbol{\mathcal{F}}_d$ the diffusive fluxes, and $\boldsymbol{S}$ represents the source terms. The system of equations is integrated over a cell volume, and spatially discretized. The resulting linear system is solved iteratively

for the whole domain, using an implicit backward Euler scheme

$$\left[\frac{V}{\Delta t}\boldsymbol{\mathcal{I}} - \frac{\partial \boldsymbol{R}}{\partial \boldsymbol{Q}}\right] \Delta \boldsymbol{Q} = \boldsymbol{R}\,, \tag{3.2}$$

where V is the volume of the cell. Vector $\boldsymbol{R}$ represents the right hand side terms of the linear system and is defined as

$$\boldsymbol{R} \equiv -\sum_{i \in \text{cell}} (\boldsymbol{\mathcal{F}} - \boldsymbol{\mathcal{F}}_d) \cdot \boldsymbol{n}_i A_i + \boldsymbol{S}V \tag{3.3}$$

where A_i and $\boldsymbol{n}_i$ are respectively the area and normal vector of the i^{th} face of the cell.

3.2.2 Governing equations for the structural response module

The structural response module in KATS solves for the displacement field $\boldsymbol{u} \equiv (u_x, u_y, u_z)$. Three relations – force equilibrium, strain tensor and Hooke's Law – compose a closed system for the evaluation of the structural response, and are given as

$$\frac{\partial^2 \rho_s \boldsymbol{u}}{\partial t^2} - \nabla \cdot \boldsymbol{\sigma} = \rho_s \boldsymbol{f}, \tag{3.4}$$

$$\boldsymbol{\sigma} = 2\mu\boldsymbol{\varepsilon} + \lambda\ \mathrm{Tr}(\boldsymbol{\varepsilon})\boldsymbol{\mathcal{I}}, \tag{3.5}$$

$$\boldsymbol{\varepsilon} = \frac{1}{2}[\nabla \boldsymbol{u} + (\nabla \boldsymbol{u})^{\mathrm{T}}]. \tag{3.6}$$

where ρ_s represents the density of a solid material, $\boldsymbol{\sigma}$ is the stress tensor, t is time, $\mathbf{f}$ is the external body force per unit mass and $\boldsymbol{\varepsilon}$ is the strain tensor. μ and λ are respectively the first and second Lamé parameters, and are obtained with

$$\mu = \frac{E}{2(1+\nu)} \tag{3.7}$$

$$\lambda = \frac{E\nu}{(1+\nu)(1-2\nu)} \tag{3.8}$$

where E is Young's modulus and ν is Poisson's ratio. Since the components of the displacement vectors $\boldsymbol{u}$ are the variables for which the equation is solved, the conser-

vation equation can be rewritten as

$$\int_V \frac{\partial^2(\rho_s \boldsymbol{u})}{\partial t^2}\, dV - \oint_{\partial V} \left[\mu\left(\nabla \boldsymbol{u} + (\nabla \boldsymbol{u})^{\mathrm{T}}\right) + \lambda\ \mathrm{Tr}(\nabla \boldsymbol{u})\boldsymbol{\mathcal{I}}\right] \cdot \mathbf{n}\, da = \int_V \rho_s \boldsymbol{f}\, dV\,. \tag{3.9}$$

Initial conditions are set using the distribution of displacement $\boldsymbol{u}$ or $\partial \boldsymbol{u}/\partial t$ at $t = 0$. The solution is obtained by applying the usual boundary conditions such as a fixed support on the surface, symmetry, fixed pressure, fixed traction or free surface (zero traction).

3.2.3 Treatment for the time derivatives

Since the equilibrium equation for solid mechanics has a second-order time derivative, the time integration scheme must be different than the material response or flow field equations. In this study, the second-order time derivative term is split into two first-order time derivatives

$$\frac{\partial \boldsymbol{u}}{\partial t} = \boldsymbol{v}, \tag{3.10a}$$

$$\frac{\partial \boldsymbol{v}}{\partial t} + \nabla \cdot (\boldsymbol{\mathcal{F}} - \boldsymbol{\mathcal{F}}_d) = \mathbf{S}. \tag{3.10b}$$

where $\boldsymbol{v} \equiv (v_x, v_y, v_z)$ is the solid velocity vector. By doing so, the two equations can be solved using the KATS framework. Since the solid density is treated as a constant in the quasi-static scheme for each time step, the equations are divided by ρ_s on both sides. The governing equations, in the context of Eq. (7.1) and (7.2), are

thus represented by the following

$$\boldsymbol{Q} = \begin{pmatrix} u_x \\ u_y \\ u_z \\ v_x \\ v_y \\ v_z \end{pmatrix}, \boldsymbol{\mathcal{F}}_d = \frac{1}{\rho_s} \begin{pmatrix} 0 & 0 & 0 \\ 0 & 0 & 0 \\ 0 & 0 & 0 \\ 2\mu\dfrac{\partial u_x}{\partial x} + \lambda\nabla\cdot\boldsymbol{u} & \mu\left(\dfrac{\partial u_x}{\partial y} + \dfrac{\partial u_y}{\partial x}\right) & \mu\left(\dfrac{\partial u_x}{\partial z} + \dfrac{\partial u_z}{\partial x}\right) \\ \mu\left(\dfrac{\partial u_y}{\partial x} + \dfrac{\partial u_x}{\partial y}\right) & 2\mu\dfrac{\partial u_y}{\partial y} + \lambda\nabla\cdot\boldsymbol{u} & \mu\left(\dfrac{\partial u_y}{\partial z} + \dfrac{\partial u_z}{\partial y}\right) \\ \mu\left(\dfrac{\partial u_z}{\partial x} + \dfrac{\partial u_x}{\partial z}\right) & \mu\left(\dfrac{\partial u_z}{\partial y} + \dfrac{\partial u_y}{\partial z}\right) & 2\mu\dfrac{\partial u_z}{\partial z} + \lambda\nabla\cdot\boldsymbol{u} \end{pmatrix}, \tag{3.11}$$

$$\boldsymbol{S} = \begin{pmatrix} v_x \\ v_y \\ v_z \\ \rho_s f_x \\ \rho_s f_y \\ \rho_s f_z \end{pmatrix}. \tag{3.12}$$

3.2.4 Thermo-mechanical coupling procedure

Since the structural response reaches equilibrium at a much faster speed than thermal response, a quasi-static approach is sufficient, and much more efficient. Therefore, although the KATS mechanical response solver is able to solve transient problems, when coupled to the thermal response solver, a simplified, quasi-static version is used. The equations solved for this quasi-static approach are obtained by setting vector $\frac{\partial \boldsymbol{Q}}{\partial t}$ of Eq. (7.1) to zero. The KATS framework can still be used to solve this system, and Eq. (7.2) becomes

$$\Delta\boldsymbol{Q} = \left[\frac{\partial \boldsymbol{R}}{\partial \boldsymbol{Q}}\right]^{-1} \boldsymbol{R}, \tag{3.13}$$

where $\boldsymbol{Q} = \boldsymbol{u}$. It is to be noted that solving this equation is identical to applying Newton's iterative method for a system of equations.

A overview diagram of the coupling scheme is provided in Fig. 3.1. As illustrated, the quantities computed by the structural response code are not transferred back to the thermal response code. Since ablation problem are temperature-driven, the temperature changes caused by strain and deformation are negligible. Therefore, there is no need to account for the mechanical term in energy equation of the thermal response. The changes in solid density caused by the deformation, however, might not be negligible, are omitted for the present study.

The coupling strategy uses the time step sizes imposed by the thermal response module. At a fixed frequency number of time step s, the temperature and solid density results are transferred to the structural response module. The structural response module then uses them to solve the displacement, stress and strain fields. Since both modules use the same finite volume framework, a shared computational grid is used, which avoids interpolations between cell centers and neighboring nodes and increases the fidelity of the whole solution. The iterative process is repeated until the final time t_f is reached.

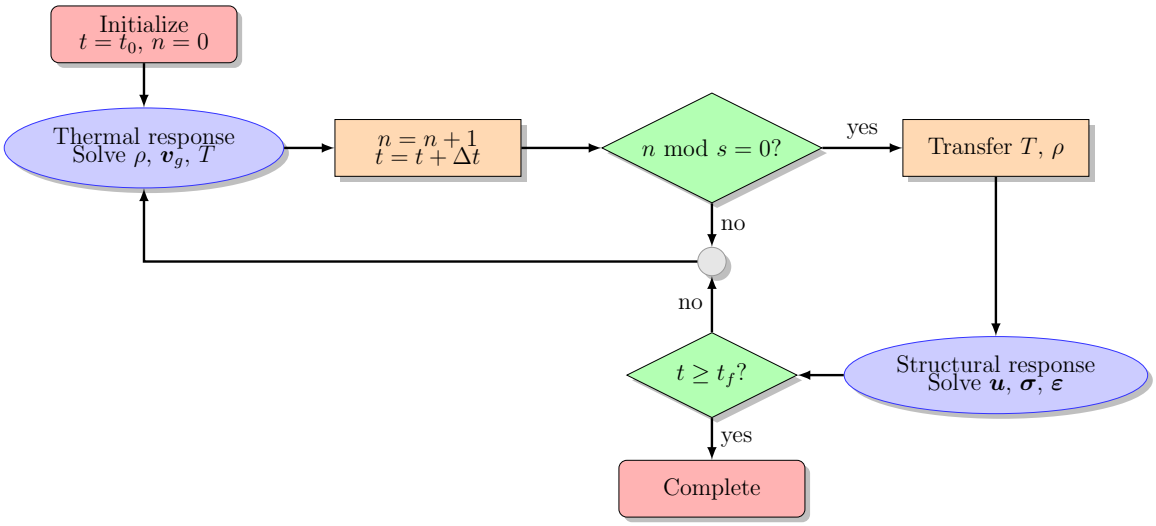

Figure 3.1: Coupling scheme between the structural response and thermal response

3.3 Verification

The structural response code was initially verified for transient response using two test cases. A coupled test case was also performed to show the accuracy of the temperature field and the thermal expansion for a steel plate. All verification test cases used steel as the material, with properties given in Table 3.1. The material was assumed to be isotropic, and all the properties were considered independent of temperature.

Table 3.1: Thermal and mechanical properties for steel

Density, kg/m^3	Specific heat, J/(kg·K)	Conductivity, W/(m· K)
7850	434	60.5
CTE, μm/(m·K)	Young's modulus, GN/m^2	Poisson's ratio
12	200	0.3

3.3.1 Transient solution - compression of a steel bar

The first test case was designed to verify the transient response of the solid material. A steel bar was compressed on one end, using a ramping 1×10^6 Pa pressure load, while the other end was fixed, as shown in Fig. 3.2a. It should be noted that the fixed support constrained all displacement vectors to zero. The results, presented in Fig. 3.2b, were compared to an analytical solution obtained using d'Alembert's formula [87].

The L^2 relative error was calculated for three different times. The values obtained were 0.320%, 0.318% and 0.318% for $t = 0.5 \times 10^{-3}$ s, 1.0×10^{-3} s and 1.5×10^{-3} s, respectively. The computed results are considered to be in excellent agreement with the analytical solution at each time step.

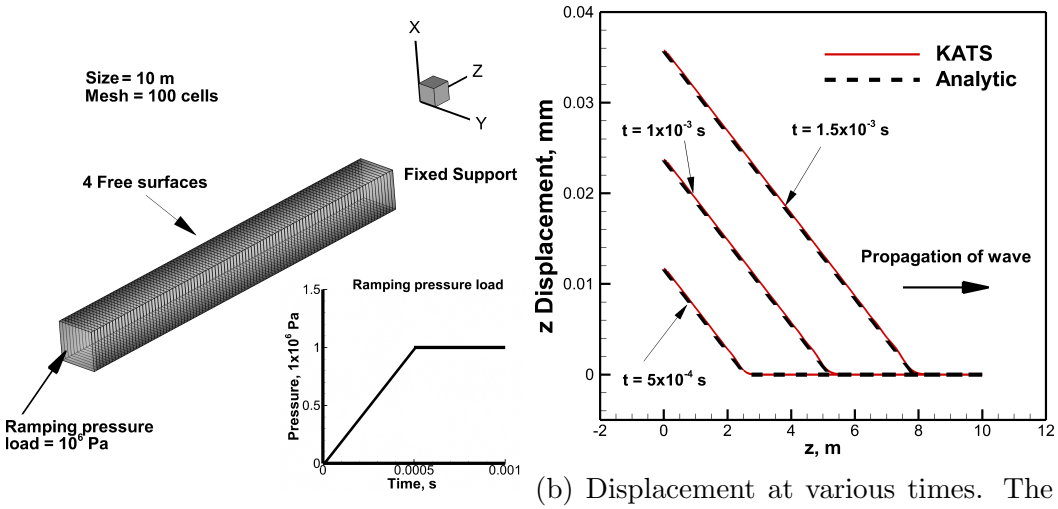

(a) Boundary conditions, dimensions, and computational grid

(b) Displacement at various times. The solution obtained using KATS is compared to an analytical solution

Figure 3.2: Problem definition and results for the first verification test case – transient compression of a 1D steel bar

3.3.2 Transient solution - compression of a 2D steel plate

The second verification test case was designed to verify the geometric effects on two dimensional problems. For this case, the 2D steel plate illustrated in Fig. 3.3a was considered. The mesh, dimension and boundary conditions are also provided in Fig. 3.3a. More specifically, one end of the plate was fixed, while a ramping 1 mm compression displacement was applied to the other. All other boundaries were assumed to be free surfaces.

The computed results were verified by performing a code-to-code comparison with the commercial FEM software ANSYS [34]. Comparisons were performed along three lines parallel to the direction of compression, at $x = 0.5$ m, 0.75 m and 1 m. The results at $x = 0.5$ m are illustrated in Fig. 3.3b and show that the $y-$displacement agrees remarkably well with the results obtained using ANSYS. The L^2 relative errors – the maximum value over time – was also calculated, with values of 0.228%, 0.432% and 0.434% obtained at the three locations.

In addition to the comparison, contour plots of the compression waves are dis-

played in Fig. 3.3c. These plots illustrate the propagation of the deformation wave within the plate, with local expansion effects.

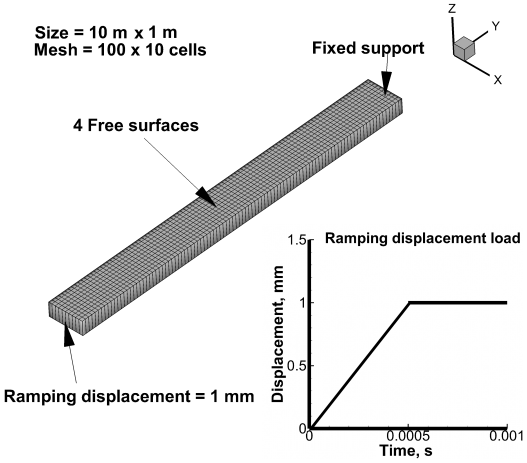

(a) Boundary conditions, dimensions and computational grid

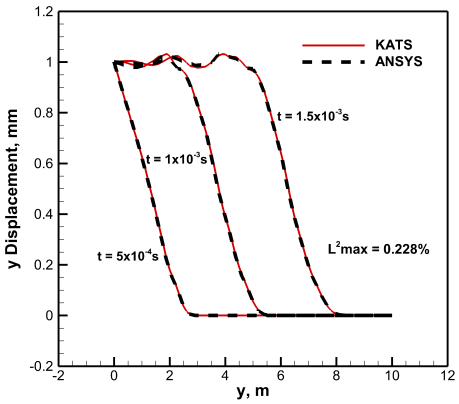

(b) Displacement at various times. The solution obtained using KATS is compared to an analytical solution

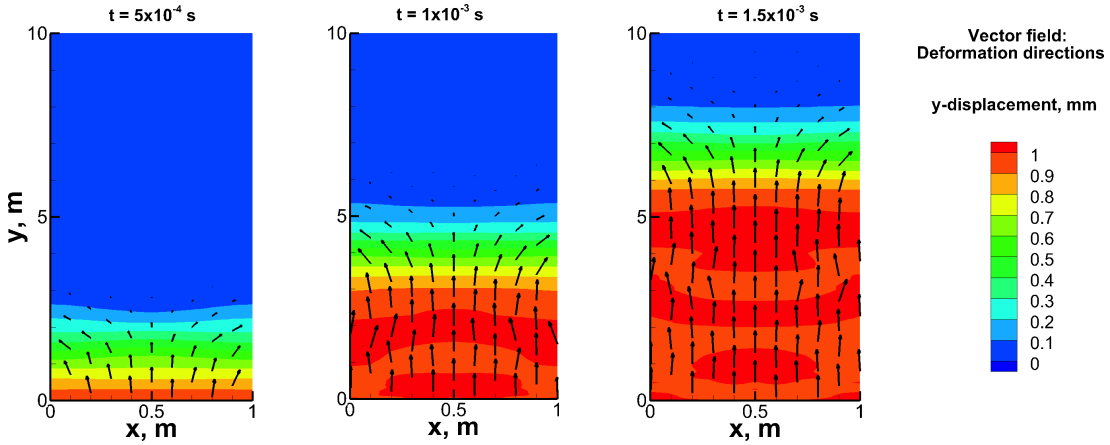

(c) Isocontours of the displacement in the y-direction at various times, illustrating the compression waves propagating within the plate

Figure 3.3: Problem definition and results for the second verification test case – transient compression of a 2D steel plate

3.3.3 Coupled solution - heating of a steel plate

The goal of the present work is to calculate the thermal strain and quantify its effects on the stress field. Therefore, the coupled results must be carefully verified. This is achieved by comparing the coupled results obtained with the KATS code with

those of a commercial software. For this third verification test case, a steel plate initially at 298 K was subjected to a constant heat flux for 10 seconds. Because of the disparity in the time scales of the thermal and structural problem, the quasi-static structural equations were solved. The boundary conditions and computational grid are presented in Fig. 3.4. The computational grid was refined near the surface, where heat flux is applied, since larger gradients were expected in this area.

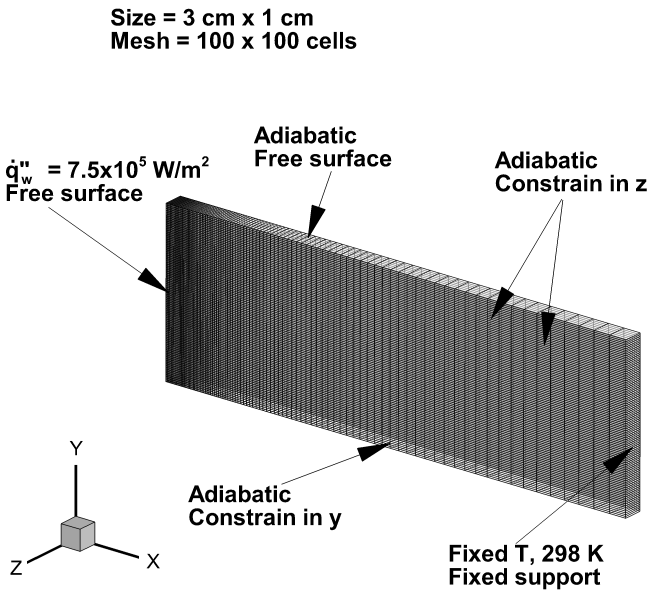

Figure 3.4: Problem definition for the third verification test case – coupled heating of a steel plate

Results at $t = 1, 5$ s and 10 s are presented in Fig. 3.5. As expected, at $t = 1$ s, the temperature increases along the heated surface. At the same time, the plate expands to the negative x and positive y directions, as shown in Fig. 3.5a. This becomes more evident after 10 s of heating, as shown in Fig. 3.5b.

In order to compare the results to the ANSYS commercial software, data points were extracted at $y = 0.005$ m along the plate, at $t = 1, 5$ and 10 s. The comparison of the temperature profile are presented in Fig. 3.6a. The comparison of the displacement is shown in Fig. 3.6b. For this case, the relative overall L^2 error was calculated

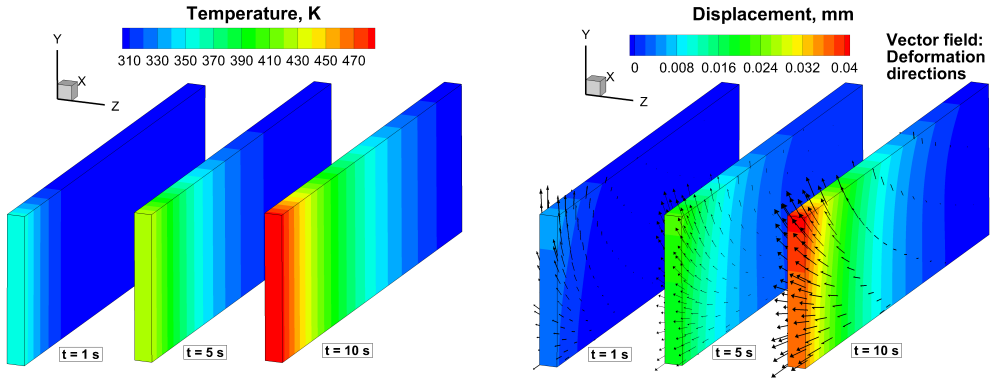

(a) Temperature isocontours (b) Displacement isocontours

Figure 3.5: Results for the third verification test case – coupled heating of a steel plate

to be 0.14 %, which is considered to be excellent. These results indicate that both the implementation and information transfer for the quasi-static coupling approach is valid. Moreover, it demonstrates that the finite volume approach used in KATS compares very well to the usual finite element method.

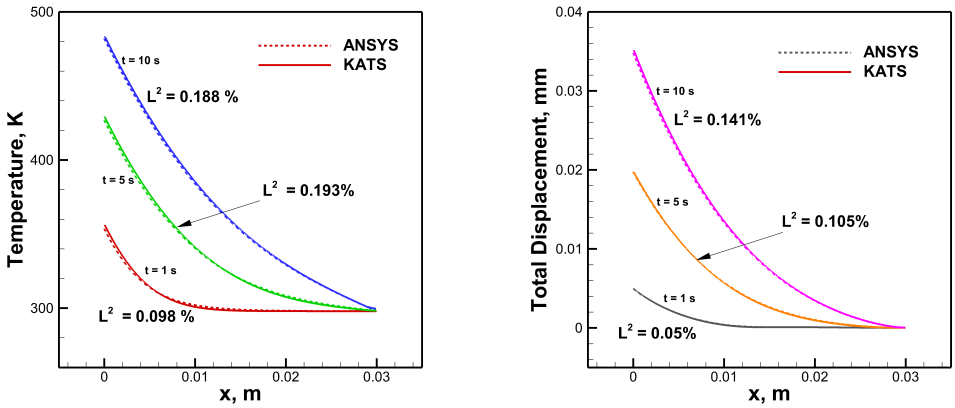

(a) Temperature comparison (b) Displacement comparison

Figure 3.6: KATS results compared to the ANSYS results for the third verification test case – coupled heating of a steel plate

In order to ensure the proper implementation of the numerical method, a complete grid convergence study was performed for this test-case. Three grids – each 3 times as refined as the previous one – were used to calculate the theoretical order of accuracy

of the scheme. More specifically, KATS uses a cell centered solver, for each refinement of the computation grid, the number of cells is tripled. The grids and the time steps for this test are listed in Table 3.2.

Table 3.2: Grid refinements and time step sizes for the convergence test

Refinement	Number of grid cells	Time step size	Number of time steps
coarse	90×30	9×10^{-3}	1,000
fine	270×90	3×10^{-3}	3,000
finest	810×270	1×10^{-3}	9,000

By assuming the solutions of variable X obtained at three different grid as coarse, fine and finest are X_{coarse}, X_{fine} and X_{finest}, the spatial order of accuracy can then be calculated as:

$$\text{order} = \log_3 \frac{\parallel X_{coarse} - X_{finer} \parallel_2}{\parallel X_{finer} - X_{finest} \parallel_2}, \tag{3.14}$$

The calculated orders of accuracy for each primitive variables are listed in Table 3.3. It can be seen that for all the variables, the orders of accuracy are very desirable and close to the expected value, two (2). Note that sine this is a 2D problem, no results for the u_z. The results show satisfactory convergence to the exact solution of the system for both the coupling scheme and the static structural response.

Table 3.3: Spatial orders of accuracy from the grid function convergence test

Variable	T	u_x	u_y	u_z
Order	2.032	2.035	1.921	N/A

3.4 Results: carbon phenolic charring ablator

To demonstrate thermo-mechanical coupling, the thermal loading of a representative ablative material was simulated. The geometry and boundary conditions are presented in Fig. 3.7. The testing material was TACOT, with thermal properties provided in Ref. [88].

Since no mechanical properties have been published for TACOT, the values for a similar material, obtained from Ref. [38], are used. The tabulated values for both Young's modulus and the CTE are given in Table 3.4. As for the Poisson's ratio, it is considered constant, with a value of 0.3. Unfortunately, no values were available for the char state. For Young's modulus, the last tabulated values of the virgin state is used, as it is assumed that the resin has nearly all pyrolyzed at that temperature. For the CTE, under the same assumption, a value obtained experimentally for XN05 carbon fibers is used [89]. The value are considered constant since the temperature dependency of structural properties is mainly due to the resin. All the properties for the char state are listed in Table 3.5.

Table 3.4: Mechanical properties for the virgin TACOT

Temperature, K	CTE, μm/(m·K)
130	170
233	170
297	172
308	175
428	236
474	339
495	401
587	304
652	151
675	51.3
700	2.6
1000	2.6

Temperature, K	Young's modulus, GN/m^2
156	14.7
205	12.8
299	10.3
363	9.05
428	7.96
474	5.12
538	1.81
587	1.38
652	1.69
678	1.73
700	1.73
1000	1.73

The front surface ($x = 0$ m) was subjected to a constant heat flux of $\dot{q}''_w = 7.5 \times 10^5$ W/m^2, and a constant pressure of $p = 101,325$ Pa. The back wall ($x = 0.075$ m) was

Table 3.5: Mechanical properties for the char TACOT

CTE, μm/(m·K)	Young's modulus, GN/m^2	Poisson's ratio
2.6	1.73	0.3

assumed to be adiabatic and impermeable. The side wall ($y = 0.05$ m) was considered adiabatic, permeable, and with a fixed pressure identical to the front surface pressure. The rest of the thermal boundaries, including $y = 0$ m, $z = 0$ m, and $z = 0.005$ m, were set to symmetry planes. For structural boundary conditions, the back wall ($x = 0.075$ m) was set as fixed support, the front wall and the side wall were set as free surfaces with no constraint, and the rest of the walls were constrained as shown in Fig. 3.7.

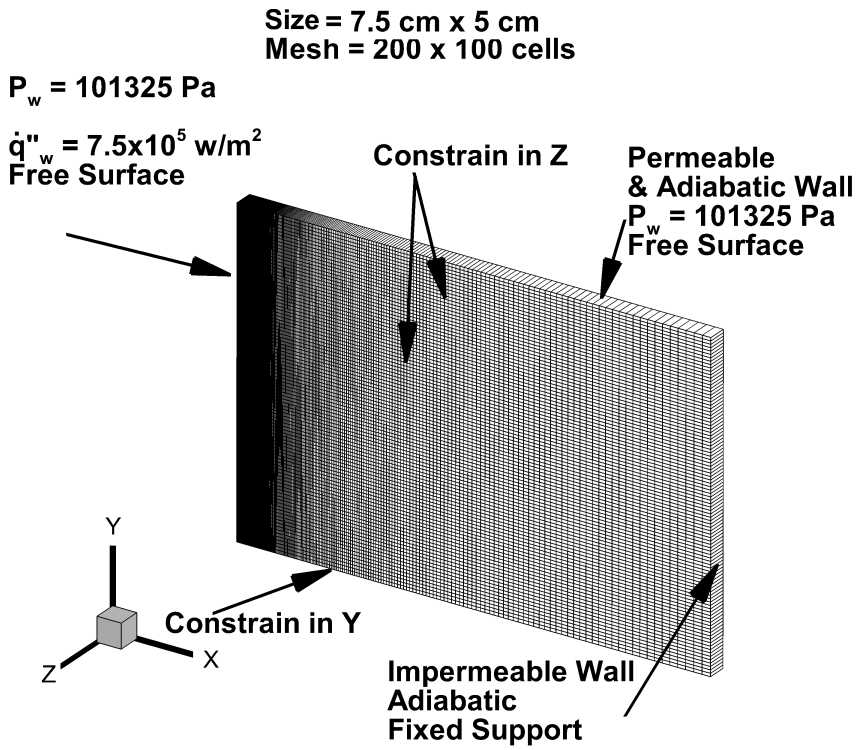

Figure 3.7: Problem definition for the 2D low-density porous ablative material (TACOT) demonstration test case

3.4.1 Results between $t = 0$ s and 1 s

The temperature, displacement, density and stress distribution between 0 s and 1 s are presented in Fig. 3.8. During initial phase, only a small portion of the plate is affected. Therefore, the results are shown for a small subset of the domain, ranging from $x = [0, 0.01]$ m. Figure 3.8a shows that the temperature starts to increase throughout the front surface of the plate, and that the stress concentration pulse, defined as the region where the stress is greater than 100 MPa, follows the same progression. Figure 3.8b shows that the deformation begins at the upper left corner and continues to increase as time elapses. This figure also indicates that the maximum displacement is only about 0.35 mm.

Figure 3.8c shows the solid density distribution within the test sample. It can be noted that the region of maximum stress appears near the edge of the virgin region, where the material starts to pyrolyze. This is clearly illustrated in Fig. 3.8d, where the progression of the von Mises stress is shown. It can be seen that the region with any significant stress is directly bounded by the pyrolysis zone ($T \in [350, 700]$).

Figure 3.9 demonstrates the correlations between the displacement, solid density, temperature and von Mises stress, along the $y = 0$ m line. This location was chosen as it corresponds to the centerline of the plate. In order to better illustrate the phenomenon, only the region between $x = [0, 0.015]$ m is illustrated as the rest of the domain is uniform. These results were taken at $t = 0.01$ s, 0.04 s, 0.10 s, and 1 s to show the time dependency. Figure 3.9a shows that the peak of stresses moves into the material, following the deformation of the plate. Figure 3.9b shows the results of von Mises stress and the solid density for the mentioned four time snapshots. The locations of the largest stress move within the sample as time elapses, and even enter the virgin zones. Figure 3.9c shows the relationship between the stress and temperature field. The temperature keeps increasing from the front surface ($x = 0$ m), stress moves into the plate and the exact peak occurs within the pyrolysis zone,

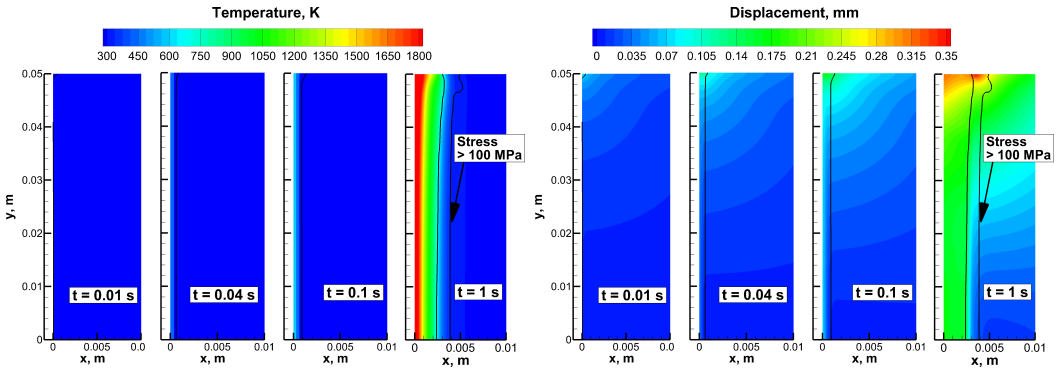

(a) Temperature isocountours and stress concentration isolines

(b) Solid displacement and stress concentration isolines

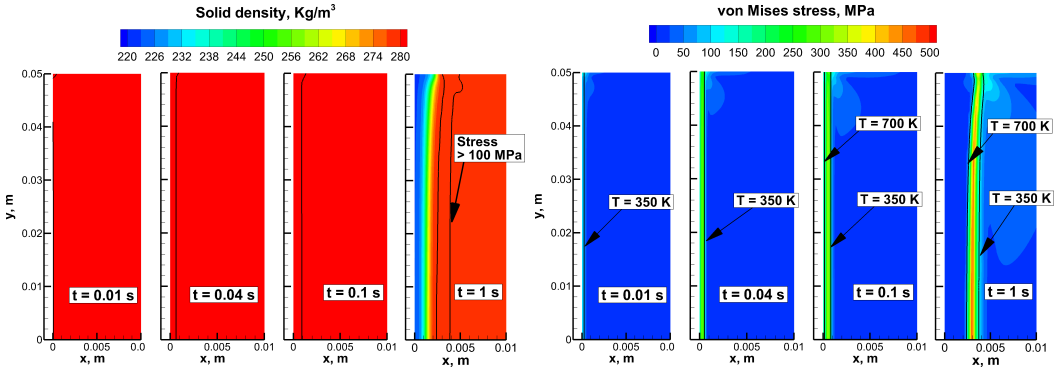

(c) Solid density isocontours and stress concentration isolines

(d) Von Mises stress isocontours and temperature isolines

Figure 3.8: Results for $t \in [0.01, 1]$ s for the 2D low-density porous ablative material (TACOT) demonstration test case

at $T \approx 600$ K.

3.4.2 Results between $t = 1$ s and 15 s

Results between 1 s and 15 s are presented in Fig. 3.10. In Fig. 3.10a, the temperature of the sample reaches up to 4000 K and the deformation, shown in Fig. 3.10b, is larger than the ones in Fig. 3.8a. The stress concentration contour line shows that region of maximum stress continuously penetrates into the material, always preceding the high temperature region. Figure 3.10c shows the correlation between solid density and stress magnitude. It can be seen that the stress concentrates on the area in the virgin material, close to the pyrolysis front. Figure 3.10d illustrates the von Mises stress and the temperature isolines. The figure shows that the distribution of stress

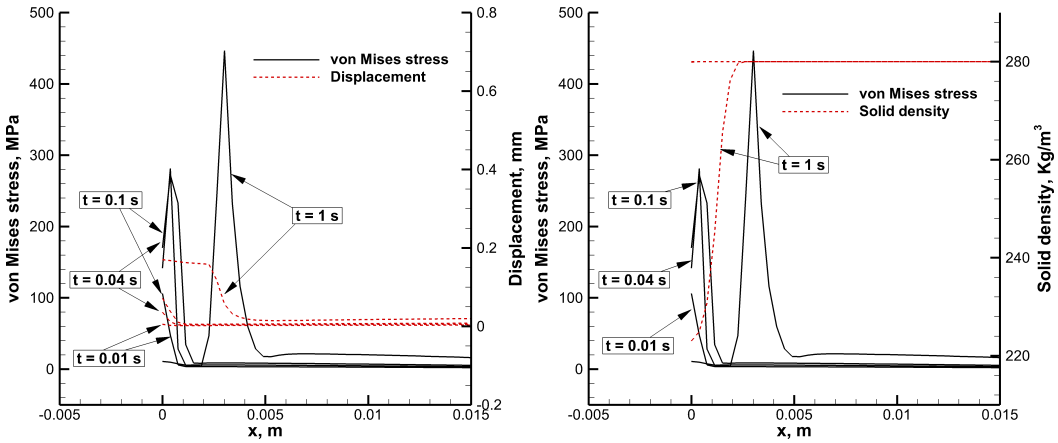

(a) Displacement and von Mises stress

(b) Solid density and von Mises stress

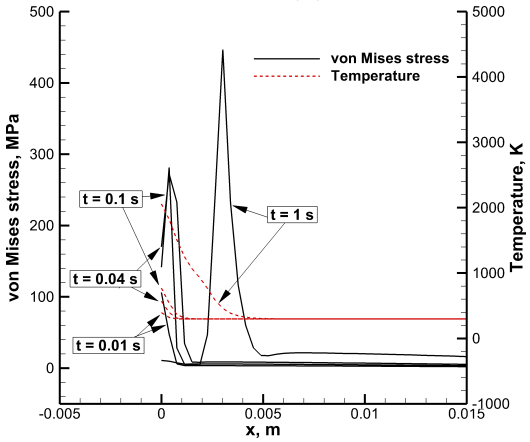

(c) Temperature and von Mises stress

Figure 3.9: Results along $y = 0$ m and $x = [0, 0.015]$ m for $t \in [0.01, 1]$ s for the 2D low-density porous ablative material (TACOT) demonstration test case

has direct relation to the temperature profile, and that the greatest value still falls within the $T = 350$ K and $T = 700$ K contour lines, that is, the pyrolysis region. These figures show that the peak of the stress occurs within the pyrolysis zone, very near to the virgin zone. In this region, the material has not yet fully decomposed, even though the pyrolysis has started.

The results from these contour plots can be understood more easily when presented along a single line ($y = 0$ m), as is done in Fig. 3.11. Figure 3.11a shows that the stress and the deformation are related and vary with time. It can be seen that the greatest gradient of deformation results in the maximum stress. Figure 3.11b clearly illustrates

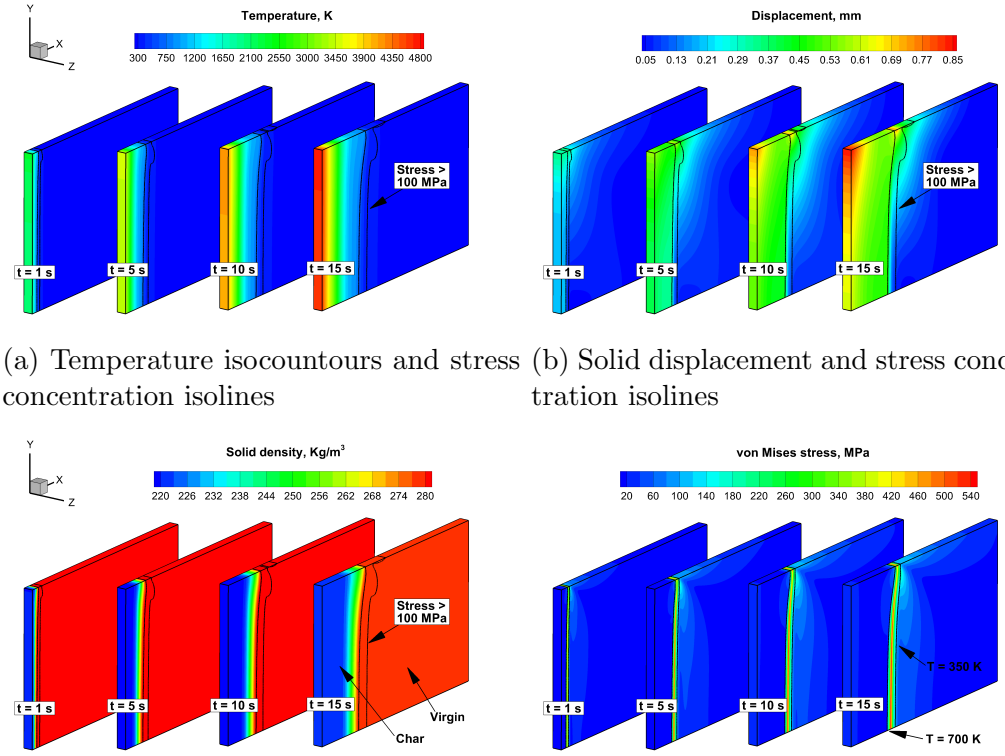

(a) Temperature isocountours and stress concentration isolines

(b) Solid displacement and stress concentration isolines

(c) Solid density isocontours and stress concentration isolines

(d) Von Mises stress isocontours and temperature isolines

Figure 3.10: Results for $t \in [1, 15]$ s for the 2D low-density porous ablative material (TACOT) demonstration test case

the delay between the solid density and the maximum stress. The peaks of the stress are always located at the forefront of the pyrolysis zones. This is also observed in Fig. 3.11c where large part of the peak occurs in a relatively low temperature region.

3.4.3 Discussion

The behavior previously described is mainly due to two combined effects. The first is the result of the non-uniform temperature distribution that leads to a non-uniform material expansion, and generates internal stresses. The second is generated by the intrinsic changes within the material caused by pyrolysis. The material properties – Young's modulus and CTE, for instance – have significantly different values in the virgin and char state. When the material goes from one state to the other, the steep

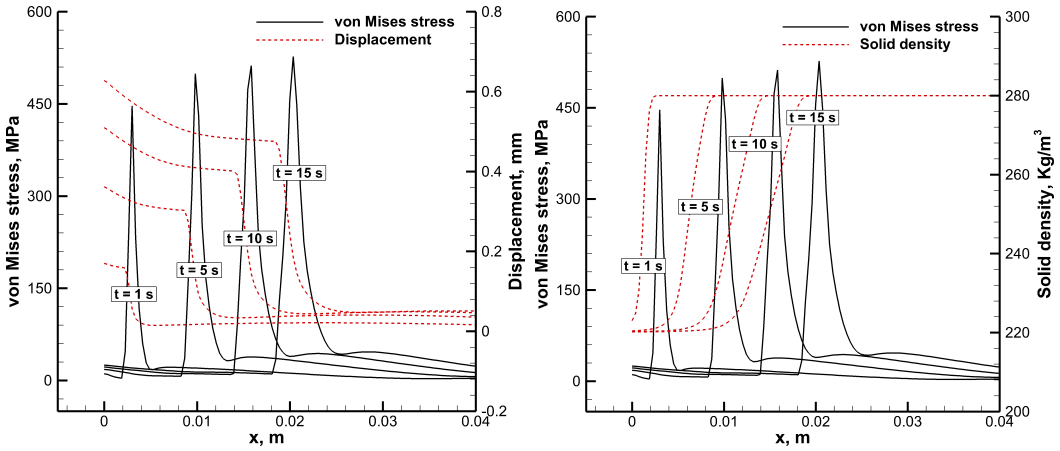

(a) Displacement and von Mises stress

(b) Solid density and von Mises stress

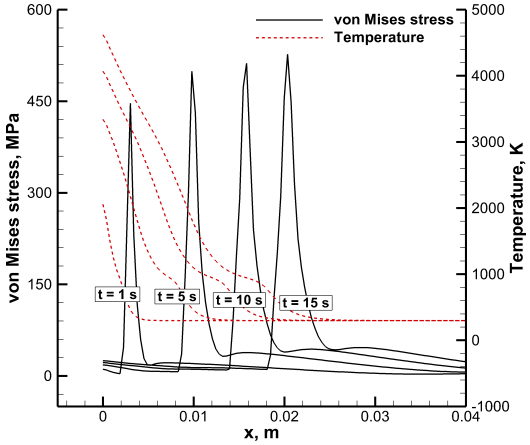

(c) Temperature and von Mises stress

Figure 3.11: Results along $y = 0$ m and $x = [0, 0.04]$ m for $t \in [1, 15]$ s for the 2D low-density porous ablative material (TACOT) demonstration test case

changes in the properties intensifies the stress concentration.

The most interesting observation comes from the magnitude and location of the stress. Both of them play a critical role in determining when and where the TPS is likely to fail. The process of charring, by itself, may cause mechanical fracture of the TPS material.

The results presented here indicate that the location of the peak stress occurs in the pyrolysis zone, at the edge of the virgin zone, when the charring process begins.

The significance of these results can go further than the effect on strain and stress. Even if the total displacement, as its maximum, is about 0.8 mm, the local strain can

cause significant changes in the material properties, such as porosity, conductivity, and permeability. Moreover, the thermal expansion causes deformation of the geometry. In order to fully evaluate these effects on the material, a strong coupling scheme is necessary. This would result in mesh deformation, and would undoubtably impact the heat propagation within the material.

3.5 Conclusion

In order to perform detailed analysis of the structural response of ablative material, a new solid mechanics solver was developed, using a finite-volume approach. This numerical method was chosen to facilitate coupling with both hypersonic flow solvers and material response codes. Verification test cases show that solid mechanics problems can be modeled with sufficient accuracy and efficiency by using a finite volume approach instead of the usual finite element method. The coupling capabilities were demonstrated through a 2D test case, using a low density porous ablative material. The simple test case was able to demonstrate that the location of maximum stress occurred in front of the pyrolysis zone, where the material had barely begun to char. It also showed that the regions of high stress concentration occur within the pyrolysis zone, where the temperature gradient and variations of material properties are significant. The location and the magnitude of the stress is due to both non-uniform temperature gradients and the variations in the material properties due to the charring process.

These findings are of great interest to material response modeling since it is believed that high stress leads to crack formation, which has been observed in some ablative materials. The high stress front could also lead to a severe weakening of the fibers that, combined with oxidation, eventually results in spallation. Spallation is an undesirable phenomenon for a TPS material since it accelerates the recession of the ablator.

The results presented here are exploratory, but allow to highlight phenomena that can only occur through coupling. The next step will be to fully assessed them by using a strong coupling approach – both with the material response and the flow field – and by modeling realistic materials, validated by detailed experiments.

Chapter 4: Investigation of Internal Pressure within Ablative Material

In order to increase the insulation properties and decrease mass, modern TPS materials are usually highly porous. They are usually composed of a fibrous substitute impregnated with resin material. Under entry conditions, resin material decomposes and generates pyrolysis gas. The resulted gas can change the temperature distribution dramatically by providing a form of transpiration cooling. Another consequence is that because the pyrolysis gas flows within the porous structures, it will exert pressure field on the surfaces within the material, and that is the source of internal pressure.

This chapter presents an exploratory study on the internal pressure of ablative material. In order to evaluate the stress and deformation caused by internal pressure field, the structural response code is coupled with the existing thermal response module.

4.1 Coupling scheme

The one-way coupling scheme used in internal pressure coupling is similar compared to the one described in Chapter 3. The same quasi-static approach is used as a basic framework. Figure 4.1 shows the information transfer between the thermal response and structural response. As the simulation progresses, thermal response delivers the pressure field, changes of density and grid information to the structural response module. The structural response uses those variables to calculate the displacement and stress.

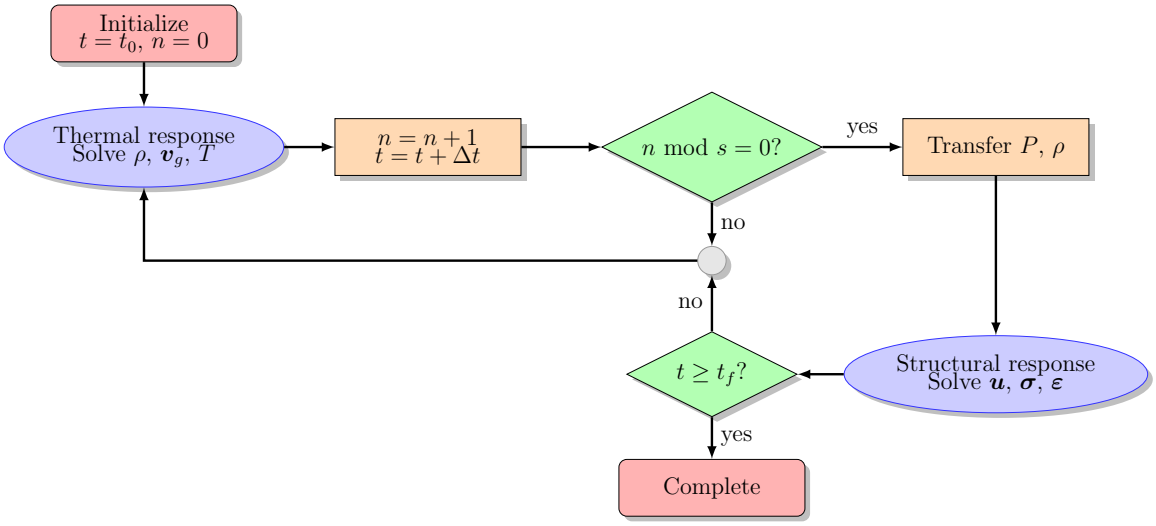

Figure 4.1: A one-way coupling scheme for internal pressure coupling

4.2 Material model and limitations

In order to investigate the internal pressure field within the ablative material during ablation process, some key assumptions are needed. The first concept needed to clarify is the internal pressure field. In this study, the pressure field is generated by the pyrolysis gas. Thus, the shear force exerted by external hypersonic flow field is not considered. In addition, because of the relatively low speed of pyrolysis gas, shear force caused by flowing through pores is not taken into account. Thus, the internal pressure $P_{internal}$ is the relative pressure, which can be calculated as

$$P_{internal} = P - P_{ref}, \tag{4.1}$$

where P is the produced pyrolysis gas pressure, P_{ref} is the reference pressure at the initial state, which is set to be 101,325 Pa. The models and detailed calculation for the pyrolysis gas flow can be found in Ref. [72].

The second key concept to define is the porous material model. In this study, the porous media is considered to be isotropic material with uniformly distributed pores. In addition, these pores are assumed to be interconnected so that pyrolysis gas can freely flow from one pore to another. Based on these assumptions, the internal

pressure is considered to exert force uniformly on the walls of each elements. Thus, no sudden jumps and defects are modeled. Based on this, the absolute magnitude of internal pressure is expected to be small, even for the impermeable walls used as boundary conditions.

As a result of those assumptions, the porous material is treated as a bulk material with isotropic material properties. However, the reality is definitely different; as the distribution of the pore size is non-uniform, and some of those pores are not connected. Thus, pressure can be built up rapidly in sealed pores and lead to a micro-scale explosion.

4.3 Stress calculation

The internal pressure is the result of the pyrolysis gas produced by chemical reaction of the virgin material[71]. Since pressure directly acts on the fibrous element surfaces within the material, it can be directly added into the stress tensor on the normal direction as:

$$\boldsymbol{\sigma}_{ij} = \boldsymbol{\sigma}_{ij}^{total} - P\mathcal{I}_{ij} \tag{4.2}$$

where the superscript *total* represents all the forces acts on a certain cell surface.

4.4 Carbon phenolic charring ablator with permeable wall

4.4.1 Case setup and boundary conditions

The testing material used for this test is TACOT, with tabulated values for both Young's modulus and the CTE given in Table 3.4 for virgin and Table 3.5 for char.

The geometry and boundary conditions are presented in Fig. 4.2. The front surface ($x = 0$ m) was subjected to a constant heat flux of $\dot{q}''_w = 7.5 \times 10^5$ W/m^2, and a constant pressure of $p = 101,325$ Pa. The back wall ($x = 0.075$ m) was assumed to be adiabatic and impermeable. The side wall ($y = 0.05$ m) was considered adiabatic,

permeable, and with a fixed pressure identical to the front surface pressure. The rest of the thermal boundaries, including $y = 0$ m, $z = 0$ m, and $z = 0.005$ m, were set to symmetry planes. For structural boundary conditions, the back wall ($x = 0.075$ m) was set as fixed support, the front wall and the side wall were set as free surfaces with no constraint, and the rest of the walls were constrained as shown in Fig. 4.2.

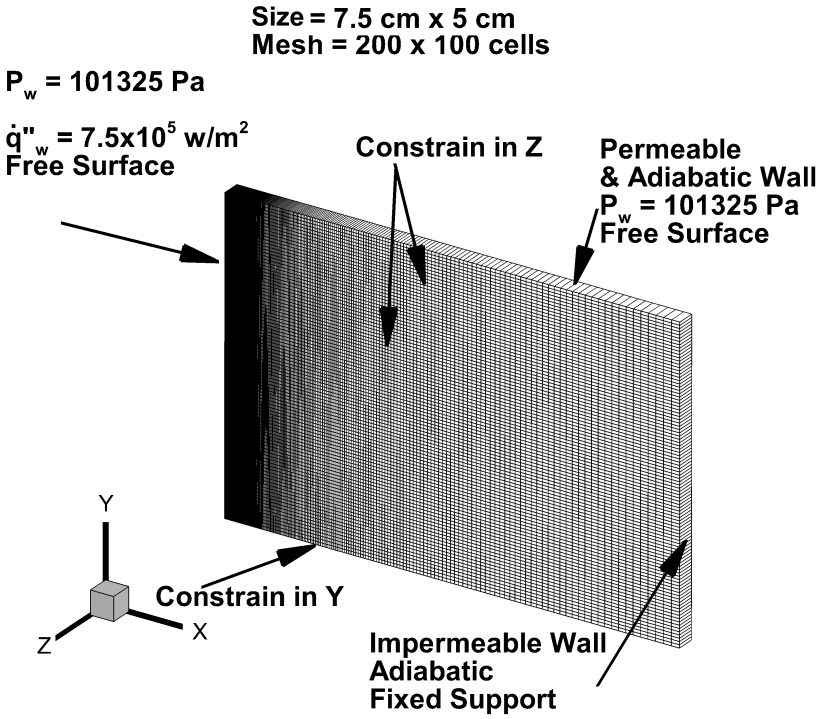

Figure 4.2: Problem definition for internal pressure investigation in charring ablation. Boundary conditions, dimensions and computation grid with a top surface as permeable wall

4.4.2 Numerical results

Figure 4.3 shows a series of isocontours evolutions for various variables at $t = 1, 5, 10$ and 15 s. In Fig. 4.3a, the temperature increases as time elapses, with almost uniform distribution. Since the top surface is permeable, heat conduction becomes slightly stronger on the top side wall. In Fig. 4.3b, the pressure fields are presented. It can be seen that the overall magnitude of the internal pressure is small, around 3,600 Pa.

However, as ablation continues, the pressure field becomes more uniform, and on the char regime, the relative pressure becomes negative. In Fig. 4.3c, the evolution of displacement results is presented. It can be observed that since the absolute pressure is small, the resulting maximum displacement is only 0.002 mm, which is 2 microns, and then can be ignored when compared to the size of the geometry. Still, the distribution of displacement is very uniform and tends to expand to the upper left. In Fig. 4.3d, the isocontours of the resulting von Mises stress are presented. Because the driving force - internal pressure - is small, as a consequence, there is no significant changes in stress level as time elapses. The maximum stress locates at the upper right corner because of the fixed support, necessary to hold the plate.

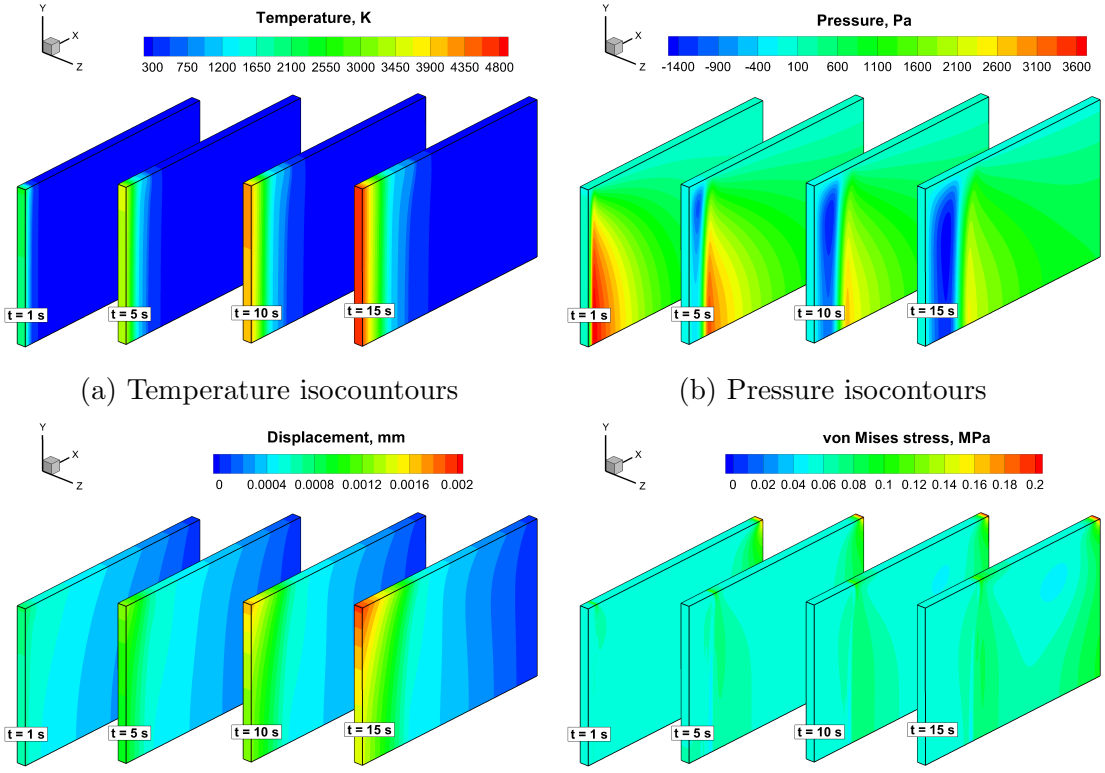

(a) Temperature isocountours

(b) Pressure isocontours

(c) Displacement isocontours

(d) Von Mises stress isocontours

Figure 4.3: Isocontours for $t \in [1, 15]$ s for various variables for permeable top surface case

Figure 4.4 presents the results for pressure, displacement and stress on the axis ($y = 0$ m). Figure 4.4a shows the evolution of temperature and pressure. It can be

observed that as the material ablates, the surface temperature reaches the unrealistic value of 4,800 K. With respect to pressure, the absolute magnitude decreases while at the front, the negative value increases, which results in a 'pulling' effect on the material. Figure 4.4b shows the relationship of displacement and pressure. The pulling effects can be clearly seen as time elapses as the displacement keeps increasing. Figure 4.4c shows the relationship of von Mises stress and pressure. It is interesting to see the complex profile stress caused by internal pressure. As discussed, the maximum stress, around 0.1 MPa, is located at the bottom surface where a fixed support holds the plate. In addition, because of the increased displacement, the overall stress keeps increasing while decreasing at the front part, due to the negative pressure distribution.

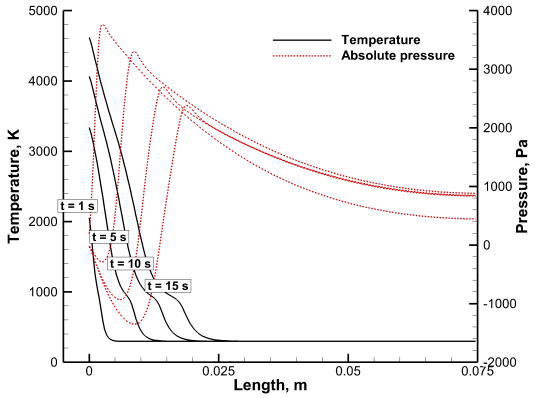

(a) Pressure and temperature

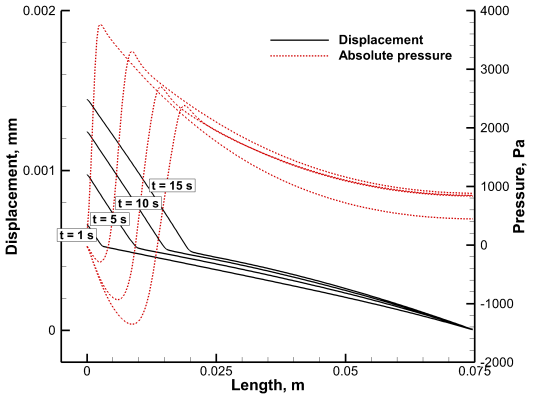

(b) Pressure and displacement

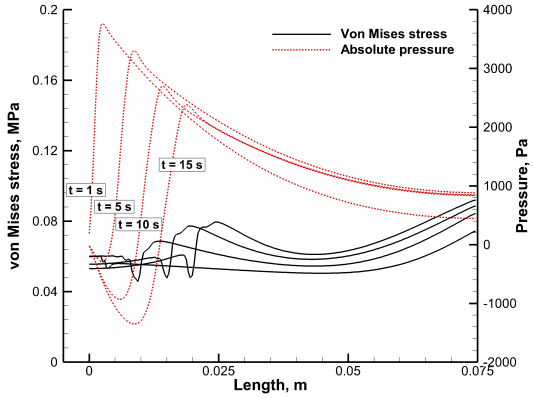

(c) Pressure and von Mises stress

Figure 4.4: Temperature, displacement, von Mises stress and internal pressure for the permeable top surface case.

4.5 Carbon phenolic charring ablator with impermeable wall

This test-case investigates the internal pressure within a charring ablation process. The difference with this case and the previous one is the top surface ($y = 5$ cm), which is set to be impermeable.

4.5.1 Case setup and boundary conditions

The geometry and boundary conditions are presented in Fig. 4.5. All the material properties are identical to the permeable wall case of Section 4.4. All the boundary conditions are the same except the top surface is set to be impermeable, with a fixed support. Therefore, no pyrolysis gas can flow through the top surface and as a result, the temperature distribution is expected to be as uniform as the pressure field.

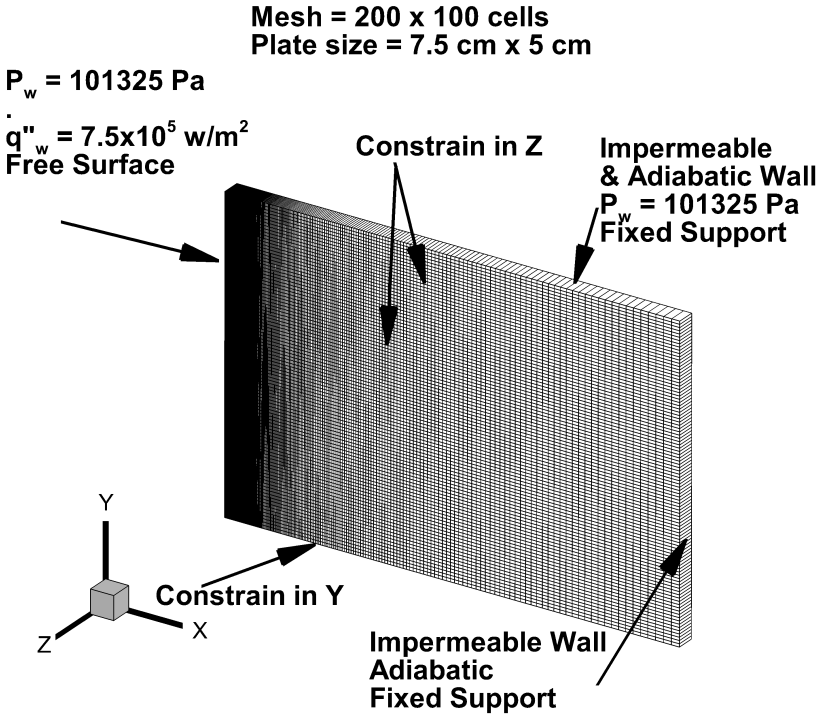

Figure 4.5: Problem definition for the internal pressure investigation in charring ablation. Boundary conditions, dimensions and computation grid with a top surface as impermeable wall

4.5.2 Numerical results

Figure 4.6 shows a series of isocontours evolution for various variables at $t = 1, 5, 10$ and 15 s. The evolution of temperature results are displayed in Fig. 4.6a. As no gas exits the top surface, the temperature field is uniformly distributed along x direction. However, temperature keeps increasing as the front surface is constantly subjected to large heat flux. The evolution of internal pressure results is presented in Fig. 4.6b. The first difference, when compare to the previous case is that the internal pressure is uniformly distributed along the x direction, as is the temperature. Secondly, unlike the permeable wall case, there is no negative value of the relative pressure. This is due to the fact that the gas can only flow through the left front surface, and that there is a constant environmental pressure applied to that surface. However, since pressure increases inside the plate, the resulted pressure field still has a "pulling" effect on this plate. The evolution of displacement result is presented in Fig. 4.6c. It can be observed that the "pulling" effect leads to the expansion of the center part of the front surface. Because the top wall and left end wall are fixed, the plate can only expands to the center area. The magnitude of the maximum displacement remains very small with a value of 0.0012 mm. The evolution of von Mises stress results is presented in Fig. 4.6d. Since the relative pressure and the resulted displacement are all very small, the stress caused by them are small, with a maximum value of 0.2 MPa located at the top right corner of the plate. No significant changes can be seen as the ablation continues.

The comparisons of temperature, displacement, von Mises stress and internal pressure are presented along $y = 0$ m in Fig. 4.7. Figure 4.7a shows the comparison between temperature and pressure. It can be seen that for this case, no negative pressure occurs within the plate and the relative pressure keeps increasing with time as the temperature on the front surface keeps increasing. Figure 4.7b shows the comparison between displacement and pressure. It is very intersting to see a similar distribu-

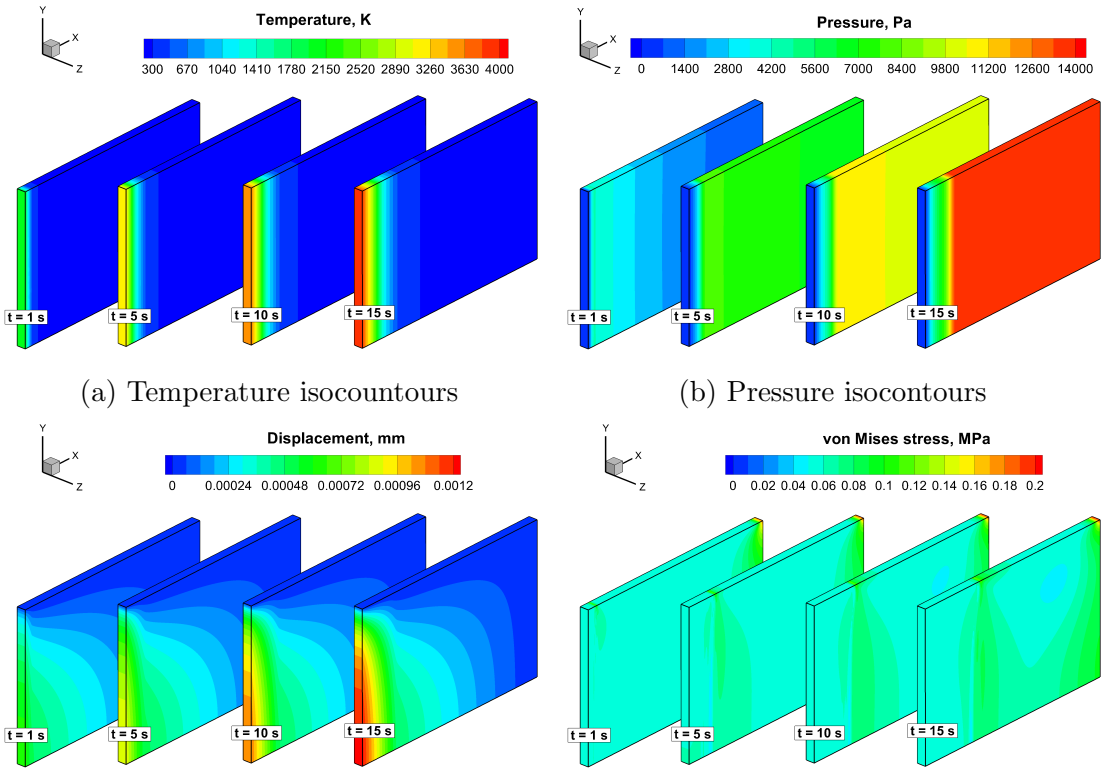

(a) Temperature isocountours

(b) Pressure isocontours

(c) Displacement isocontours

(d) Von Mises stress isocontours

Figure 4.6: Isocontour results for $t \in [1, 15]$ s for various quantities for impermeable top surface case

tion of the displacement, when compared to the permeable wall case. However, the "pulling" effect is weaker than the case of the permeable wall, with a maximum value around 0.0012 mm. As a result, in Fig.4.7c the von Mises stress becomes even smaller compares to the previous case with a maximum value of 0.07 MPa.

4.6 Conclusion

In this chapter, the internal pressure produced by pyrolysis gas has been investigated through a one-way coupling approach. Using the same approach as the thermo-mechanical coupling described in Chapter 3, the internal pressure field is transferred to the structural response, which allows the calculation of displacement and stress. To simplify the problem, the porous media is assumed to be treated as bulk material

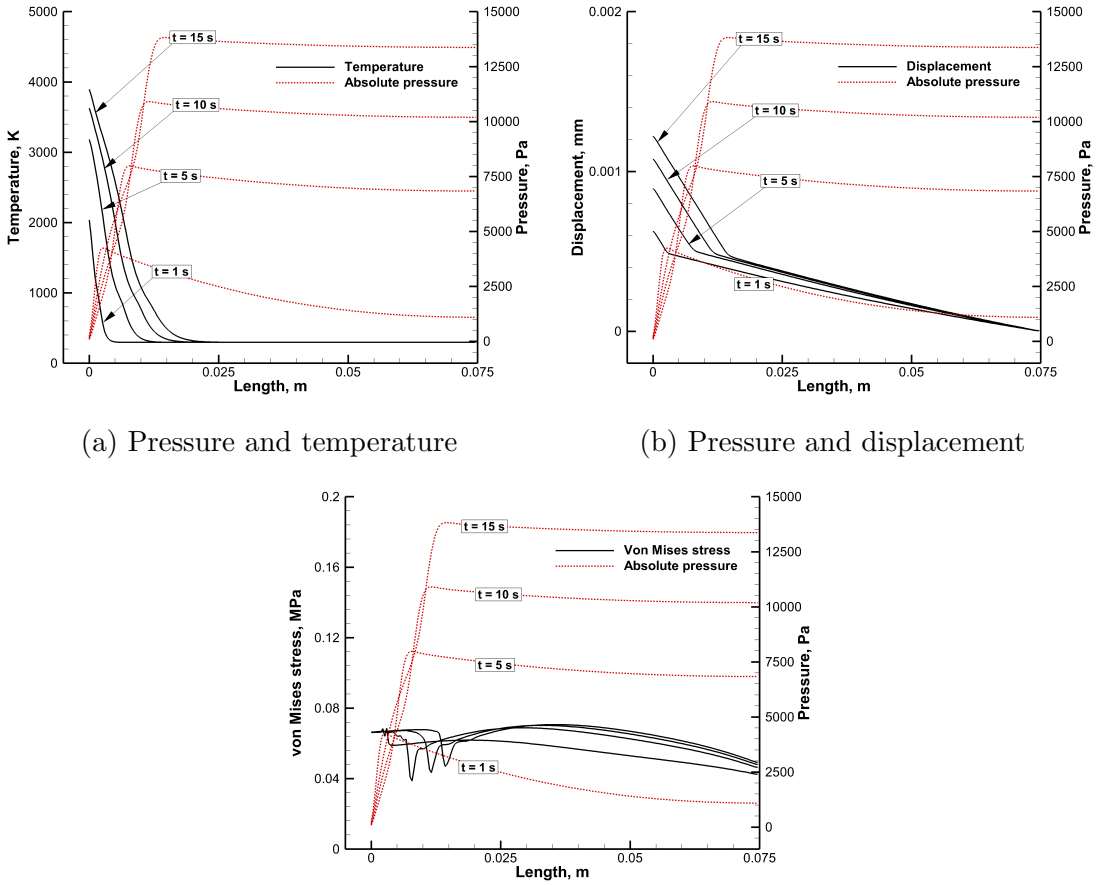

(a) Pressure and temperature

(b) Pressure and displacement

(c) Pressure and von Mises stress

Figure 4.7: Results comparisons among temperature, displacement, von Mises stress and internal pressure for impermeable top surface case

with uniformly distributed pores and these pores are interconnected so that pyrolysis gas can flow through.

Using this model on charring ablation cases, the internal pressure and resulted displacement are investigated. By changing the boundary condition of the top surface from permeable to impermeable, the internal pressure distribution changes significantly. For permeable case, internal pressure shows both negative and positive value in char and virgin respectively. For impermeable case, the internal pressure keeps increasing. The pyrolysis gas plays a same "pulling" effect on the TPS material for both cases. However, the resulted displacement and stress are small enough to be

ignored during stress analysis.

It is, however, not safe to conclude that the internal pressure will not cause any damages to the material. In reality, porous media, especially for TPS material, is far from perfectly isotropic and uniform. In addition, pores are likely to form sealed chamber within the material where pressure can build up rapidly as ablation process continues. Although the number of localized pressure build-up is limited, these micro-scale pressure chamber can form burst and cracks. As a result, some TPS may fail and be ejected into the flow field before becoming fully charred. With this in mind, future work could focus on developing more realistic material models with a more accurate pores distribution.

Chapter 5: Moving Mesh Scheme in KATS

In this chapter, the moving mesh scheme used in KATS structural response module is described with detailed scheme and demonstration cases. A short introduction of moving mesh approach will be given at the beginning. Then, detailed descriptions are provided with a demonstration case on how to deform the mesh. Next, demonstration cases of 1D, 2D and 3D computation grid will be provided to show the ability to handle complex geometries. Then, this method will be applied to a coupled thermo-mechanical modeling case. Finally, the moving mesh scheme will be applied to a charring ablation case to see how TPS material deforms when subjected to heat flux.

5.1 Introduction

The successful development of the one-way thermo-mechanical solver leads to additional questions on how to capture the deformation and its associated effects. In pure structural modeling, the material usually deforms under certain loads. This deformation can be undesirable because it causes cracks and gaps between different components. For thermal expansion, the local strain can lead to large thermal stress which can also cause material fatigue and failures. In order to study those mechanisms, it becomes necessary to develop a moving mesh scheme and coupled it into the structural response module.

5.2 Computation domain techniques - moving mesh

In this section, a demonstration case is presented to show the detailed scheme used for interpolations between cell center and grid node. The material used in this chapter is steel with properties given in Table 3.1. Since the purpose is to demonstrate mesh

movement, the steel is considered unbreakable under any mechanical loading.

5.2.1 Demonstration case - 2D plate compression

Figure 5.1 shows the loading functions. As it is illustrated, the displacement load follows a 1 second Sine function with a maximum 0.5 m displacement. The boundary conditions and computation grid are provided in Fig. 5.1b. For this 2D plate, the front surface is subjected to a displacement load. The end wall is fixed support. Two side walls are set to free surfaces, which means they will move according to the interior part of the plate. In order to better visualized the deformation, an area identified on Fig. 5.1b with a red rectangular is picked. This area is called the "study area".

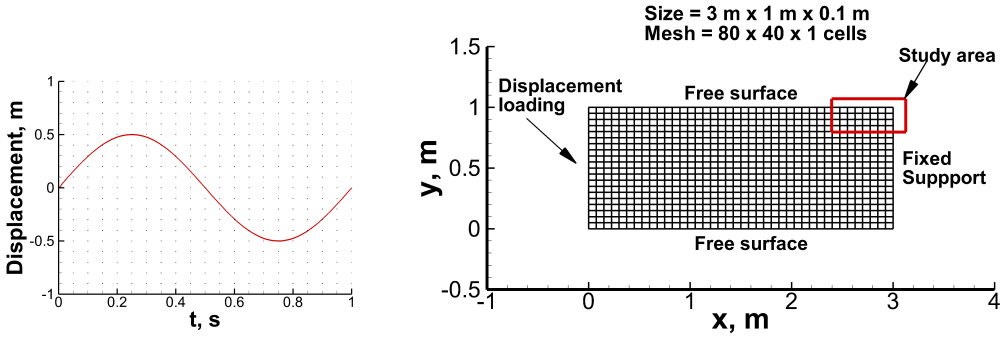

(a) Loading function (b) Boundary condition and geometry

Figure 5.1: Moving mesh scheme illustration case with loading function, boundary conditions and computation grid.

In order to illustrate moving mesh scheme for finite volume framework, the definitions of cell, face and node must first be clarified. In a FVM framework, node is the basic element representing a point in space. Three or four nodes, are connected together to form a face. And as a result, a number of faces from a cell. For this 2D case, 2 nodes form a face, and 4 faces form a cell. A cell center is the spatial center of a closed 4 faces.

Figure 5.2 shows the previously mentioned study area with labels for nodes and cells at the $t = 0$ s. Two random nodes, shown as yellow circles, M and N, are chosen

for the representation of interior node and boundary node respectively. Their neighboring cell centers shown as blue squares, have also been labelled as a combination of i and j. In this figure, at $t = 0$ s, there is no movement for all the cells and nodes.

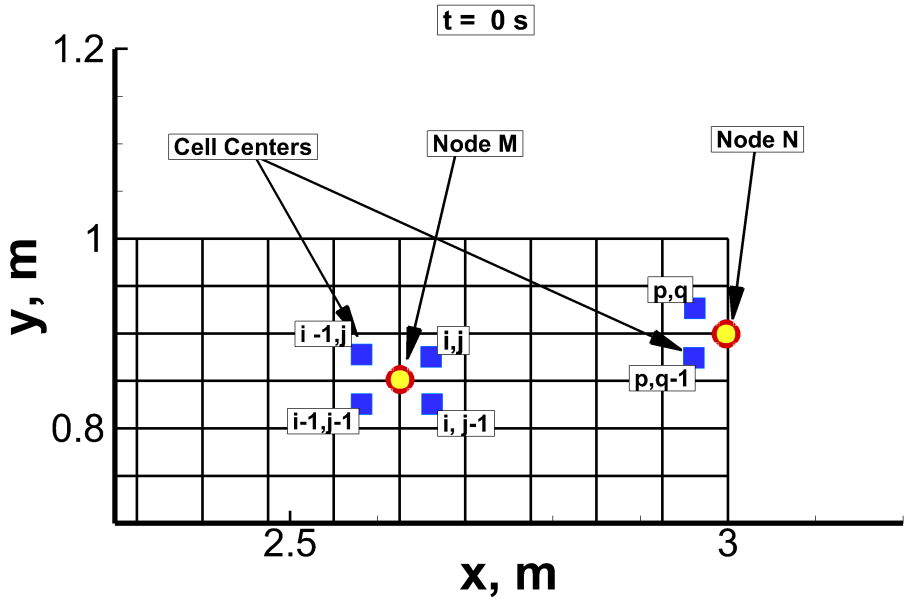

Figure 5.2: Detailed illustration of upper right corner of the geometry with test cells and nodes identified.

Figure 5.3 shows the deformed mesh and corresponding nodes and cells at $t = 0.1$ s. Since the loads at this time is compressing the plate, all the nodes and cells are moving toward upper right. For node M, the amount of movement is calculated by a weighted average of surrounding cells $cell_{i,j}$, $cell_{i,j-1}$, $cell_{i-1,j}$ and $cell_{i-1,j-1}$. In this 2D case, all the movements of interior nodes are calculated according to this methodology. It can be observed that even for this coarse mesh, the grid deforms very smoothly without any unexpected changes in geometry.

For node N, the calculation is different. Nodes on the boundary are all calculated by using the surrounding face centers. Since this node is on the end wall where all the displacement is fixed, there is no movement on its surrounding faces. That is why the displacement on node N is zero. On the contrary, all the nodes on the side wall show a move toward upper right because they represent the free surface. All the

faces are free to move thus have a non-zero displacement. In this way, the amount of movement on those nodes are weighted averaging of neighboring faces.

It should be noted that the cells $cell_{p,q}$ and $cell_{p,q-1}$ did move after this compression. Even though the faces on the boundary do not move, the cell are still affected by the rest of the domain. Therefore, the solutions of displacement are not zero for these two cell centers.

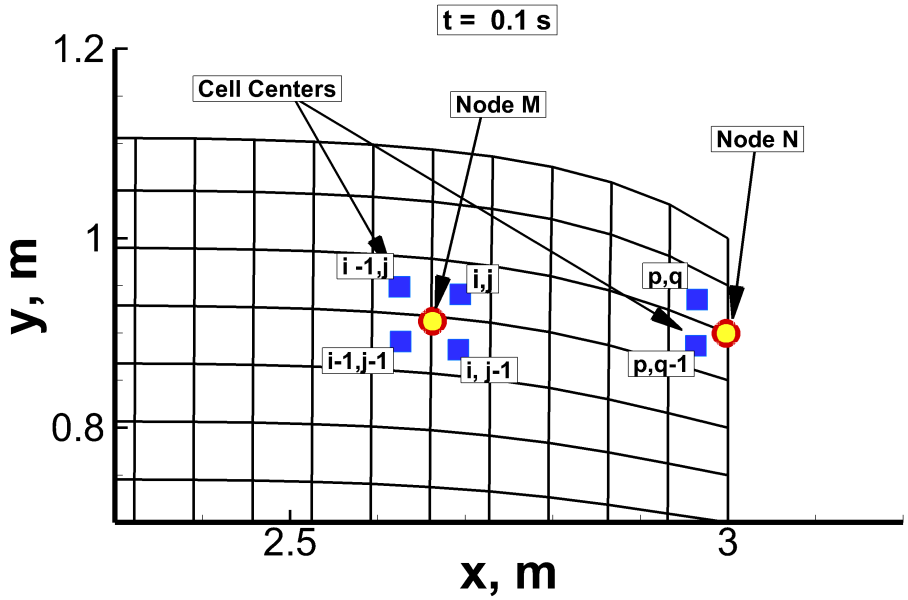

Figure 5.3: At $t = 0.1$ s, the plate is compressed with a deformation toward upper right corner

Several remarks should be made regarding the moving mesh scheme for any kind of application. The first one is that deforming computation grid dose not only serve as a visualization tool. Since the movement represents the actual deformation of solid material, parameter such as mass, must be conserved within a cell. Also, all the spatial related parameters, such as cell volume, face area, face norms and spatial gradient need to be updated after each deformation, for each time step. This can be very time-consuming if the computation grid contains millions of cells. Since there is a change in geometry, volumetric strain should be calculated accordingly. The criteria

on whether or not to take into consideration the strain effects on material properties such as conductivity, should be also carefully studied.

5.3 Moving mesh demonstration cases

In this section, a series of demonstration cases are provided to show the ability of this mesh moving approach of handling multi-dimensional problems. First, a 1D case is presented to show the accurate movement on boundaries. Then, a 2D case similar to the previous illustration case is provided to show Poisson effects of compression and extension on free surface. Finally, a 3D case is used to show a stronger Poisson effects and the 3D capabilities of the algorithm.

5.3.1 1D demonstration

For this first case, a steel bar is used. Figure 5.4 shows the loading function as well as the boundary conditions, dimension and computation grid. The steel bar has one end fixed while the other end is given a displacement load. In this case, the loading function is set to be a Sine function of 1 second so that compression and extension are applied. The maximum displacement, representing maximum compression, occurs at $t = 0.25$ s, and the minimum displacement, representing maximum extension, occurs at $t = 0.75$ s.

Figure 5.5 presents the results during the compression. At the beginning, in Fig. 5.5a, the bar is at rest with zero displacement for all nodes and cells. Then in Fig. 5.5b as the front surface is being compressed , the bar is compressed uniformly to the right. In Fig. 5.5c as time elapses, the bar is further compressed with a maximum displacement of approximately 0.9 m. Finally in Fig. 5.5d at $t = 0.25$ s, maximum displacement is reached as the front surface is compressed at exactly $x = 1$ m with still uniformly distributed spacing.

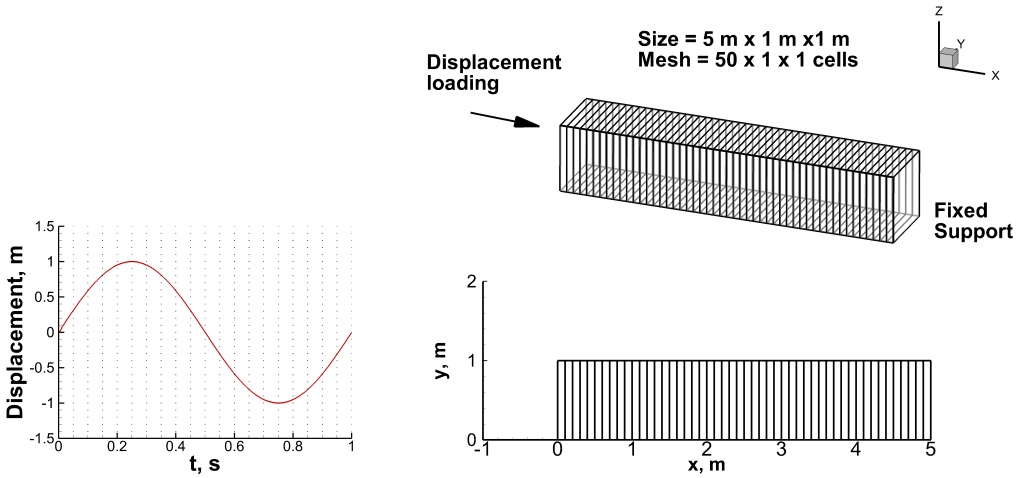

(a) Loading function (b) Boundary condition

Figure 5.4: Moving mesh 1D demonstration case setup

Figure 5.6 shows the results for the bar in the extension. By the nature of Sine function, when $t = 0.5$ s, the displacement load is zero, which makes this bar is back into its initial state, shown in Fig. 5.6a. As the loading function keeps being applied, the bar is extended to the left, as shown in Fig. 5.6b, with the same uniformly distributed displacement for each element. In Fig. 5.6c, the bar is further extended with a maximum extension of approximately -0.9 m. Finally at $t = 0.75$ s, maximum extension reached to exactly $x = -1$ m in Fig. 5.6d.

Several observations can be made regarding this 1D case. First, since this is a 1D geometry, all the nodes are on boundary faces. Thus, the movement on front face should be exactly the same amount as the loading function, as is observed in the results. Also, no movement should be observed on y or z direction, which can also be confirmed by the results. In addition, because the movement of each node obeys steady-state equilibrium, the movements are uniformly distributed within this steel bar, which also shown in the results.

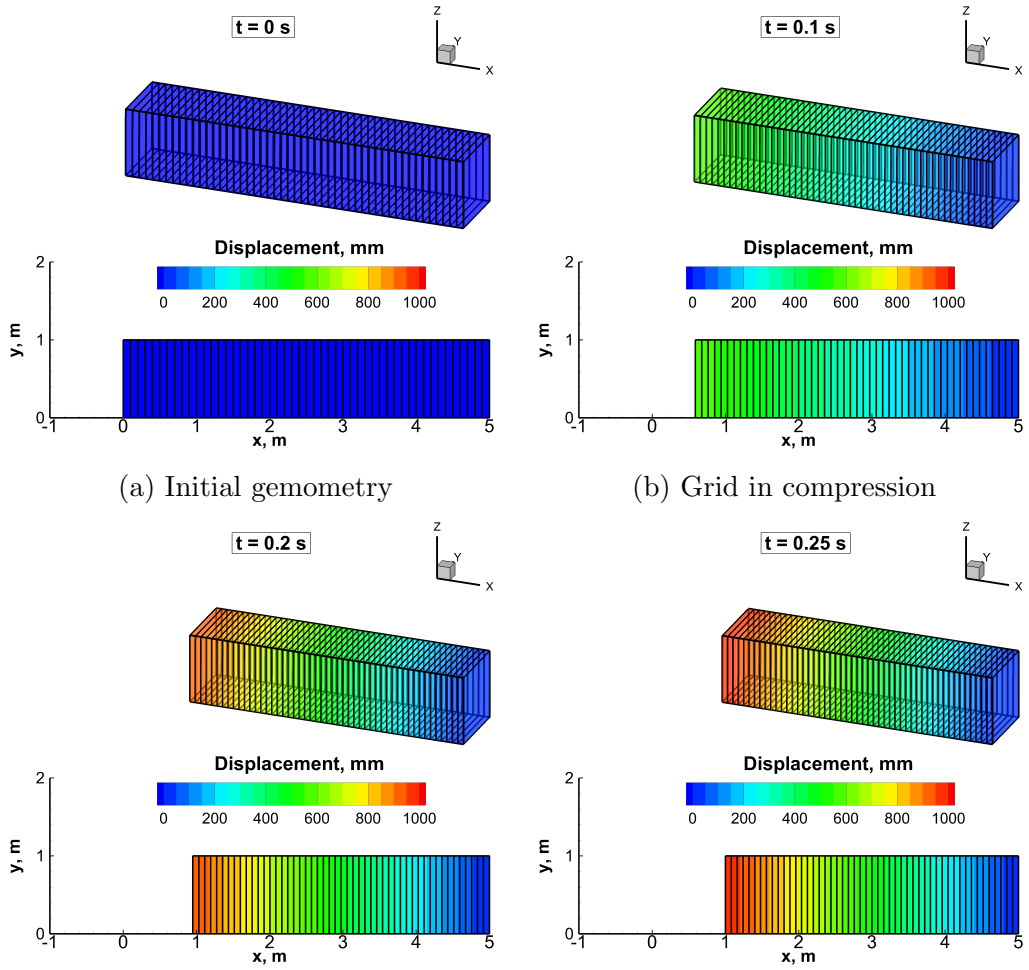

(a) Initial gemometry

(b) Grid in compression

(c) Compressed at $t = 0.2$ s

(d) Grid is compressed to final state

Figure 5.5: Moving mesh demonstration case. Grid deformation of 1D mesh in compression stage

5.3.2 2D demonstration

The second case is identical to the first one, but is now in 2D. Figure 5.7 shows the loading function as well as the boundary conditions, dimension and computation grid. The displacement is applied following the same Sine function as in the previous case. The front surface ($x = 0$ m) is subjected to the loading, and the right wall ($x = 5$ m) is set as a fixed support. Two side wall are set to be free surface. It should be noted that, in this 2D case, Poisson effects are expected to be observed on the side walls as opposed to the 1D case.

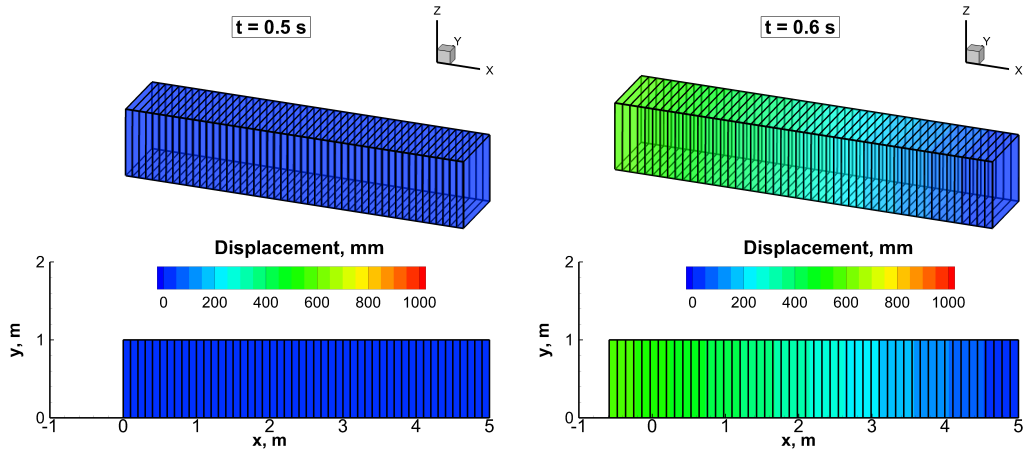

(a) Initial gemometry (b) Grid in extension

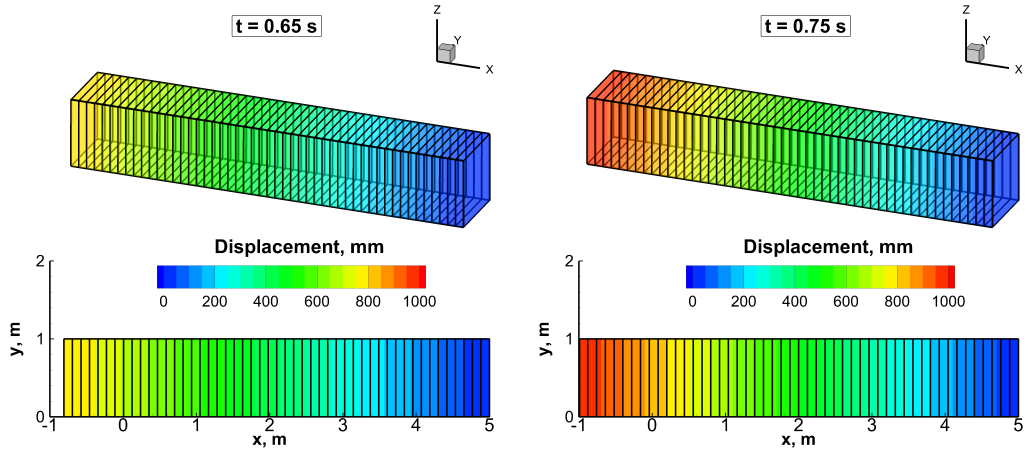

(c) Extended at $t = 0.65$ s (d) Grid is pulled to final state

Figure 5.6: Moving mesh demonstration case. Grid deformation of 1D mesh in extension stage

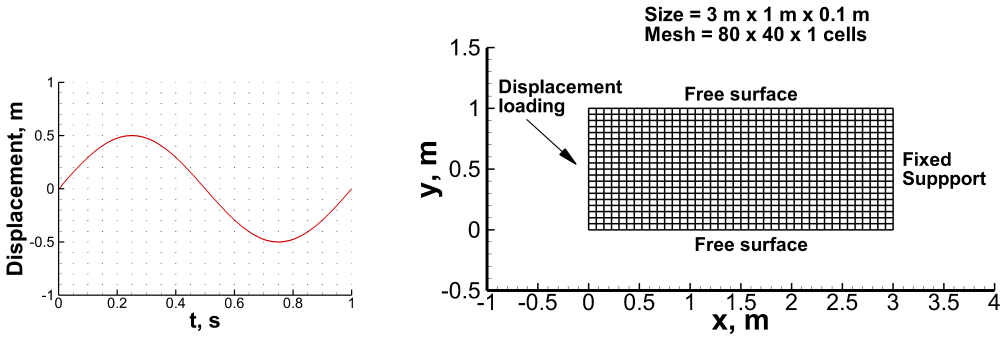

(a) Loading function (b) Boundary condition

Figure 5.7: Moving mesh 2D demonstration case setup

Figure 5.8 shows a series deformation results in the compression phase. At the beginning in Fig. 5.8a, all the cells and nodes are at rest with zero displacement. At $t = 0.1$ s, the plate is compressed to about 0.3 m, as shown in Fig. 5.8b. It can be observed that two side walls expand in the y direction as a result of Poisson effects. In Fig. 5.8c, stronger expansion of two side walls is observed since the plate is further compressed to about 0.45 m. Finally, in Fig. 5.8d, the plate is at maximum compression, and the $x-$displacement on front surface is exactly 0.5 m.

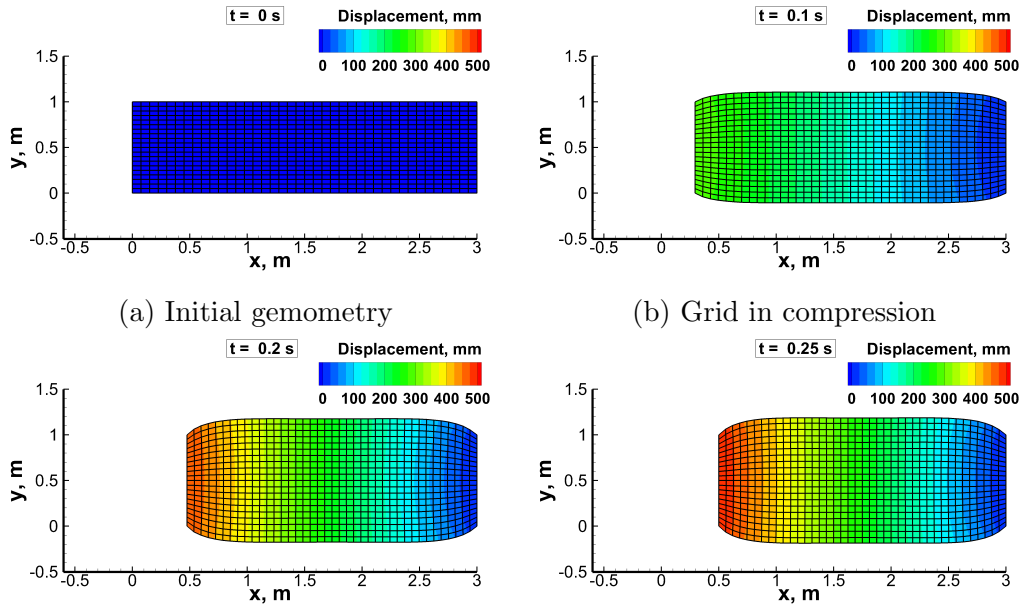

(a) Initial gemometry

(b) Grid in compression

(c) Compressed at $t = 0.2$ s

(d) Grid is compressed to final state

Figure 5.8: Moving mesh 2D demonstration case; grid deformation in the compression phase

Figure 5.9 shows a series of results in extension stage. At $t = 0.5$ s shown in Fig. 5.9a, the plate restores to its original shape and all the displacements are zero. At $t = 0.6$ s shown in Fig. 5.9b, the displacement loading becomes negative and plays a pulling effect on the plate. It can be observed that two side walls contract inwardly because of the Poisson effect. When $t = 0.65$ s, the plate is further pulled to its left as illustrated in Fig. 5.9c, with a maximum displacement around 0.4 m. Finally at $t = 0.75$ s shown in Fig 5.9d, this plate is pulled to the position at exactly $x = 0.5$

m. Stronger contracting effects on two side walls can be seen.

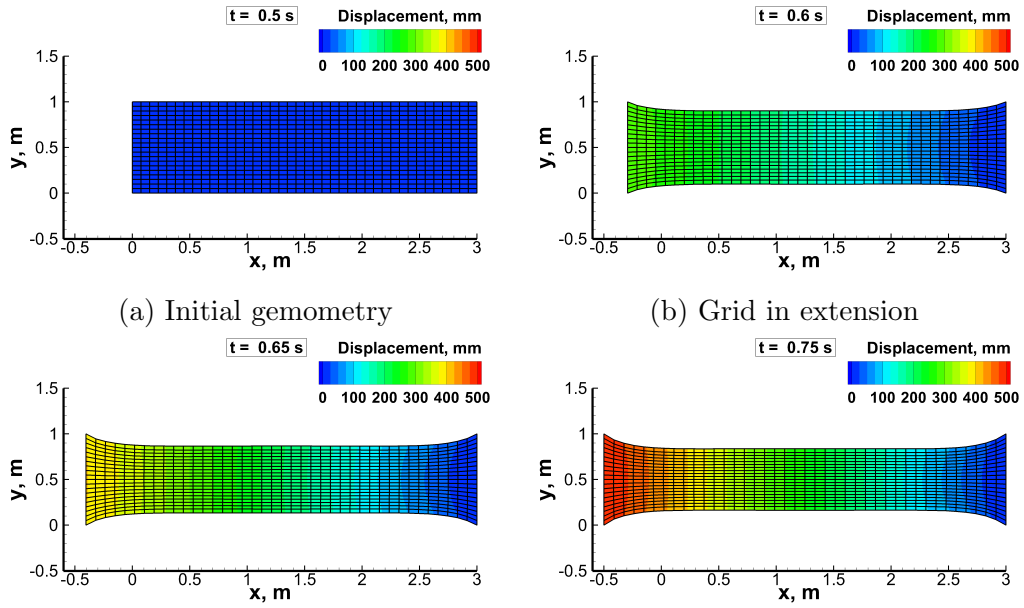

(a) Initial gemometry

(b) Grid in extension

(c) Extended at $t = 0.65$ s

(d) Grid is pulled to final state

Figure 5.9: Moving mesh 2D demonstration case; grid deformation in the extension phase

In this 2D demonstration case, all the loads and boundary conditions are the same as in the illustration case. Thus, detailed discussion for this case can be found in Sec. 5.2.

5.3.3 3D demonstration

Figure 5.10 shows the loading function, the boundary conditions and computation grid. The loading function is the same in 2D case. This test-case consists of a steel cuboid with the front surface subjected to a displacement loading, while the bottom surface is fixed. The four side walls are set to free surfaces. As with the previous cases, more obvious Poisson effects are expected on the side walls during both compression and extension stages.

Figure 5.11 shows the deformation results in the compression phase. The contour plots show the total displacement, which is the norm of $\vec{u}$. In Fig. 5.11a, at $t = 0$ s,

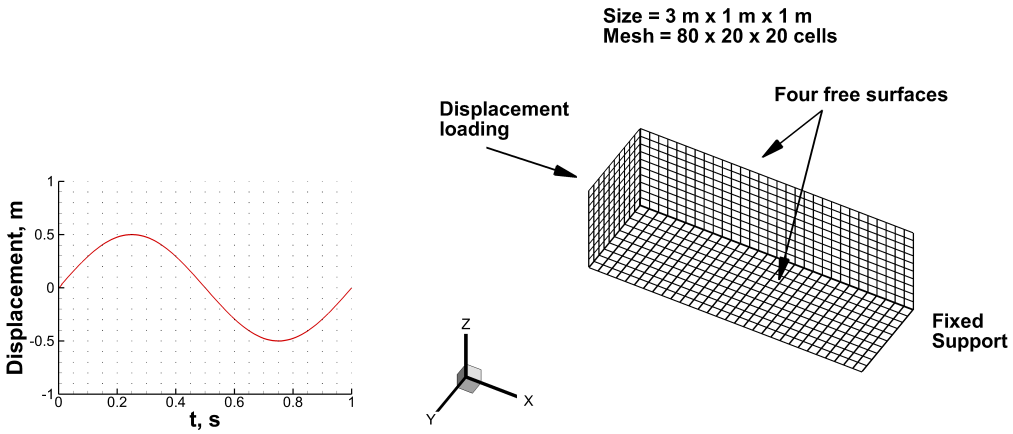

(a) Loading function (b) Boundary condition

Figure 5.10: Moving mesh 3D demonstration case setup

no movement for all cells and nodes. In Fig. 5.11b, at $t = 0.1$ s, the front surface is compressed to approximately 0.3 m, and an expansion can be observed on side walls. In Fig. 5.11c, at $t = 0.2$ s, the cuboid is further compressed to approximately 0.45 m and all side walls expand outwardly. In Fig. 5.11d, at $t = 0.25$ s, the compression reaches a maximum value of 0.5 m.

Figure 5.12 shows the results in the extension phase. At $t = 0.5$ s, in Fig. 5.12a, the cuboid restored from compression and all displacements are zero. At $t = 0.6$ s, in Fig. 5.12b, the loading becomes negative to its original form and side walls contract inwardly. At $t = 0.65$ s, in Fig. 5.12c, the cuboid is further extended to 0.4 m with a stronger contracting effect on the side walls. Finally at $t = 0.75$ s in Fig. 5.12d, cuboid reaches a maximum extension with a displacement of 0.5 m. As shown in these contour plots, the deformations are distributed uniformly within this cuboid.

Several remarks should be made for the moving mesh cases. First, the contour plots are based on the total displacement result, which is calculated as the norm of $\vec{u}$. Moreover, moving mesh algorithm for 3D is much more complex than 1D or 2D case since more cell centers and nodes are taken into consideration. Finally, the deformation results obey the equilibrium equations, which makes the deformation

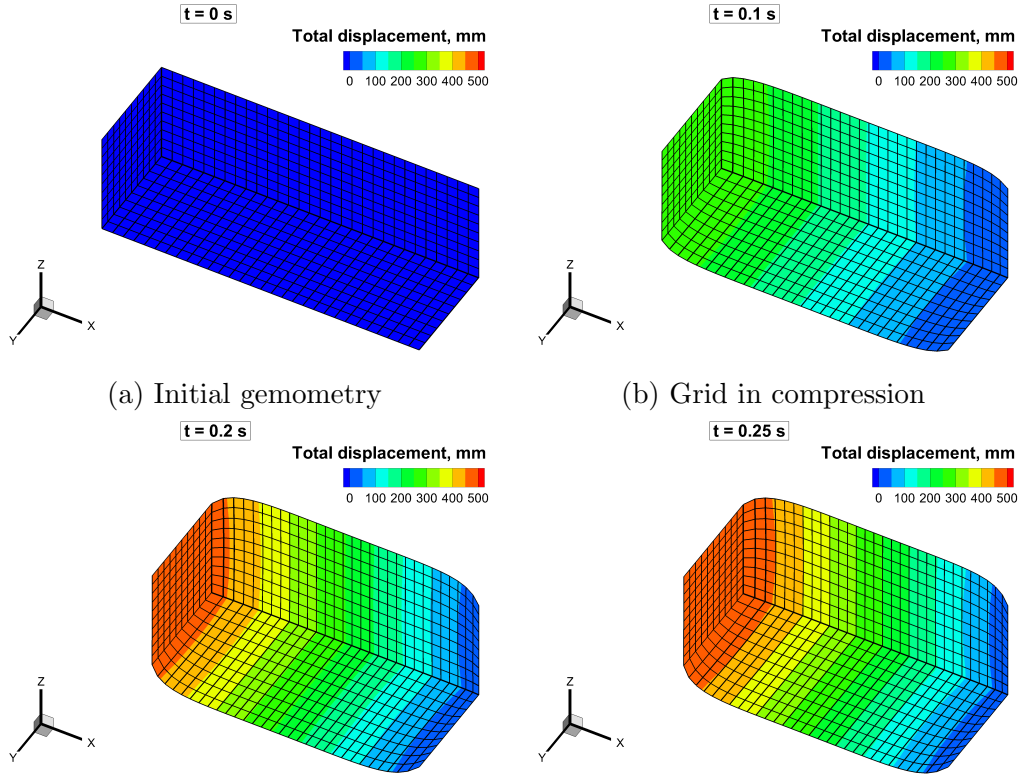

(a) Initial gemometry

(b) Grid in compression

(c) Compressed at $t = 0.2$ s

(d) Grid is compressed to final state

Figure 5.11: Moving mesh 3D demonstration case. Grid deformation in compression stage

physically distributed on the computation grid.

5.4 Moving mesh application - heating of a steel plate

In this section, the developed moving mesh scheme is applied to a thermo-mechanical coupling case to demonstrate its ability to capture the thermal expansion and changes in shape. In order to perform such application, the moving mesh scheme obtains the displacement values from structural response module and all the geometric parameters are updated based on the displacement field. Then, the density for each cell is calculated according to the changing cell volume to ensure the mass conservation for each cell. Thus, this case consists of a two-way coupling demonstration case.

Figure 5.13 shows the case setup, a plate made of steel with length and width of

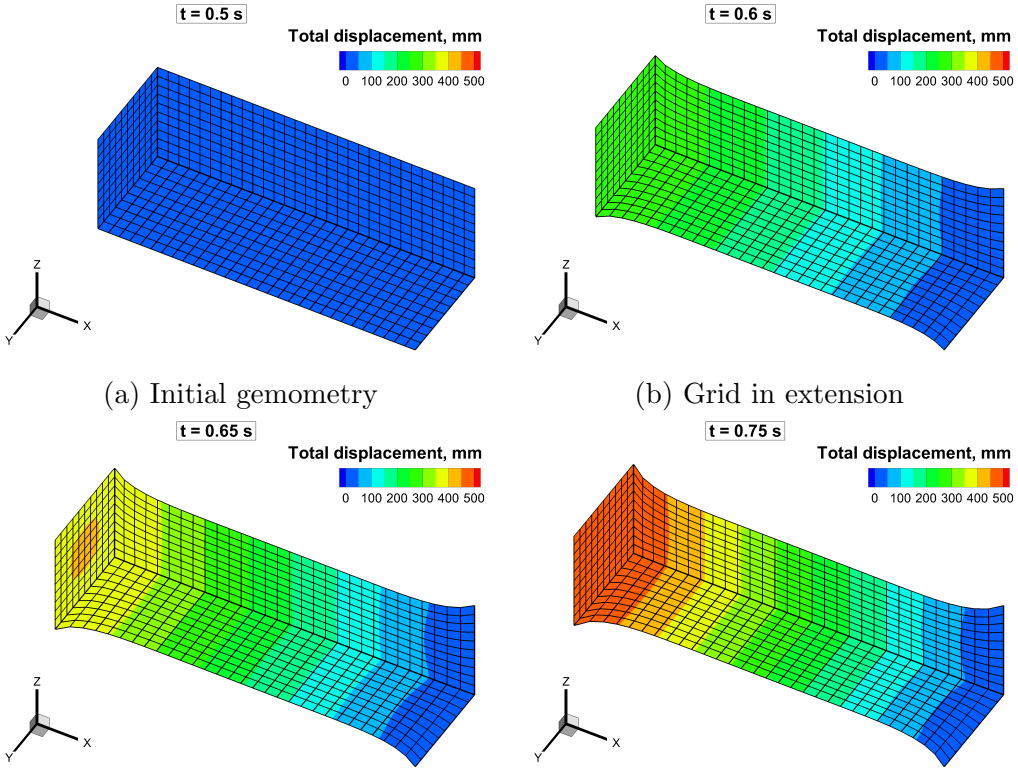

(a) Initial gemometry

(b) Grid in extension

(c) Extended at $t = 0.65$ s

(d) Grid is pulled to final state

Figure 5.12: Moving mesh 3D demonstration case. Grid deformation in extension stage

3 cm x 1 cm. The front surface is subjected to a heat flux and the end surface is at room temperature and fixed support. The other faces are all adiabatic and with constant constraints as indicated. The computational grid is refined near the surface, where heat flux is applied, since larger gradients are expected in this area. Because the bottom surface is constrained in the $y-$direction, the plate is expected to expand toward the upper left corner.

Figure 5.14 shows the displacement contours, where vectors indicating the directions of deformation. It should be noted that the magnitude of the displacement is very small with a maximum value of 0.04 mm. Thus, the deformation is multiplied by 100 times to better visualize. At $t = 1$ s, the plate shows very mild deformation on the corner. As the front surface is being heated constantly, at $t = 5$ s, significant expansion can be observed on the front part of the plate. Finally, at $t = 10$ s, stronger

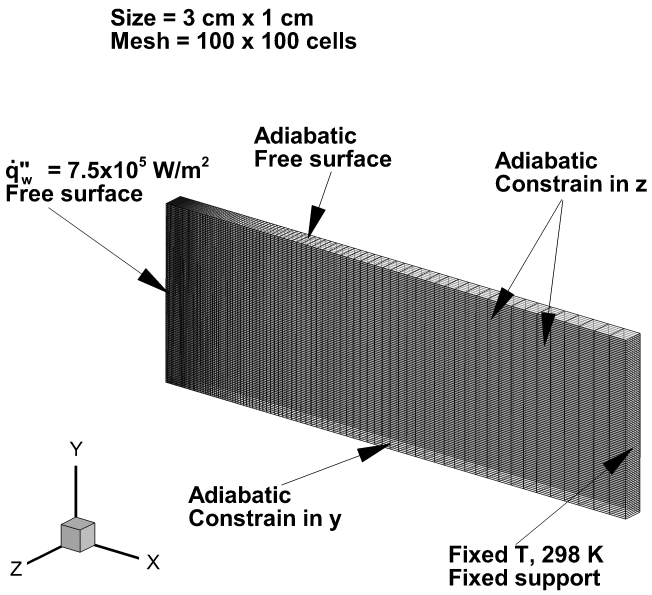

Figure 5.13: Moving mesh application case. Dimensions, boundary conditions and computation grid for coupled heating of a steel plate

expansion on the front surface can be seen and the whole plate shows a uniformly distributed expansion.

Figure 5.15 shows the results of temperature isocontours on the gradually deformed geometry. At $t = 1$ s, the plate has not absorbed much heat, and the temperature changes are located near the surface, and the plate barely deforms. At $t = 5$ s, as the heating effect becomes more obvious, the temperature at front surface reaches about 430 K and the geometry is now clearly deforming. At $t = 10$ s, the front surface reaches maximum temperature of 470 K with significant thermal expansion on the front part.

Several remarks should be made for this coupled case. First, the displacement and temperature results are verified in Chapter 3, and therefore assumed to be correct. It should also be noted that Second, in order to have a better visualization of the results, the deformation is magnified. In this case, because all the displacement results are obtained before deforming the mesh, it is easier to choose an appropriate

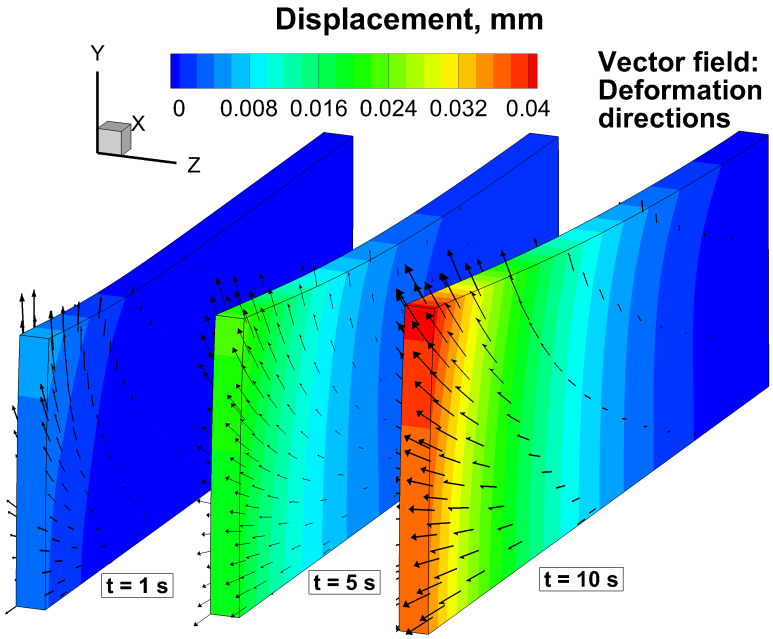

Figure 5.14: Displacement isocontours results. Plate expands to upper left corner because of the thermal expansion

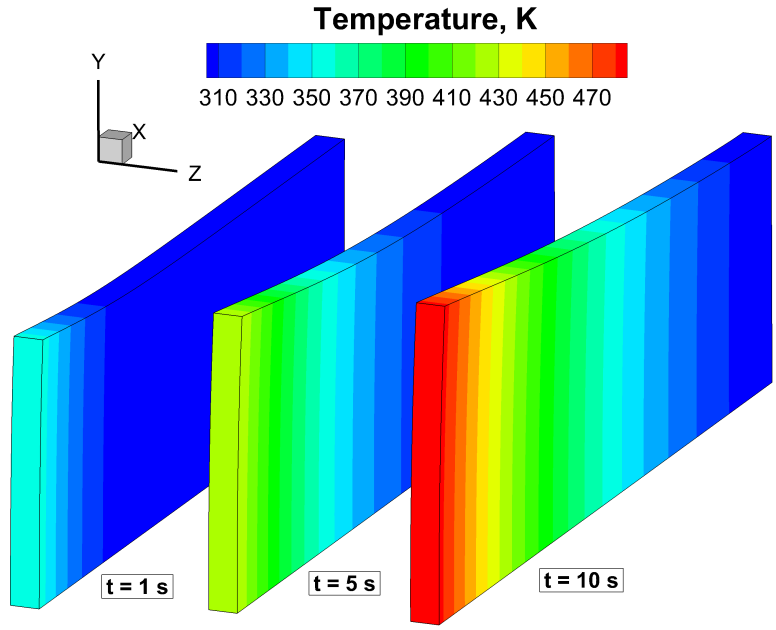

Figure 5.15: Temperature isocontours results. Plate expands to upper left corner because of the thermal expansion

multiplier. Last, although the thermal response calculates the temperature field using the deformed mesh, the temperature field is still distributed uniformly. This is because the actual changes is small and the effects of changing the density and geometric parameters have little or no impact on the heat conduction. In a word, the impact on thermal response from structural changes are limited in this case. However, if the strain effects on the material properties are considered, the temperature field is expected to be nonuniform. The strain effects caused by thermal expansion will be discussed in Chpater 7.

5.5 Moving mesh application - carbon phenolic charring ablator

In this section, the moving mesh scheme is applied to a charring ablation case with non-uniformly distributed temperature profile and temperature-dependent material properties. For this case, the deformation is expected to be more complex, thus validate the robustness of the moving mesh scheme.

The material used for this case is TACOT, with thermal properties provided in Ref. [88]. Since no mechanical properties are published for TACOT, the values for a similar material, obtained from Ref. [38], are used. The tabulated values for both the Young's modulus and the CTE are given in Table 3.4. All the properties for the char state are listed in Table 3.5.

The geometry and boundary conditions are presented in Fig. 5.16. The front surface ($x = 0$ m) is subjected to a constant heat flux of $\dot{q}''_w = 7.5 \times 10^5$ W/m^2, and a constant pressure of $p = 101,325$ Pa. The back wall ($x = 0.075$ m) is assumed to be adiabatic and impermeable. The side wall ($y = 0.05$ m) is considered adiabatic, permeable, and with a fixed pressure identical to the front surface pressure. The rest of the thermal boundaries, including $y = 0$ m, $z = 0$ m, and $z = 0.005$ m, are set to symmetry planes. For the structural boundary conditions, the back wall ($x = 0.075$ m) is set as fixed support, the front wall and the side wall are set as free surfaces

with no constraint, and the rest of the walls are constrained as shown in Fig. 5.16. It should be noted that since the upper side wall is permeable, temperature field is expected to be non-uniform and the bottom surface is constrained in the $y-$direction, the plate is expected to expand to its upper left corner, similar in the previous case.

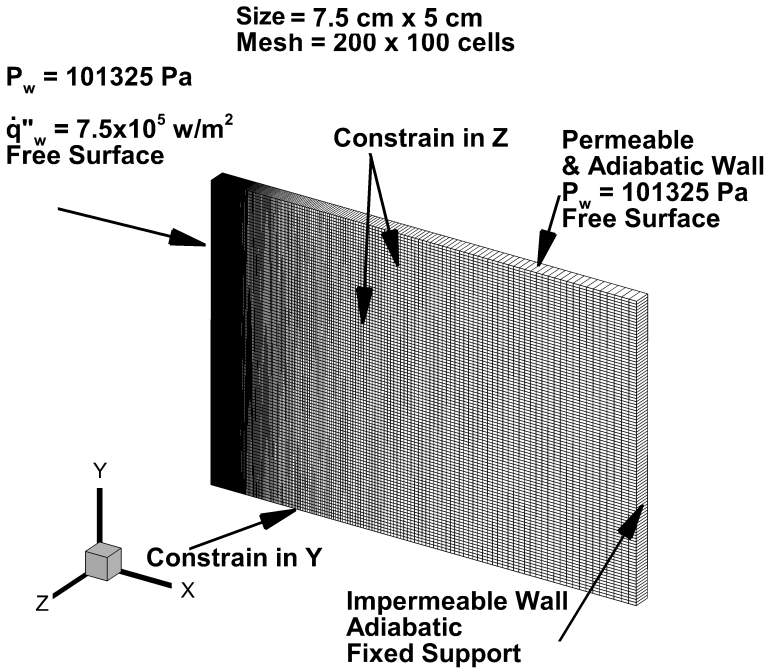

Figure 5.16: Moving mesh application case. Boundary conditions, dimensions and computation grid for charring ablation

Figure 5.17 shows the isocontours of temperature, displacement, density and von Mises stress. Results are at $t = 1, 5, 10$ and 15 s, to show the time evolution of solutions. Figure 5.17a presents the evolution of temperature and the location of stress concentration where stress exceeds 100 MPa. It can be observed that the contour line is slightly deformed on the upper side wall. Figure 5.17b provides the evolution of displacement field as well as the stress concentration area. It can be seen that the upper left corner deforms with a largest value around 0.85 mm. Figure 5.17c presents the evolution of solid density. During the ablation process, virgin is heated and charred and as a consequence, density decreases to approximately 220 Kg/m^3.

Figure 5.17d provides how von Mises stress evolves during the ablation process. In this figure, the are of high stress concentration is located where the temperature ranges from 350 K to 700 K.

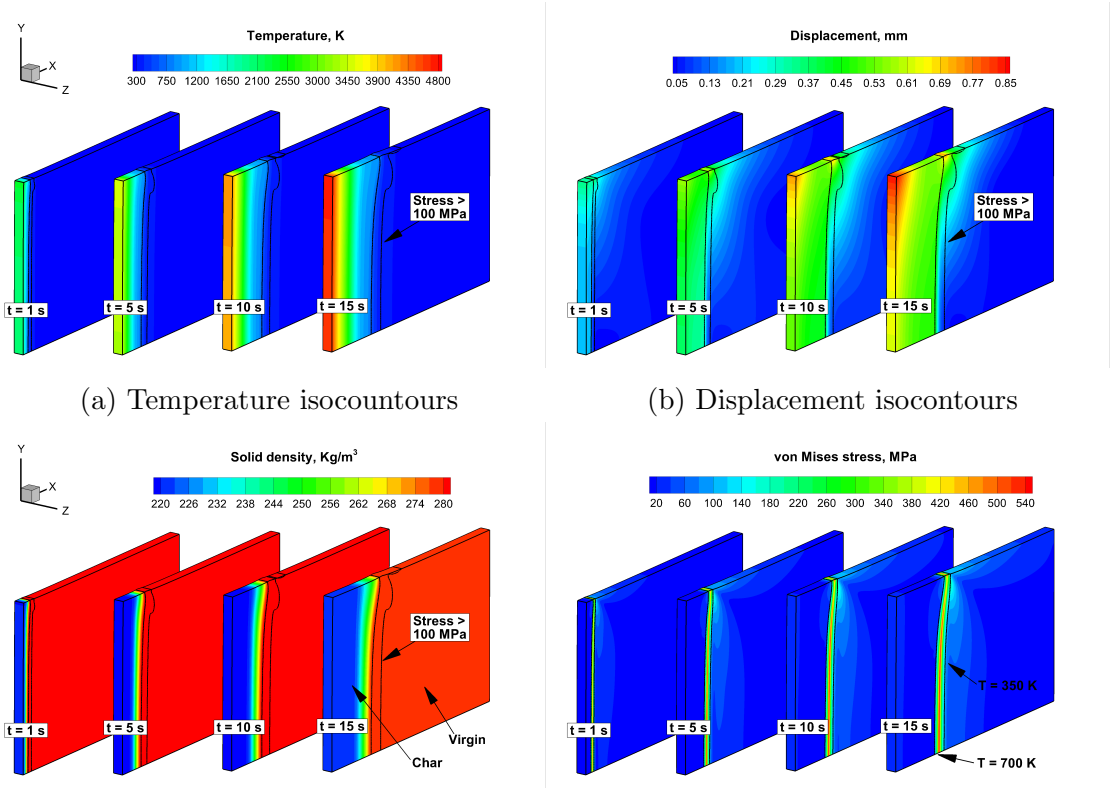

(a) Temperature isocountours

(b) Displacement isocontours

(c) Density isocontours

(d) Von Mises stress isocontours

Figure 5.17: Various isocontours results for charring ablation case. Very slightly deformation can be observed on the plate

Because the maximum displacement is relatively small, with a value of 0.85 mm, the results at $t = 15$ s are closely examined in Fig. 5.18 to allow a better visualization of the deformation. In this figure, three locations-the lower left corner, the upper left corner and the side wall-are chosen to show more detailed deformation. At the lower left corner, the front surface expands to its left with about 0.5 mm. At the upper left corner, the maximum displacement has a value of 0.85 mm. This figure clearly shows the traction effects caused by the thermal expansion. Another interesting deformation occurs at the side wall where stress concentrates. The deformation pattern at this location differs from the other two. It is a ripple-like distribution with a maximum

value of 0.7 mm. Because of this deformation, more areas is exposed to external flow field, and this area could be subjected to more heating and shear force coming from the flow field.

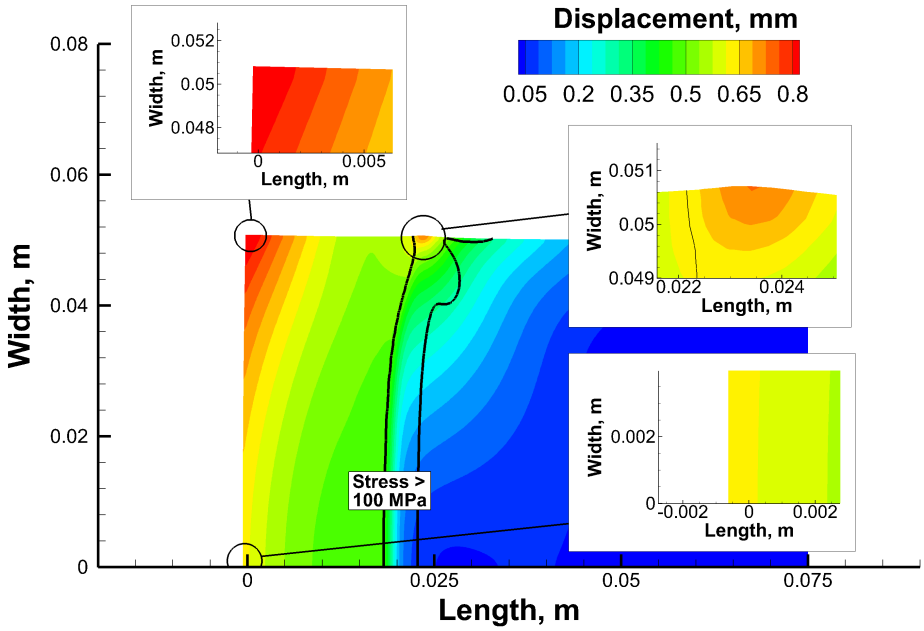

Figure 5.18: Detailed distribution of displacement at $t = 15$ s. Three locations are picked to plot with more precision to show how mesh deforms

5.6 Conclusion

The detailed approach of moving mesh module is described with multiple demonstration cases and application cases. By presenting a 2D demonstration case, the method used in interpolating displacement from cell centers to cell nodes was described. Then, a series of demonstration cases in 1D, 2D and 3D were provided to show the abilities of the scheme to handle multi-dimensional problems. This scheme was then applied to a thermo-mechanical coupling case to show the effects of thermal strain on grid deformation. Then, a more complex application, using charring ablation case, was performed. All of the results show that the moving mesh scheme is robust and can be applied to more complex problems.

In this study, the displacement results are stored and transferred to the deformation of the computation grid. Because the geometry is constructed using nodes and the FVM stores information on cell centers, interpolations between cell center and node are inevitable.

Another concern for the moving mesh scheme is the coupling frequency. Because the computational grid changes, all the geometric parameters such as cell volume, face center and area, norms of each faces are also needed to be re-calculated. In addition, a large portion of solver used a stored spatial gradient map to calculate gradient of primitive variables, this map also needs to be updated. Sometime this process can be time-consuming. Thus, on what frequency the grid is needed to be updated with deformation should be investigated very thoroughly.

Chapter 6: Two-way coupling framework and coupled thermo-mechanical parameters

6.1 Introduction

1D modeling serves as an essential tool in the development of large scale computation code because of its extensibility and simplicity. Major advantage of a 1D model is that it can be rapidly developed due to the simplified mathematical formulation. It simplifies complex three dimensional governing equations without the loss of principle behaviors. A large amount of partial differential equations collapses into ordinary differential equations such as the Poisson equation, which is solved in this chapter. Therefore, 1D model also enables a much easier implementation with respect to programming. Another benefit comes from the fact that analytical solutions are often obtained in 1D approach, which can provide accurate verification to the model.

For thermo-mechanical coupling, it becomes much easier to manipulate information transfer from one module to the other. Many commercial codes do not include a two-way scheme. There is, however, an increasing demand of a more precise prediction and higher fidelity in simulation for space industry. Thus, a two-way coupling scheme is developed in a 1D Finite Difference Method framework in this chapter.

6.2 Heat conduction equation

The 1D heat conduction equation is provided in Chapter 2, which is represented here for convenience,

$$k\frac{\partial^2 T}{\partial x^2} - \rho c_v \frac{\partial T}{\partial t} + Q = 0 \tag{6.1}$$

This consists of a parabolic partial differential equation with first order time

derivative and second order spatial derivative. Thus, an implicit backward time scheme is employed for the time derivative since it is an 'A-stable' method. As for the spatial derivative, a centered-difference discretization is utilized. Using this process, Eqs. 6.1 becomes,

$$k\frac{T_{i+1}^{t+1} - 2T_i^{t+1} + T_{i-1}^{t+1}}{\triangle x_i^2} - \rho c_v \frac{T_i^{t+1} - T_i^t}{\triangle t} + Q(x_i) = 0 \tag{6.2}$$

where superscript t represents the time; subscript i is the notation for the ith computation grid. And $\triangle x_i$ and $\triangle t$ are length between two neighboring grids and the time step size. $Q(x_i)$ is the heat generation sources within the object. Since this is a standard numerical treatment for heat equations, detailed treatment on boundary conditions and initial conditions is not presented here. Solution can be achieved by utilizing a standard newton's method for equation systems.

6.3 Static equilibrium equation

The 1D static equilibrium equation is also represented here for convenience,

$$(\lambda + 2\mu)\frac{\partial^2 u}{\partial x^2} - (3\lambda + 2\mu)\alpha\frac{\partial T}{\partial x} = 0 \tag{6.3}$$

Because of the quasi-static assumption, there is no temporal term in this equation. The second order derivative term is discretized using the same centered-difference. The temperature gradient term is then directly obtained by solving the temperature field and then transfer the solution to the following equation,

$$(\lambda + 2\mu)\frac{u_{i+1} - 2u_i + u_{i-1}}{\triangle x_i^2} - (3\lambda + 2\mu)\alpha\frac{T_{i+1} - T_{i-1}}{2\triangle x} = 0 \tag{6.4}$$

This results in a diagonal systems of equation which can be solved using a linear matrix solver.

6.4 One-way quasi-static solution

A typical quasi-static solution process for thermo-mechanical coupling is illustrated in Fig. 6.1. First, temperature field is calculated by solving the heat conduction equation. Then, temperature, along with the density and grid information, are transferred to the solid mechanics solver, which solves the static equilibrium equation. The solid mechanics solver, using the temperature field, solves the displacement as primary variables, and outputs the associated stress and strain.

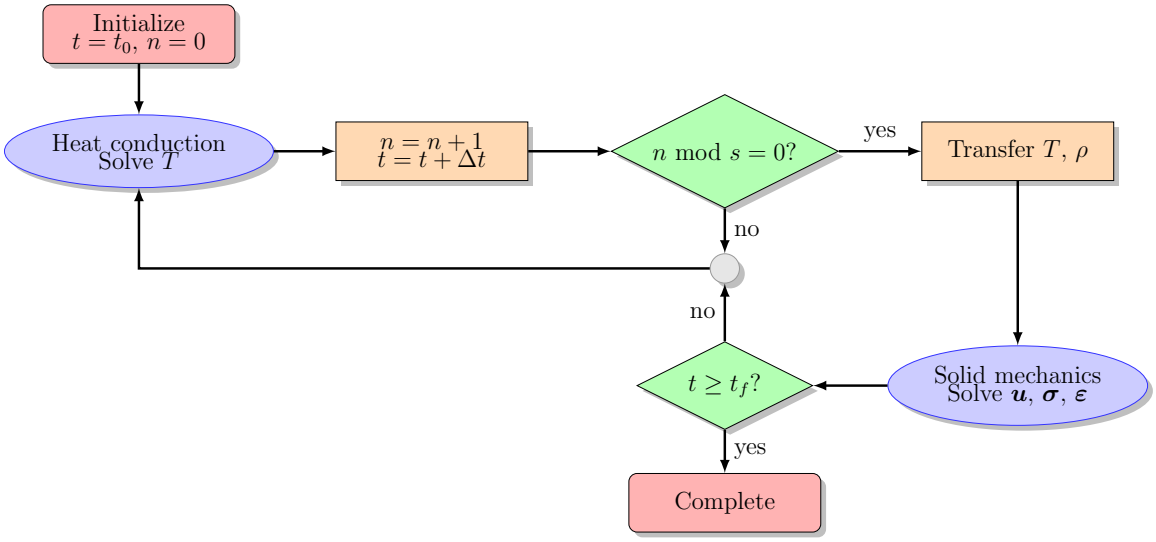

Figure 6.1: One-way coupling scheme for 1D finite difference method solver

It should be noted that all the information is uni-direction from heat conduction to solid mechanics. There is no feedback of the calculated displacement to thermal response. Most commercial software are using this scheme for thermo-mechanical coupling problem such as ANSYS [34] and Comsol [90].

Verification case

Consider a bar made of steel with properties given in Table 3.1. The left end of the bar is subjected to a constant heat flux $Q_w = 75{,}000$ W/m^2 while the right end is set to an iso-thermal boundary. For the structural boundary conditions, both ends are

fixed support, while others are constraint in y, z planes. Initially, the bar is at rest, and at a temperature of $T = 298$ K.

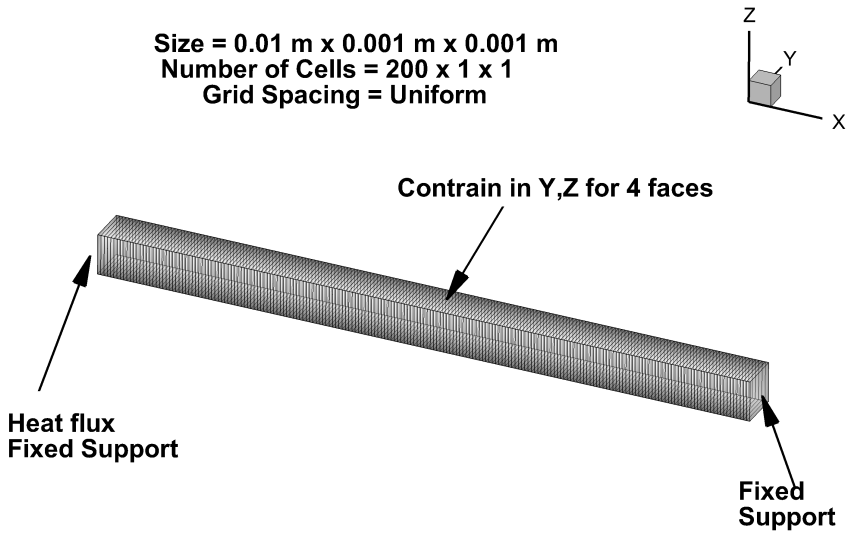

Figure 6.2: Boundary conditions and computation grid for verification case

Temperature profiles for the first 5 seconds are presented in Fig 6.3. It can be observed that as time elapses, temperature gradually increases from left to right. The solution is compared to the ANSYS result, with an excellent agreement.

The results for displacement profile are provided in Fig 6.4. It can be seen that the overall displacement is zero because of the two fixed ends. The compression and extension, however, can be observed during the heating process. Still, the results have very good agreement with ANSYS results. This phenomena will be discussed thoroughly in the next chapter.

6.5 Two-way quasi-static solution

The developed 1D code presented here serves as a verification tool for more complex solutions such as finite volume one, which will be introduced in next chapter. Unlike the one-way coupling presented in Chapter 3, the information transfer account

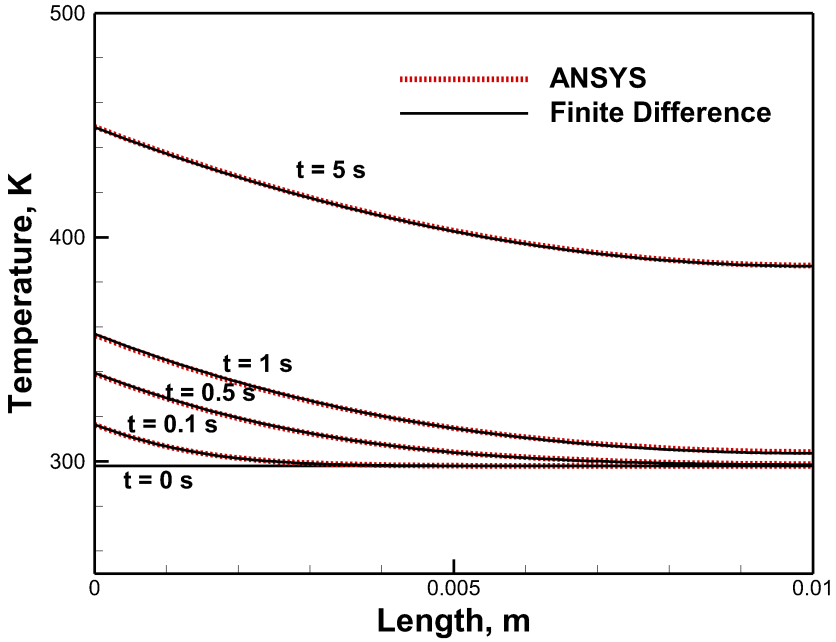

Figure 6.3: Temperature verification

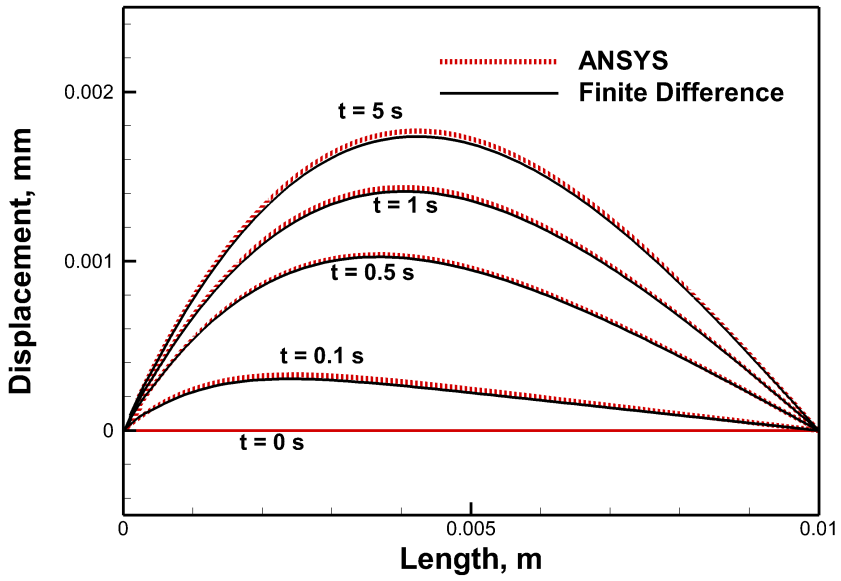

Figure 6.4: Displacement verification

for displacement. The displacement, in the form of geometry deformation, will be transferred back to the heat conduction solver and formed a closed information loop.

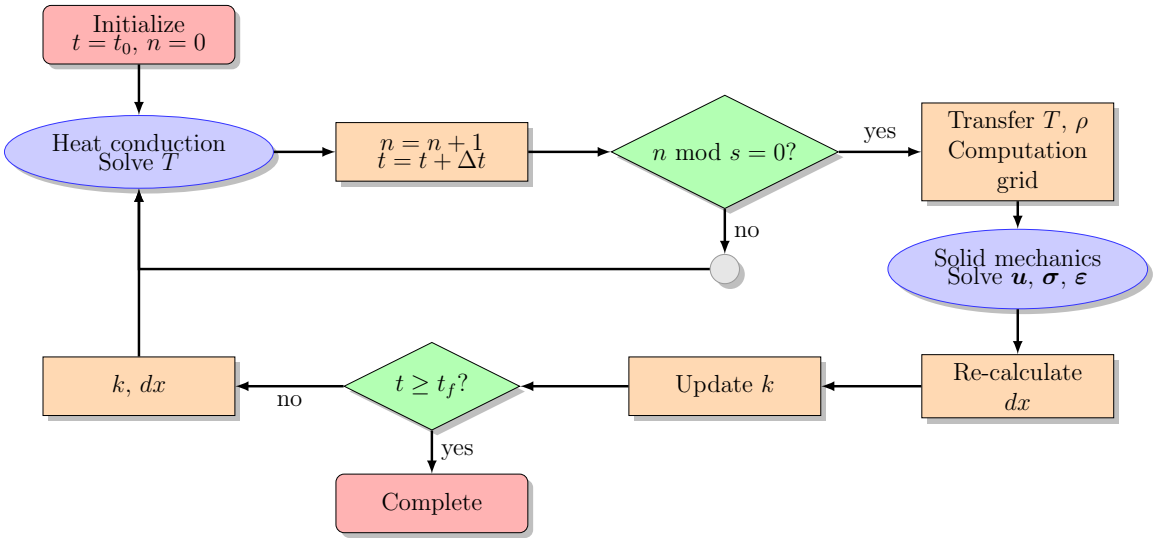

Figure 6.5: Two-way coupling scheme for 1D finite difference solver

Several steps are necessary to accomplish the feedback to the thermal response. The first one is to transfer the grid deformation since the amount of displacement has been obtained. This first step is simply to visualize the deforming grid, and no parameters are changed. The next step is to update the gradient of the primitive variables, in this case is the temperature gradient. In another word, the geometric parameters necessary for the calculation of gradient must be updated, like node position and area. Then, a mass conservation for each cell should be performed. By doing so, it ensures that no matter how the grid is changed, the total mass remains constant. As a result, density changes, even it could be very small. The local strain can then be calculated to examine the strain effects on the material properties.

The discussion above indicates the steps of developing such two-way coupling scheme, and the methodology can be applied to more complex coupling schemes such as fluid solid interaction (FSI), which will be discussed later.

Thermal expansion

Generally speaking, thermal expansion may occur when an object is subjected to heating, with certain constraints on its boundaries. Here, discussion will be given on the mechanism of this expansion and followed by a definition of strain effects.

Consider an object made up of a number of small cubic elements with equal sizes, just like the usual computational grid, and that maintains continuum under limited distortion. At this time, let the temperature of the object increases uniformly throughout the object. Under the assumption that there is no constraints on the boundaries, each element will expand with equal amount of volume in all directions. Therefore, all the cubic units are still the same sizes and fit together to form an expanded continuum body. In this example, no stress is induced and only strain is introduced.

If the object has an nonuniform temperature, each element expands differently, with an increase proportional to the temperature change. In this scenario, elements become different in sizes and can no longer fit together. To maintain continuum, each elements must restrain the deformations of its neighbor elements and stress is induced. In one-way coupling problem, this expansion in geometry is ignored due to the relative small values of displacement. In two-way coupling, however, the resulted deformation in geometry is taken into consideration.

Strain effects in material properties

Within the scope of this research, the discussions focus on the strain effect on conductivity. The capability of conducting energy within the material is based on the molecular dynamics, since it relies on vibration waves. When material expands, the distance between neighbor elements increases and resulted in a slower vibration wave, which results in a decrease in conductivity. Thus, the conductivity is no longer a constant but a variable depend on the volumetric strain e_v, which is $k = f(e_v)$. This

relationship can be described by a linear formula,

$$k(e_v) = \frac{k}{1 + ce_v} \tag{6.5}$$

where c is a relaxation coefficient to magnify or reduce the strain effects on the conductivity. Therefore, if $c = 0$, the strain has no effects on conductivity. In this study, different values of c are tested to evaluate the strain effects on both the temperature and displacement field. With this understanding, the coupling equation becomes,

$$\frac{\partial}{\partial x}\left(k(e_v)\frac{\partial T}{\partial x}\right) - \rho c_v \frac{\partial T}{\partial t} + Q = 0 \tag{6.6a}$$

$$(\lambda + 2\mu)\frac{\partial^2 u}{\partial x^2} - (3\lambda + 2\mu)\alpha\frac{\partial T}{\partial x} = 0 \tag{6.6b}$$

The first term of Eqs. 6.6a must be carefully treated. In the current 1D approach, this term is treated both analytically and numerically. Using the chain rule, it can be written as,

$$\frac{\partial}{\partial x}\left(k(e_v)\frac{\partial T}{\partial x}\right) = \frac{\partial k(e_v)}{\partial x}\frac{\partial T}{\partial x} + k(e_v)\frac{\partial^2 T}{\partial x^2} \tag{6.7}$$

This expanded formula can be evaluated using analytic form of both first order and second order derivative temperature with respect to coordinate x. However, the first order spatial derivative of conductivity is calculated by the solid mechanics module. Thus, there is no direct formula for this derivative. Therefore, numerical derivative is used to calculate this term as,

$$\frac{\partial k(e_v)_i}{\partial x_i} = \frac{k_{i+1} - k_{i-1}}{2\triangle x} \tag{6.8}$$

where k_i can be written as,

$$k(e_v)_i = \frac{k}{1 + ce_{vi}} \tag{6.9}$$

6.6 Verification results for two-way coupling

The verification case considers the same setup described in Section 6.4. The only difference is that strain effects on material property will be transferred back into the thermal response code to formed a closed two-way information.To simplify the problem, only the conductivity is transferred based on the linear relationship with volumetric strain discussed in Section 6.5.

Figure 6.6 presented results for $c = 10$. For each variable, results are plotted from $t = 0$ s to $t = 5$ s with a time step of $t = 0.1$ s. Figure 6.6a shows the temperature increases as time elapses. Figure 6.6b shows the displacement distribution, which increases and reaches a equilibrium state at $t = 5$ s with a maximum value of 0.0018 mm. Figure 6.6c plots the strain distribution along this bar, showing both compression and expansion. The positive value indicates the material expansions, which is located at the front part of the bar. The maximum strain is located at the front surface, where the highest temperature gradient is presented. At the end surface, where $x = 0.01$ m, strain has a negative value of approximately -0.05%, indicating that this part is compressed. Figure 6.6d shows the changes of conductivity. Because the linear relationship is used, the conductivity decreases as strain increases. Since the value of c is relatively small, as is the local strain, the change of conductivity is not significant, with the range of [59.8 - 60.8].

Figure 6.7 shows the result when $c = 1,000$. In this case, the strain effects is magnified. In Fig. 6.7a, at the final state when $t = 5$ s, maximum temperature increases to about 463 K and the temperature gradient becomes sharper compare to the previous result. This is caused by the decreasing conductivity, which slows the energy transfer. In Fig. 6.7b, due to the steeper temperature field, the maximum displacement increases to about 0.0185 mm. The overall distribution follows the same pattern. In Fig. 6.7c, the value of resulted strain is changed by the strain effects itself. At the front surface, the value of strain increases to 0.128%. Compare to the case

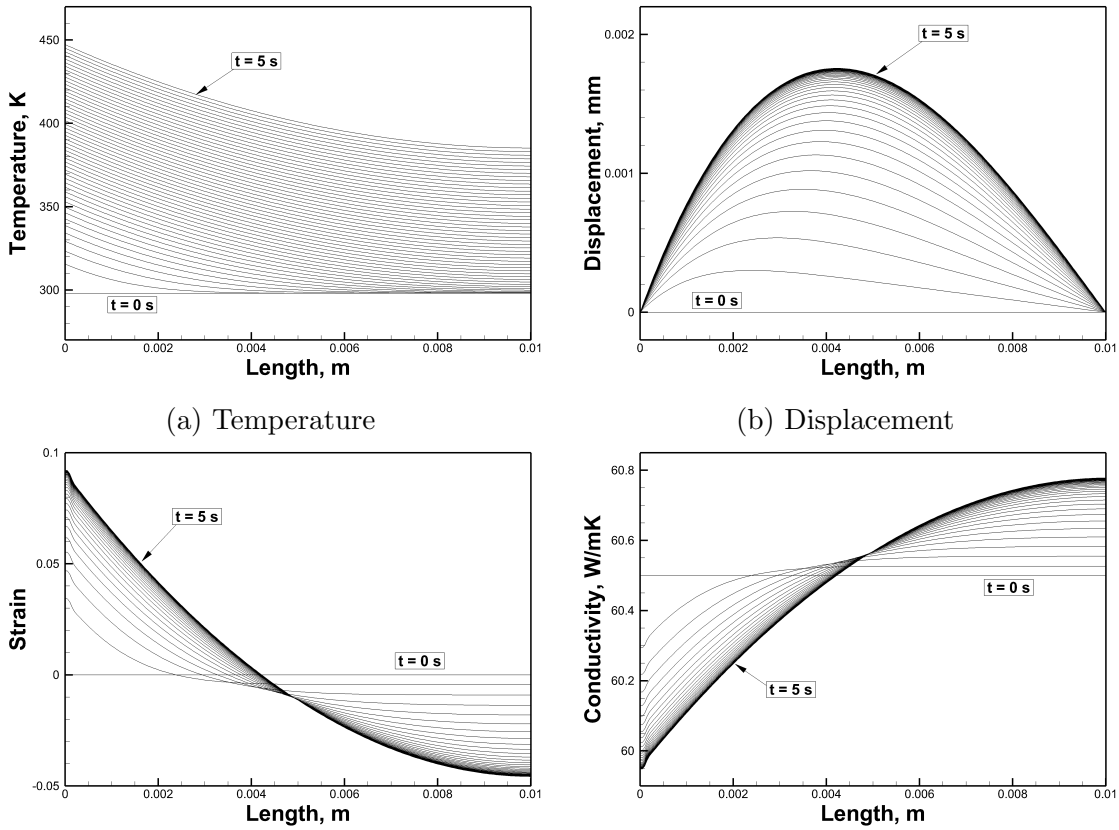

(a) Temperature

(b) Displacement

(c) Strain

(d) Conductivity

Figure 6.6: Results for $c = 10$ in time range $t = 0 - 5$ s

when $c = 10$, the maximum value of strain increases by 42%, indicating the expansion increases greatly. No significant change is observed at the end surface. In Fig. 6.7d, it can be seen that conductivity changes greatly because of the large c, with values in the range [34 - 105].

6.7 Summary

A 1D thermo-mechanical solver was developed for both one-way and two-way coupling schemes. Both schemes utilize a quasi-static framework for coupling the thermal module and solid mechanical module. The one-way results are verified against the commercial code ANSYS [34] and shows good agreement. No commercial code is found for direct two-way coupling because of the complex information loop.

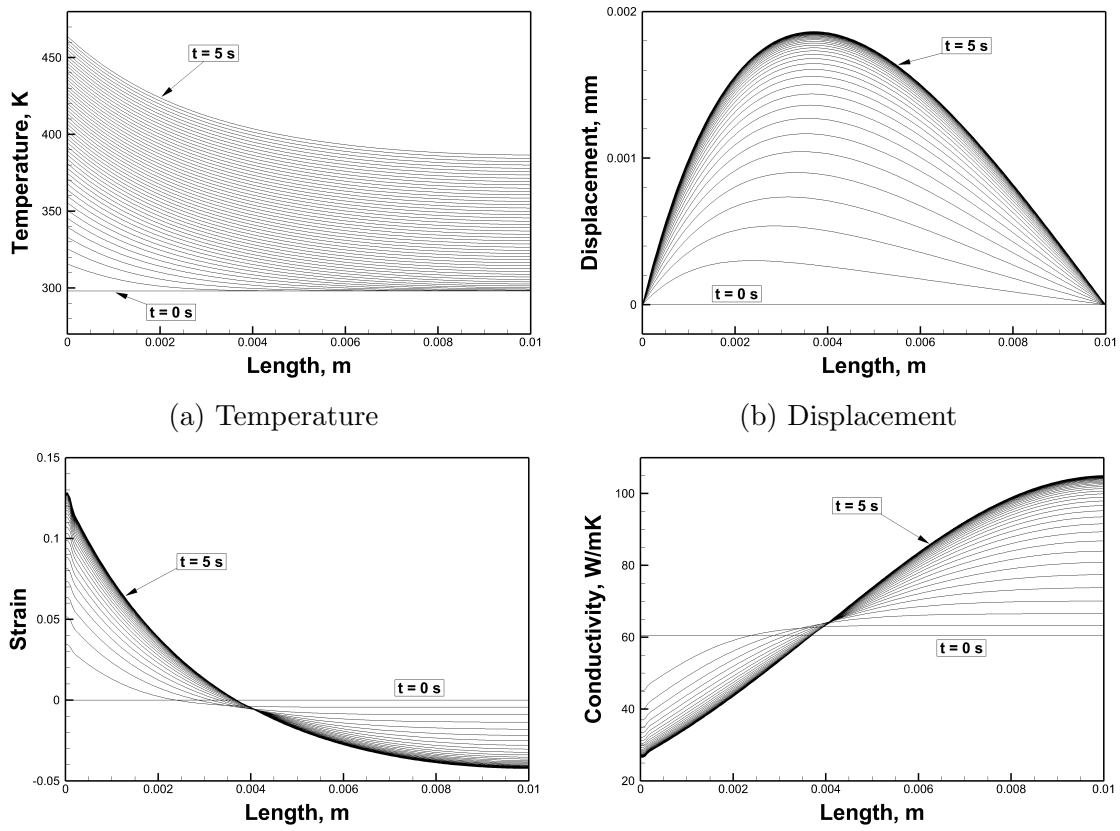

(a) Temperature

(b) Displacement

(c) Strain

(d) Conductivity

Figure 6.7: Results for $c = 1000$ in time range $t = 0 - 5$ s

The results in two-way coupling are important for applications where accurate description of thermal and structural performance are needed. One of the findings is that the strain effects not only change the structural performance such as displacement and strain, but also influence the thermal performance. It re-distributes the temperature and causes the material properties to change significantly. In the areas such as precision machining and re-entry problem, where the subtle changes cannot be ignored, two-way coupling should be the standard method for simulation.

Chapter 7: Thermo-mechanical Two-way Coupling

7.1 Introduction

During re-entry, large heat flux results in thermal expansion and stress. At the same time, this process is accompanied with shear force from the flow field and internal pressure produced by pyrolysis gas. Under such conditions, TPS materials tend to expand to a certain degree such that strain effects cannot be ignored. TPS materials usually have a coefficient of thermal expansion with an order of $10 \sim 100\times\ 10^{-6}$ m/m·K[38]. With a significant temperature gradient, which occurs on the TPS, local strain can be as large as 10 percent. Micro-scale strain can also alter the material properties such as permeability, porosity and conductivity. One of the direct effects of mechanical stresses is the phenomenon known as spallation[91, 49]. This phenomenon can be described as the ejection of material particles into the flow field. This process usually results from material failures and may lead to catastrophic loss. The cause of spallation is not well understood and is currently modeled by multiplying an empirical parameter to the thermochemical ablation rate[53]. A possible cause of spallation is the material failure resulting from exceeding the strength limit. If variability of material properties has been considered, thermal strain may cause the local defect and it is directly related to the spallation. TPS are usually manufactured using a carbon fiber matrix[54, 55, 4]. For most of materials, their integrity is maintained when the mechanical stress is less than a certain threshold value (for instance, 500 MPa for crossply carbon-fiber composite[56]). Once this stress limit has been exceeded, fractures appear on the fiber scale, leading to material failure. Numerous studies have been published on the mechanical behavior of porous ablators. One such study [57, 58]

focuses on the fracture testing of virgin and charred PICA. It was observed that cracks were initiated and grew when a critical stress limit has been reached, separating the carbon fibers from the binder. Therefore, to correctly predict failure of the TPS, it is essential to accurately model both the distributions and magnitudes of stresses within materials.

Stress field within the TPS material is not only related to high temperature gradient. The complexity of this problem increases as chemical reactions and surface blowing are considered [59]. These two factors are entwined with the ablation process, resulting in density changes and production of pyrolysis gas [92]. Transformation of TPS material by chemical reaction results in radical changes properties such as ultimate strength, coefficient of thermal expansion. Transportation of pyrolysis gas not only changes temperature field, but also leads to internal pressure which can cause stress concentration. Due to the complexity of coupled physical interactions, detailed numerical modeling is still in its first stage [93]. Solid mechanical solvers are usually only coupled with heat conduction, and material changes and internal pressure within the material are not taken into account.

The one-way coupling features a uni-direction information transfer from one physical solution to the other as input parameters. More specifically, it features transferring temperature profiles from material response code to structural response code. Within a quasi-static scheme, the heat transfer has a continuous solution, and the structural response is assumed to be static and converged for each time step. In such a way, thermal strain, thermal stress and expansion can be calculated within the material for different temperature gradient. Consequently, it assumes that changes of geometry are so small that its effects on the computational grid can be neglected. The manufacturing industry, especially material machining and welding, uses this kind of approach to solve problems. Another type of one-way thermo-mechanical coupling focuses on strain energy and its effects on the temperature field. This type of ap-

proach, for instance, is used to study to the thermo-mechanical analysis of automobile braking system[94].

Unlike the one-way scheme, two-way coupling can provide more accurate predictions. In this coupling scheme, temperature solutions are firstly transferred to the mechanical code, and produce in displacement and geometry deformation. This changes of shape are then transferred back to thermal analysis to complete a bi-direction information transfer loop. As a result, higher fidelity solutions are obtained for both solvers. Changes in the shape also lead to variations in the heat flux within the material, which result in more accurate solution. Considering the strong thermal gradient present in hypersonic thermal response, it is clear that there is a need to explore the necessity of using a two-way coupling approach for the ablation problem.

In order to facilitate the coupling between the two code, a finite volume method can be used. This methodology has been used in solid mechanics analysis multiple times, mainly because of the ease of implementation. Bijelonja and Demirdzic[77] proposed such an approach for the linear elasticity problem. The same approach was also used for a coupled thermo-mechanical stress analysis, on a moving mesh.[78]. To validate the approach, Fallah et al.[79] offered comparisons of Finite Element Method (FEM) and Finite Volume Method (FVM) results for different geometries and stress analysis. All of these studies demonstrated that FVM has equal accuracy while being simpler to implement mathematically and numerically. In addition, by using FVM, the same shared computation grid can be used for both material and structural codes. For dissimilar mesh in thermo-mechanical coupling, the mapping between different mesh can be problematic, resulting in decreased accuracy and computational efficiency.

The present study proposes a unified FVM for coupling multi-physics models for ablation simulations. A finite volume approach has been used for both thermal and structural responses. A quasi-static two-way strong coupling strategy has been

utilized for coupling both codes. In the following sections, the numerical framework and formula necessary to generate results are presented. Verification cases will then be provided along with ANSYS results. Then, study cases on ablation problem and internal pressure field and how it acts on the material are provided. Finally, a fully coupled case is presented to show the combination effects of internal pressure and thermal expansion within the iso-Q sample.

7.2 Governing equations and numerical implementation

7.2.1 Numerical framework

The solid mechanics and material response codes have both been developed within the Kentucky Aerothermodynamic and Thermal-response System (KATS) framework [70, 71]. KATS has been used to solve hypersonic flows [82], low-speed turbulent flows [83, 84], and material response [71, 70]. KATS is designed for massively parallellized computations, utilizing ParMETIS [85] for domain decomposition and openMPI [86] as the message passing interface. In KATS, the general time-independent partial differential equations are written in the following form

$$\nabla \cdot (\boldsymbol{\mathcal{F}} - \boldsymbol{\mathcal{F}}_d) = \boldsymbol{S}\,, \tag{7.1}$$

where $\boldsymbol{\mathcal{F}}$ the advective fluxes, $\boldsymbol{\mathcal{F}}_d$ the diffusive fluxes, and $\boldsymbol{S}$ represents the source terms. The system of equations is integrated over a cell volume, and spatially discretized. The resulting linear system is solved iteratively for the whole domain, using an implicit backward Euler scheme

$$\left[-\frac{\partial \boldsymbol{R}}{\partial \boldsymbol{Q}}\right] \Delta \boldsymbol{Q} = \boldsymbol{R}\,, \tag{7.2}$$

where $\boldsymbol{Q}$ represents the conservative variables and V is the volume of the cell. Vector $\boldsymbol{R}$ represents the right hand side terms of the linear system and is defined as

$$\boldsymbol{R} \equiv -\sum_{i \in \text{cell}} (\boldsymbol{\mathcal{F}} - \boldsymbol{\mathcal{F}}_d) \cdot \boldsymbol{n}_i A_i + \boldsymbol{S} V \tag{7.3}$$

where A_i and $\boldsymbol{n}_i$ are respectively the area and normal vector of the i^{th} face of the cell.

7.2.2 Governing equations for the structural response module

The structural response module in KATS solves for the displacement field $\boldsymbol{u} \equiv (u_x, u_y, u_z)$. Three relations – force equilibrium, strain tensor and Hooke's Law – compose a closed system for the evaluation of the structural response, and are given as

$$-\nabla \cdot \boldsymbol{\sigma} = \rho_s \boldsymbol{f}, \tag{7.4}$$

$$\boldsymbol{\sigma} = 2\mu\boldsymbol{\varepsilon} + \lambda \ \mathrm{Tr}(\boldsymbol{\varepsilon})\boldsymbol{\mathcal{I}}, \tag{7.5}$$

$$\boldsymbol{\varepsilon} = \frac{1}{2}[\nabla \boldsymbol{u} + (\nabla \boldsymbol{u})^{\mathrm{T}}]. \tag{7.6}$$

where ρ_s represents the density of a solid material, $\boldsymbol{\sigma}$ is the stress tensor, t is time, $\mathbf{f}$ is the external body force per unit mass and $\boldsymbol{\varepsilon}$ is the strain tensor. μ and λ are respectively the first and second Lamé parameters, and are obtained with

$$\mu = \frac{E}{2(1+\nu)} \tag{7.7}$$

$$\lambda = \frac{E\nu}{(1+\nu)(1-2\nu)} \tag{7.8}$$

where E is Young's modulus and ν is Poisson's ratio. Since the components of the displacement vectors $\boldsymbol{u}$ are the variables for which the equation is solved, the conservation equation can be rewritten as

$$-\oint_{\partial V} \left[\mu \left(\nabla \boldsymbol{u} + (\nabla \boldsymbol{u})^{\mathrm{T}}\right) + \lambda \ \mathrm{Tr}(\nabla \boldsymbol{u})\boldsymbol{\mathcal{I}}\right] \cdot \mathbf{n} \, da = \int_V \rho_s \boldsymbol{f} \, dV \, . \tag{7.9}$$

Initial conditions are set using the distribution of displacement $\boldsymbol{u}$ or $\partial \boldsymbol{u}/\partial t$ at $t = 0$. The solution is obtained by applying the usual boundary conditions such as a fixed support on the surface, symmetry, fixed pressure, fixed traction or free surface (zero traction).

7.2.3 Coupling scheme

The scheme used for coupling the material response and structural response codes is described here. Even though the material response code offers transient solution, it assumed that the structural response reaches equilibrium much faster and thus can be considered time-independent. Figure 7.1 presents the coupling scheme, detailing how information flows between the material and structural response codes. During the simulation, the material response code provides temperature, solid density and pressure to the structural response code while the structural code provides information on deformation of computational domain, local strain and its effects on the material properties for certain amount of time steps.

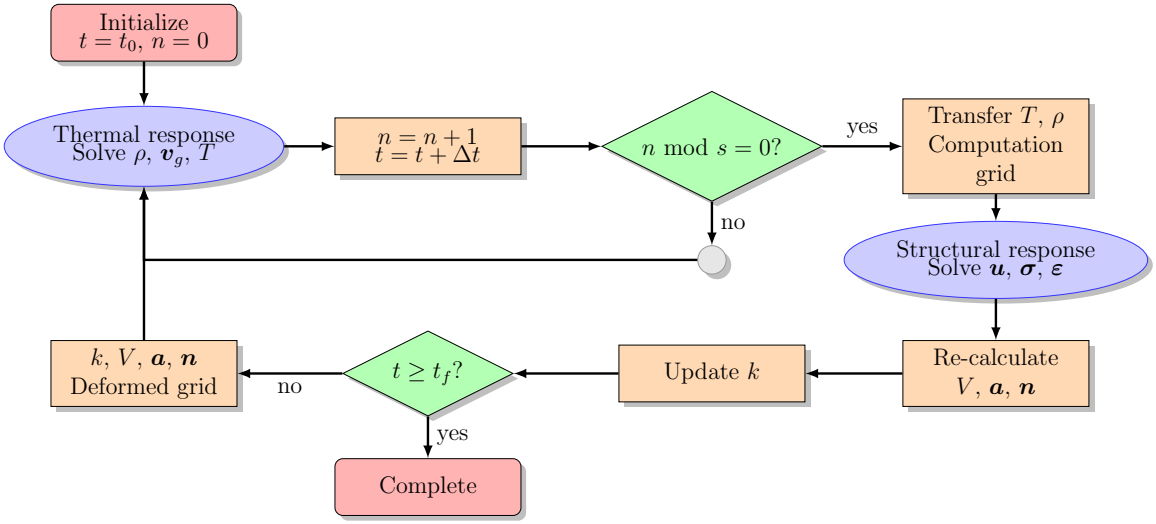

Figure 7.1: Two-way coupling scheme between the structural response and thermal response

The two-way coupling is achieved by exchanging quantities between the codes which influence each respective model. Since the displacement field affects the shape of the domain, the computational grid needs to be modified accordingly. This results in additional updates on the face weights, node positions and cell volumes. It is important to point out that these changes must be performed under the constraints of mass conservation. Therefore, the density of the material is directly affected by

the displacement. Moreover, strain also has an effect on material properties such as conductivity and porosity. These quantities also need to vary. Finally, since the structural solver assumes steady-state, solutions must be updated regularly, insuring that the temperature changes on the structural aspect remains reasonable. These interactions are achieved in a way that balances the coupling frequency to the computational efficiency.

7.2.4 Strain definition

Strain is defined as a relative displacement of particles in the body that excludes rigid-body motions. For a typical engineering normal strain, it is defined as:

$$e = \frac{\Delta L}{L} = \frac{l - L}{L} \tag{7.10}$$

where e is the engineering normal strain, L is the original length and l is the deformed length of the object. In a FVM framework, the definition of strain has been extended to volumetric strain as it is easier to represent the local strain. The volumetric strain is defined as:

$$e_v = \frac{\Delta V}{V} = \frac{V' - V}{V} \tag{7.11}$$

where e_v is the volumetric strain, V is the original volume of an object and V' is the deformed volume of the object. For 1D problem, both of engineering strain and volumetric strain will have the same value. Under the assumption that material is isotropic, the volumetric strain is used in all following studies.

7.2.5 Strain effects on porous media properties

Strain effects have significant impacts on various properties of porous media. Discussion of detailed property models for porous material is beyond the scope of this study. Therefore, the strain relationship used to describe the key parameters will come from related researches. An example of the variation of the porosity as a function of strain

can be found from Bakhshian and Sahimi [64]. In their studies, the porosity varies almost linearly with the strain.

Inspired by this study, the strain-conductivity relations are developed. When material expands, the distance between molecules increases. According to the molecule dynamics, it becomes harder for the heat wave to vibrate through the material. Therefore, the conductivity will decrease when material is undergoing thermal expansion. For the purpose of verification, a simple linear relation between strain and conductivity has been built as:

$$k' = \frac{k}{1 + c\, e_v} \tag{7.12}$$

where k' is conductivity after deformation, k is the original conductivity, c is a relaxation coefficient to magnify or reduce the strain effects on the property and e_v is volumetric strain. In this study, different values of c are tested to assess the strain effects on the temperature field.

7.3 Verification test cases

In this section, verification cases are presented to show the correct implementation of governing equations. Due to the lackage of commercial code capable of two-way coupling, a 1D code is developed using Finite Difference Method. Thus, in the verification process, this 1D code along with KATS will be verified against ANSYS [34] for one-way results. And then, two-way results will be compared using 1D code and KATS to show the same results are obtained.

The material used is steel and its properties are presented in Table 7.1. To simplify the problem, all the properties are considered independent of temperature and the strain effects will only impact on the conductivity.

Additional verification test cases for the developed structural response code can be found in [95]. In the present document, only thermo-mechanical coupling is presented.

Table 7.1: Thermal and mechanical properties for steel

Density, kg/m^3	Specific heat, J/(kg·K)	Conductivity, W/(m· K)
7850	434	60.5
CTE, μm/(m·K)	Young's modulus, GN/m^2	Poisson's ratio
12	200	0.3

7.3.1 Geometry and boundary conditions

The same geometry and boundary conditions are used for both one-way and two-way coupling. Consider a steel bar is heated at a constant heat flux for 5 seconds in Fig. 7.2. The thermal boundary conditions at $x = 0$ is $Q_w = 7.5 \times 10^5$ W/m^2, and all other surfaces are perfectly insulated. The reference temperature is set to 298 K to represent the indoor environment. For structural boundary conditions, both of two ends are fixed, and all other surfaces are constrained in specific directions.

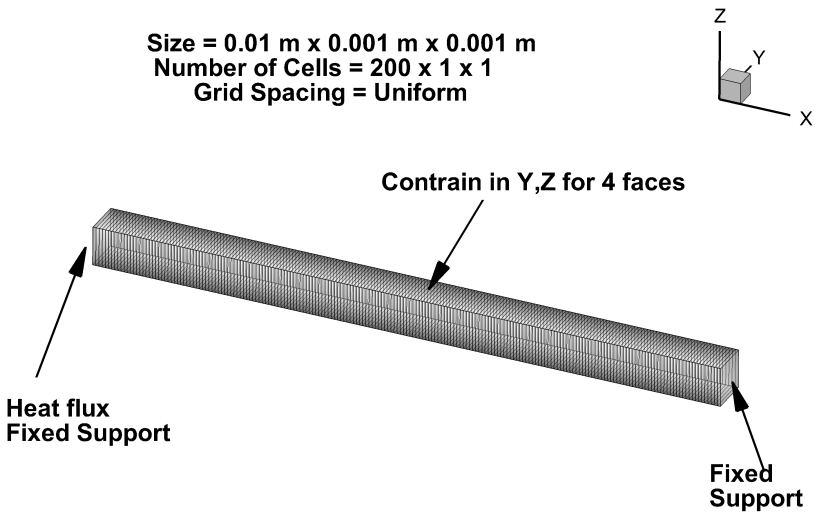

Figure 7.2: Verification case with boundary conditions and computation grid

7.3.2 One-way coupling results verification

Figure 7.3 shows the temperature comparisons for three different codes. At $t = 0$ s, the temperature is uniform at 298 K. As left side is subjected to the heat flux, the

temperature increases from left to right. The perfect agreement for each code can also be observed. L-2 norm will be added very soon.

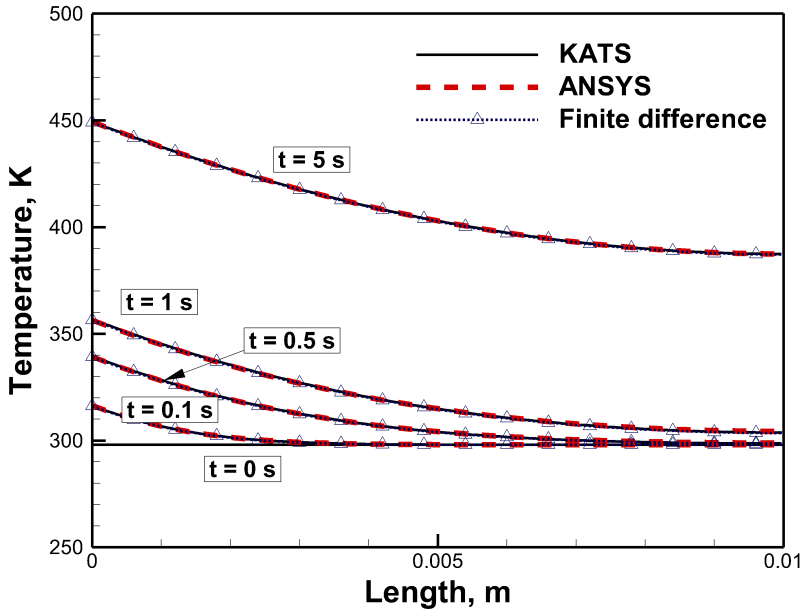

Figure 7.3: Temperature results comparison

Figure 7.4 presents the results of displacement comparison. It can be seen that since the two ends are fixed, there is no overall deformation along the bar. However, displacement field shows that each element is expanding to its right (positive value of displacement) since thermal strain has a larger effect on the left part. Again, three different code produces results agree with each other perfectly.

Figure 7.5 shows the strain result comparison. For this result, ANSYS result is missing because it does not provide this volumetric strain value as direct output. The sign of the strain values represents the material either being compressed (negative) or expanded (positive). As seen by the strain distribution, expansion and compression occur at the same time. The left part of the bar is expanded due to the higher temperature gradient whereas the right part of the bar is compressed because of a lower temperature and increased thermal stresses.

It is interesting to point out that as the temperature magnitude increases with

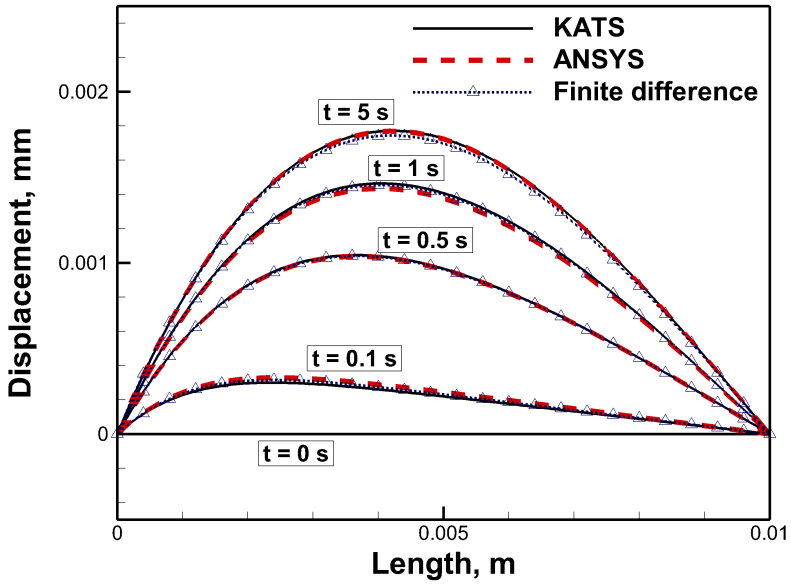

Figure 7.4: Displacement results comparison

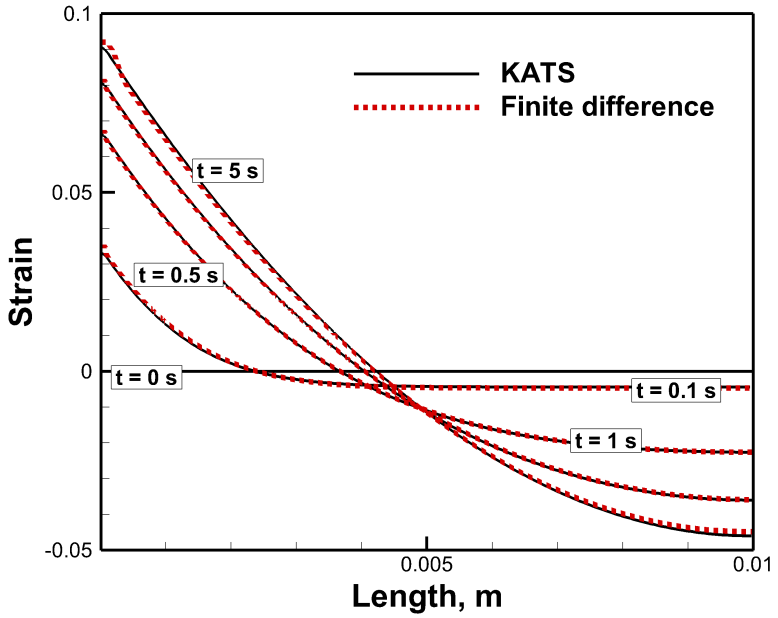

Figure 7.5: Strain results comparison

time, the displacement field reaches a steady state equilibrium. In Fig. 7.6a, the solutions are plotted by a time step 0.1 s. It is observed that the displacement field reaches its steady state with a maximum value at about $x = 0.0045$ m. Thus, the

strain alongside the bar behaves in a similar manner showed in Fig. 7.6b. The main reason is that the temperature gradient along the bar reaches a steady state as heat flux keeps heating the bar. Thus a constant temperature difference can be found.

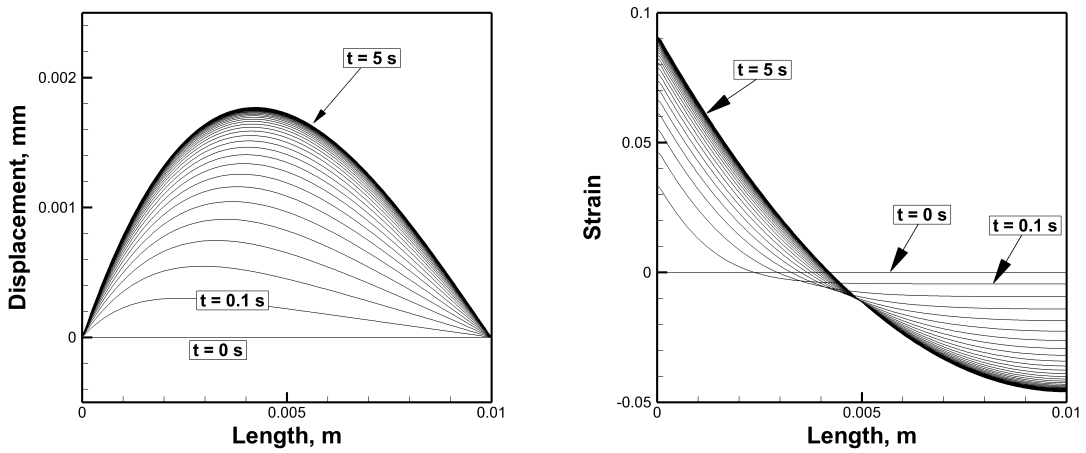

(a) Displacement (b) Strain

Figure 7.6: Results for different times

7.3.3 Two-way coupling results verification

Since ANSYS does not provide direct way for two-way thermo-mechanical coupling, the comparison of results in this section will between KATS and developed 1D finite difference code. It should be noted that because different mathematical framework of these two solver, the results are able to be cross-validated to show the correct implementation of governing equations.

With the understanding of the behavior of displacement and strain field, different values of relaxation coefficient have been chosen to evaluate the impacts on different variables. In order to increase the clarity, all the results shown are at $t = 5$ s when equilibrium reached with maximum and minimum values. In Fig. 7.7a, it can be observed that as strain effects become stronger, the temperature distribution becomes steeper. When compare $c = 1$ and $c = 1,000$, the temperature at the $x = 0$ m is higher for $c = 1,000$. It is because the conductivity decreases at $x = [0, 0.004]$ m,

thus, it becomes harder to transfer heat alongside the bar. For the rest of the bar, since conductivity increases, the temperature becomes smoother than when using $c = 1$. Changes in temperature also have impacts on the displacement field. In Fig. 7.7b, it can be observed that as the strain effects becomes stronger, the maximum displacement increases and the location of the maximum moves to the left, where temperature gradient is steeper.

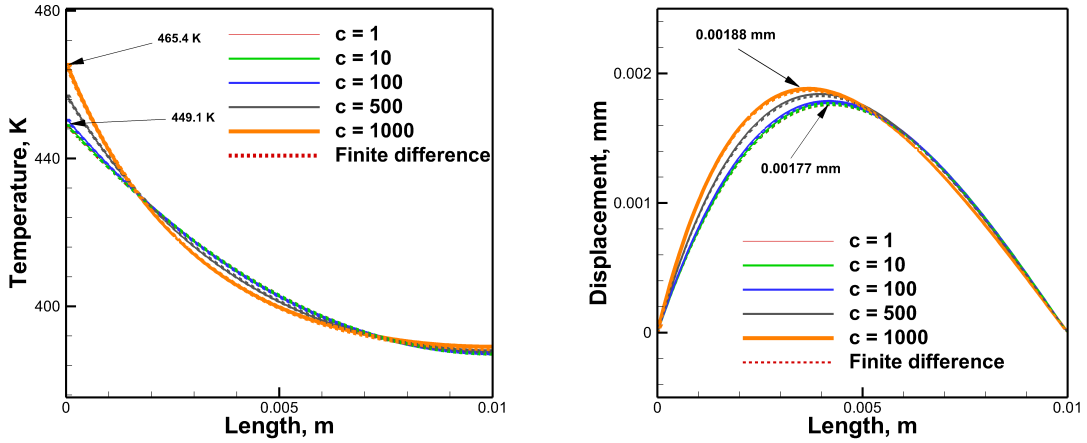

(a) Temperature (b) Displacement

Figure 7.7: Temperature and displacement results for various relaxation values at $t = 5$ s

The corresponding strain results are presented in Fig 7.8. The changes in strain follows the same behavior as the temperature. It should also be noted that because of the particular behavior of this case, the results of different variables are not proportionally related to the relaxation coefficient.

7.4 Two-way strong thermo-mechanical ablation 1D modeling

In this section, the fully coupling scheme is employed to model charring ablation problems. A step-by-step comparison is performed to show how the grid deforms, and how strain effect impacts the material response. First, 1D results are presented to better understand the physics and demonstrate how grid deformation and strain

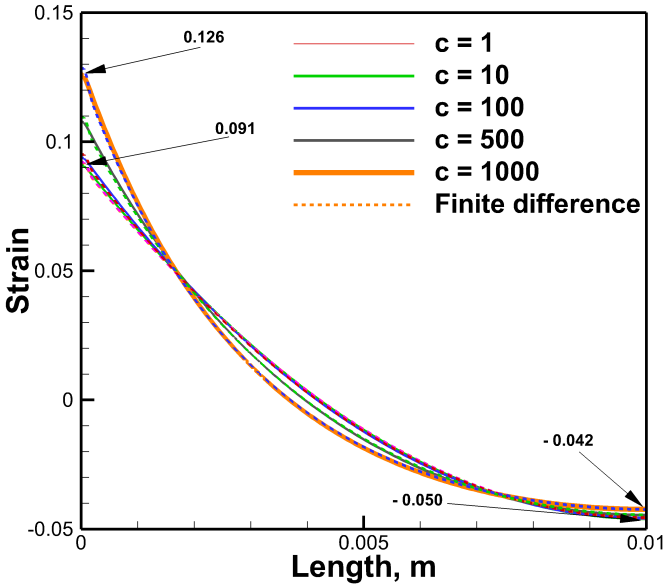

Figure 7.8: Strain results for various relaxation values at $t = 5$ s

effects play a role in strong coupling. Then, full 3D geometry – an iso-Q sample – is presented to show how geometric effects plays in coupled ablation problems. Contrary to the previous verification cases, the material used in the following sections is theoretical charring ablator TACOT [88].

7.4.1 Boundary conditions and coupling process

The geometry used for this problem consists of a 0.01 m 1D bar made of TACOT, as illustrated in Fig. 7.9. The front surface ($x = 0$ m) is subjected to a constant heat flux of $Q_w = 7.5 \times 10^5$ W/m^2, and a constant pressure at $p = 101,325$ Pa. The back wall ($x = 0.01$ m) is assumed to be adiabatic and impermeable with a fixed support. All other surfaces are considered to be symmetric.

7.4.2 Results

For this case study, the relaxation factor c is set to 1. The temperature values for different coupling schemes are presented in Fig. 7.10. The four lines represent

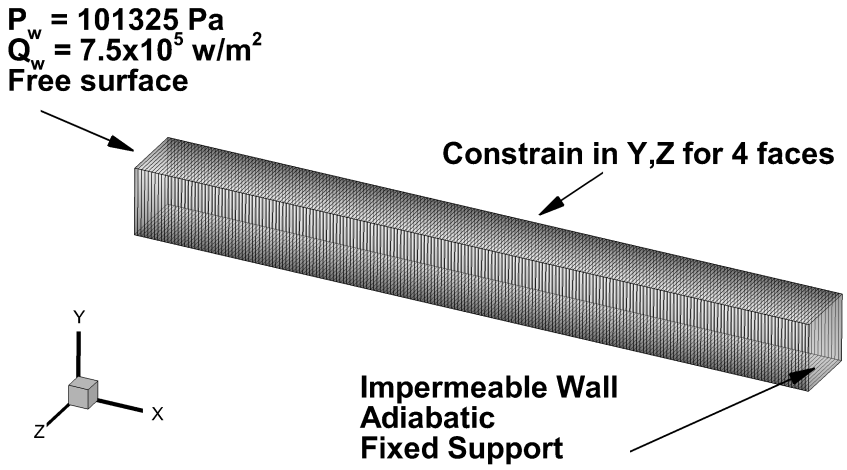

Figure 7.9: Charring ablation case with boundary conditions and computation grid

the results obtained with simple one-way coupling, grid deformation feedback, strain effects on conductivity and full coupling, respectively. Using the one-way coupling as the baseline, it can be seen that the thermal expansion at the front surface is captured by the grid deformation coupling. Because of this displacement, the results are shifted to the right, and very small temperature changes are observed. When the strain effects are added, the maximum temperature increases for about 10 K, due to the decrease in the conductivity in the expanded region. Since conductivity along the bar both increases and decreases, the temperature field becomes steeper at first and then becomes smoother. When both the grid deformation and strain effect are combined – the fully coupling results – the surface expands to the left with a temperature increase for about 7 K. Of course, since the relaxation factor is very small, the temperature increase is not significant. With a more accurate strain-property relation, more temperature changes are expected for this fully coupling case.

The results for displacement are presented in Fig. 7.11. When comparing the baseline one-way coupling to the rest, it can be seen that both grid deformation and strain effects play a role in decreasing the maximum displacement. The changes in

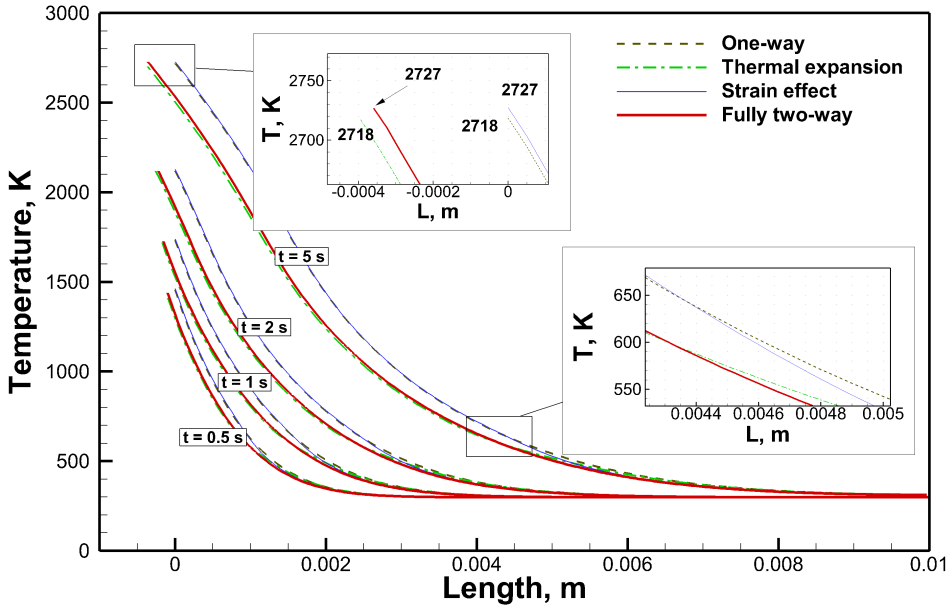

Figure 7.10: Temperature results for different coupling schemes

length decreases the whole displacement along the bar uniformly. However, the strain effects coupling smooths the displacement gradient around $x = 0.004$ m. As expected, the fully coupled results show these two combined effects: the displacement becomes smoother and with a smaller maximum value.

Figure 7.12 shows the distribution of von Mises stress along the bar. Compare to the one-way result as baseline, the magnitude of maximum stress does not change significantly. The location of the peak stress, however, are shifted to left. The thermal expansion is first observed to shift to left about 0.0001 m as well as the strain effect. As a result, the fully coupled result shows the peak moves to left about 0.0003 m.

Results for the volumetric strain are provided in Fig. 7.13. Although the total strain is about only 4%, the local volumetric strain can be quite large, with value as large as 17%. This large changes can have serious impact on solid density and related properties. The peaks of the lines illustrate where largest stress occurs, which is in the region between the virgin and char state (stress follows the strain behavior). Comparing the results at $t = 5$ s, grid deformation has little effects on the strain

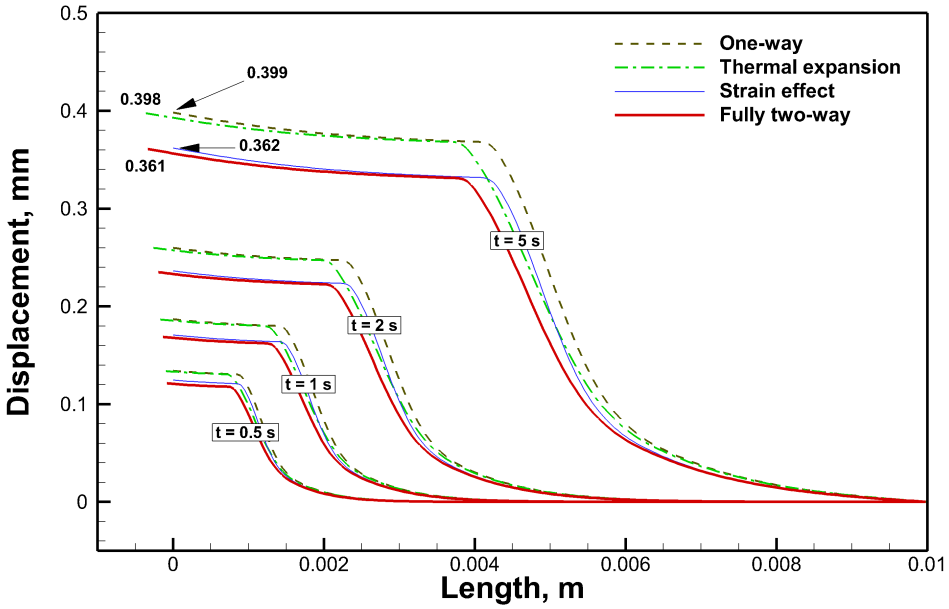

Figure 7.11: Displacement results for different coupling schemes

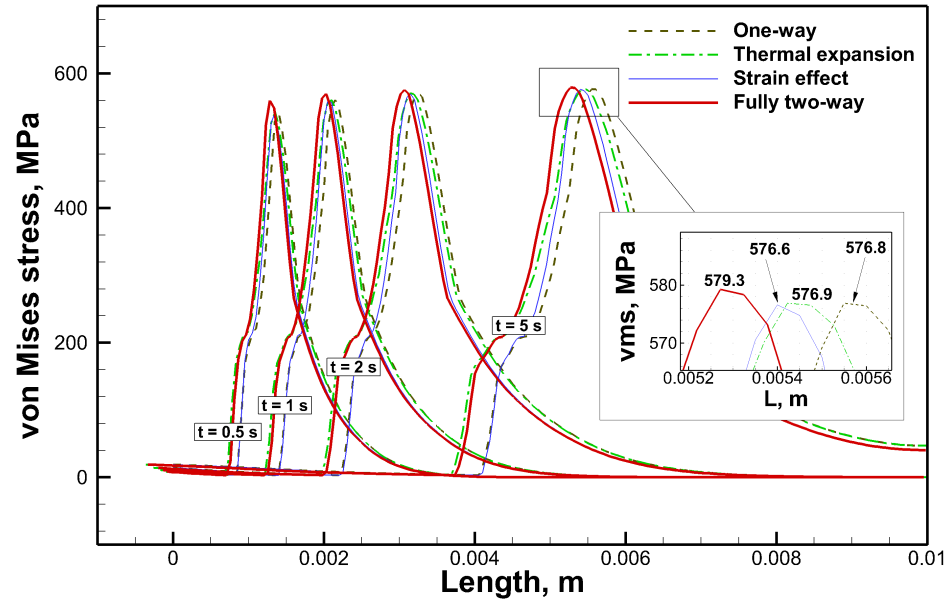

Figure 7.12: Von Mises stress results for different coupling schemes

magnitude. Strain on the contrary, decreases the peak value, although very minimally (about 0.1%). The combination of both phenomenon for the fully coupled case shows only a movement of the peak with little changes in magnitude.

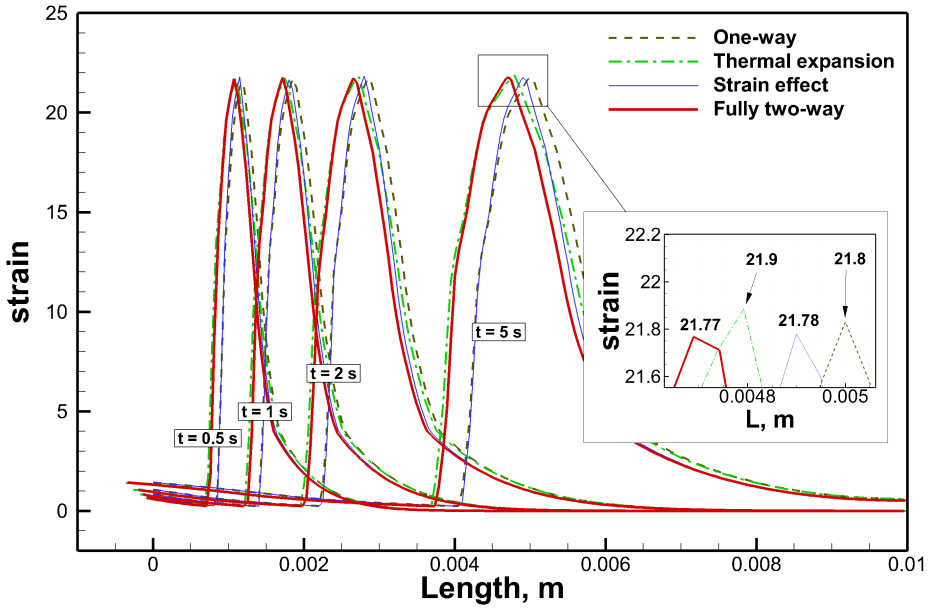

Figure 7.13: Volumetric strain results for different coupling schemes

7.4.3 Results on projected grid

To compare the importance of the two-way coupling scheme, the 1-way coupled results are projected on a new grid using the computed displacement solution. Figure 7.14 shows the temperature results, where the one-way and thermal expansion coupling schemes are both overlapping. The same observation is made for the strain effects and the two-way coupling temperatures. When compared to Fig. 7.10, it can be concluded that the strain effect has much stronger influences on the temperature distribution. This is not unexpected since the strain has a direct relationship with conductivity.

The same comparison is performed for the displacement, with the results shown in Fig. 7.15. The strain effect has a lower maximum displacement than the one obtained with the one-way coupling and moving mesh. As for the fully coupled results, the maximum displacement is even lower. When compared to the one-way coupling results, the maximum displacement is decreased by approximately 10%. As with the temperature, the strain effects considerably affect the displacement distribution.

Figure 7.16 illustrates the same comparison, but this time, with the von Mises

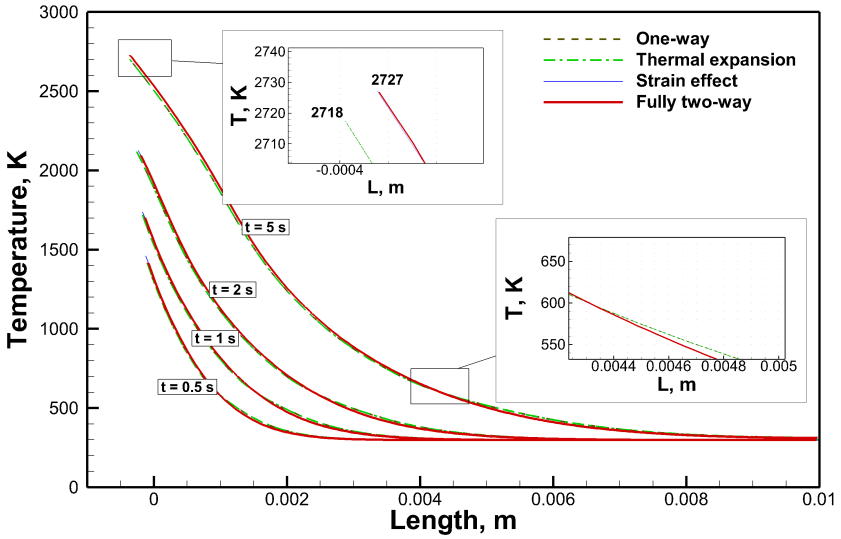

Figure 7.14: Temperature results on projected grid

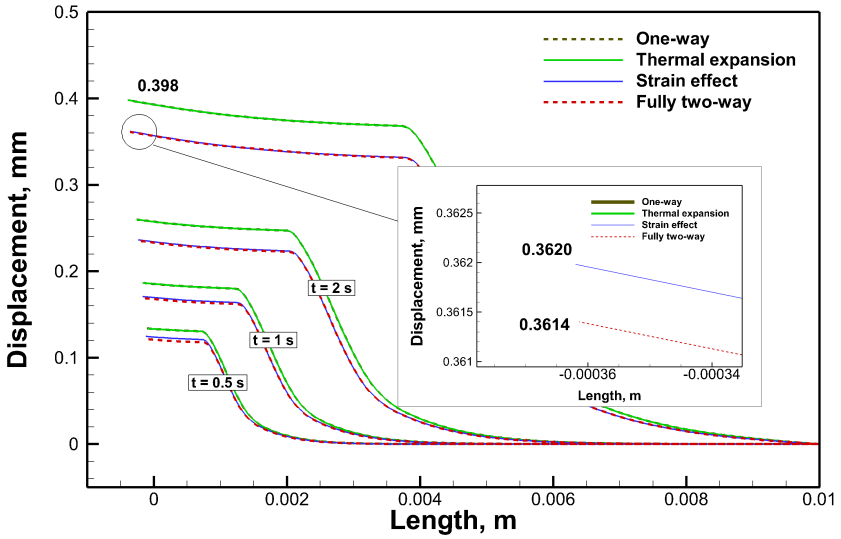

Figure 7.15: Displacement results on projected grid

stress. The strain effect shifts the peaks of the stress to left, even on the results obtained on a fixed mesh. When compared to the one-way results, the maximum stress obtained using the two-way coupling scheme increases to about 2.4 MPa.

Finally, Fig. 7.17 illustrates the results of the volumetric strain on the projected grid. It can be seen that the magnitudes of all the coupling schemes remains approximately constant, while the location of the maximum strain shifts to left in the case

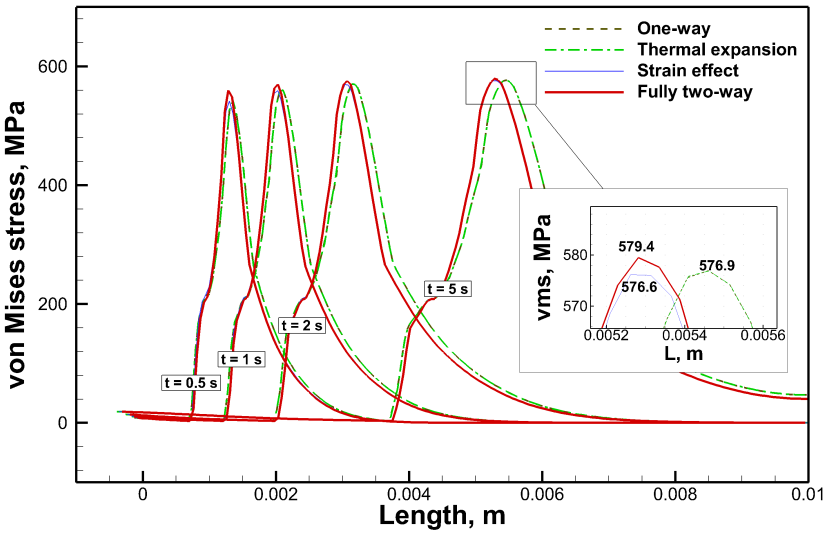

Figure 7.16: Von Mises stress results on projected grid

of the results obtained with strain effect and two-way coupling.

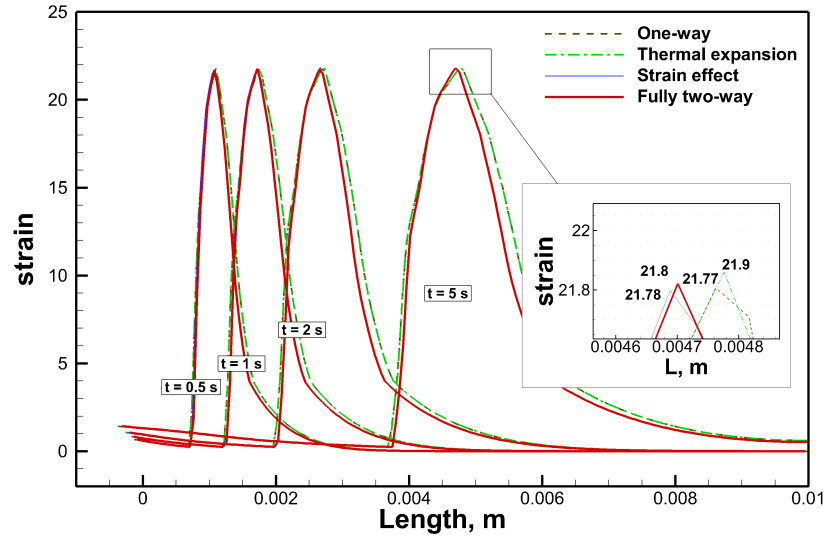

Figure 7.17: Volumetric strain results on projected grid

First, it is important to point out that the strain effect used for these results is set to be very small, with a relaxation parameter is 1. For a material more sensitive to volumetric strain, much stronger changes are expected. Second, the strain effect has a strong influence on the locations of the peak values of stress and strain, as well

as the maximum displacement and temperature. Therefore, it is undesirable to use a material that has strong strain related properties as TPS material.

7.5 Fully coupled iso-Q sample

Arc-jet facilities are used to produce an extreme environment suitable for TPS material testing. For this kind of tests, samples are usually shaped into an iso-Q sample so that the heat flux on the front surface is almost uniform. Fig. 7.18a shows a typical post-test iso-Q geometry and Fig. 7.18b shows the sample is being subjected to energized hypersonic flow. For this coupling case, a typical arc-jet material response is modeled in order to provide insightful results and a better understanding of the multi-physic process.

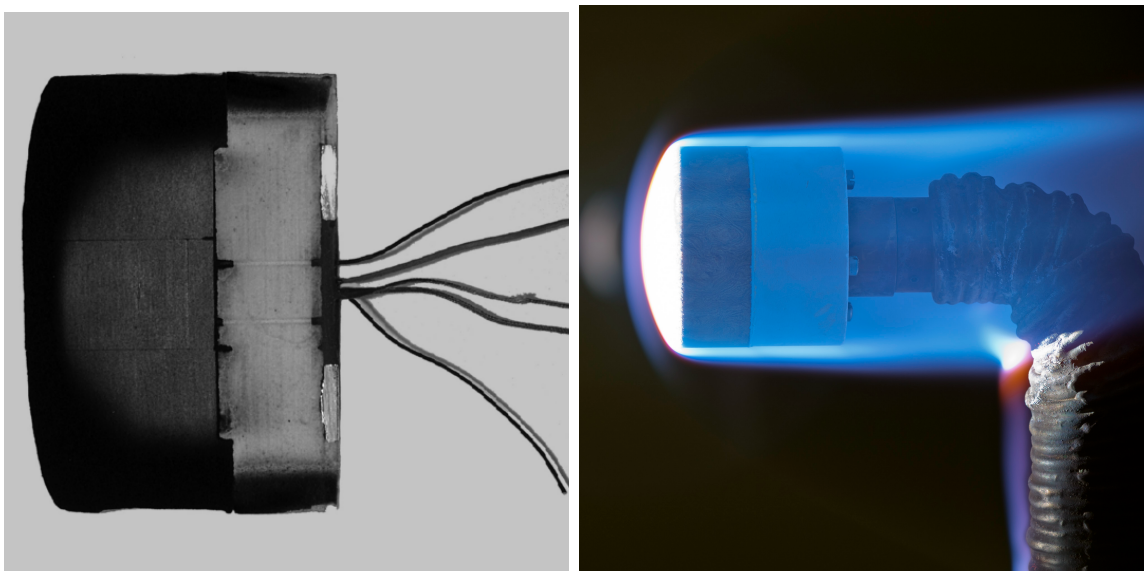

(a) Post-test iso-Q sample. Image taken from Ref. [96]

(b) Iso-Q sampple in arcjet tesing. Image taken from Ref. [97]

Figure 7.18: iso-Q sample

7.5.1 Boundary conditions and coupling process

Figure 7.19 shows the boundary conditions and computational grid used for the simulation. The front surface is subjected to a constant, uniform heat flux at $Q_w =$

7.5×10^5 W/m^2 and a constant, uniform pressure of $p = 101,325$ Pa. The back wall ($x = 0.05$ m) is assumed to be adiabatic and impermeable. The side wall ($y = 0.05$ m) is set to be adiabatic, permeable, and with a fixed pressure, $p = 101,325$ Pa, which is the same as the front surface pressure. For solid mechanical boundary conditions, the back wall ($x = 0.05$ m) is set to have a fixed support. As for the front and the side wall, they are modeled as free surfaces with no constrain. For a better computational result, the mesh is intensively refined on the front surface and side wall, where temperature gradient are expected to be large. A total of 60,000 computational cells are used for this mesh.

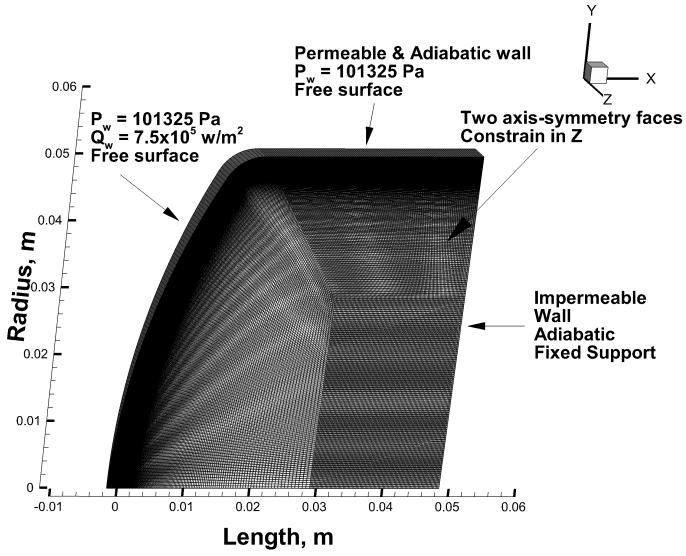

Figure 7.19: Charring ablation case for iso-Q sample

7.5.2 Results

The two-way strong coupling shows very interesting modifications of the geometry caused by thermal expansion. Figure 7.20 illustrates the displacement results, including changes of geometry. It is immediately observed that at the beginning of the simulation, when $t = 1$ s, the thermal expansion changes the geometry with a maximum displacement 0.2 mm at the edge between the front surface and the side

wall. The front surface also expands to its left with a displacement of 0.1 mm.

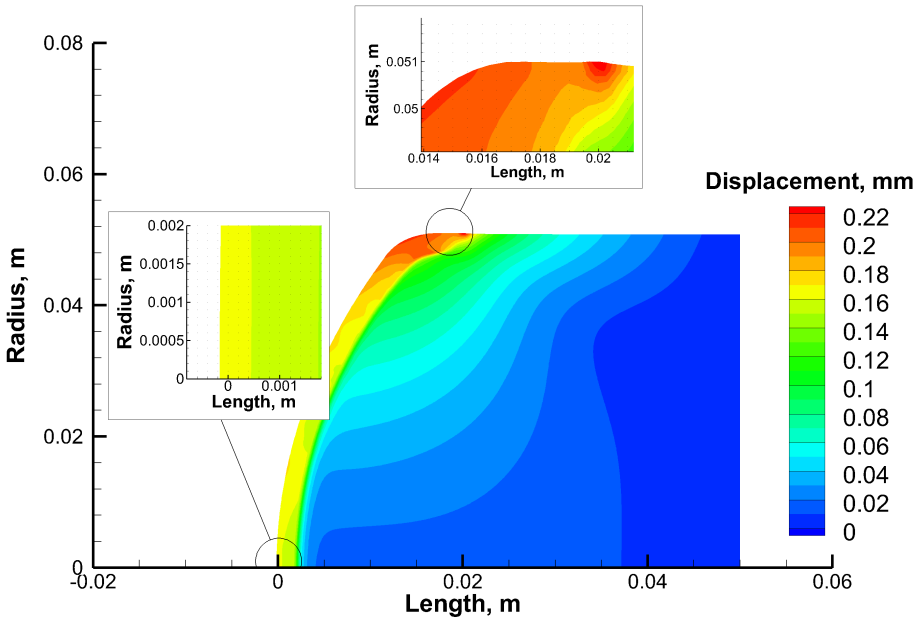

Figure 7.20: Displacement results at $t = 1$ s

Figure 7.21 provides the temperature field at $t = 1$ s. The same expansion can be observed. It should be noted that, since the material is expanding, in a realistic way, the heat flux subjected to that area should vary with the changes of the deformation. These results give more requirement on the heat flux description with a spatial correction. The value of the heat flux is fixed and uniformly subjected to the sample front surface in this case.

Figure 7.22 presents the distribution of von Mises stress within the sample. It can be observed that stress concentrates in a band area with a maximum value of 540 MPa. Since temperature is the driving force of this expansion and stress, the band area follows the same pattern of the temperature field. The expanded front surface shows little stress except at the joint area where front wall and side wall are connected. This stress concentration has been studied in previous investigation on the relationship between stress and temperature, displacement and density in Ref. [98].

Nevertheless, this type of behavior has been observed experimentally. An example

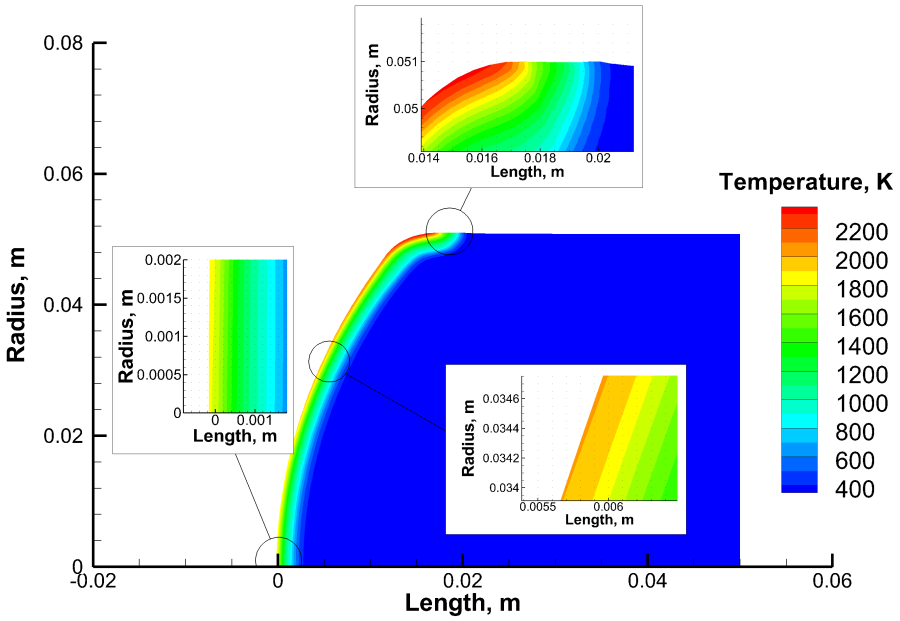

Figure 7.21: Temperature results at $t = 1$ s

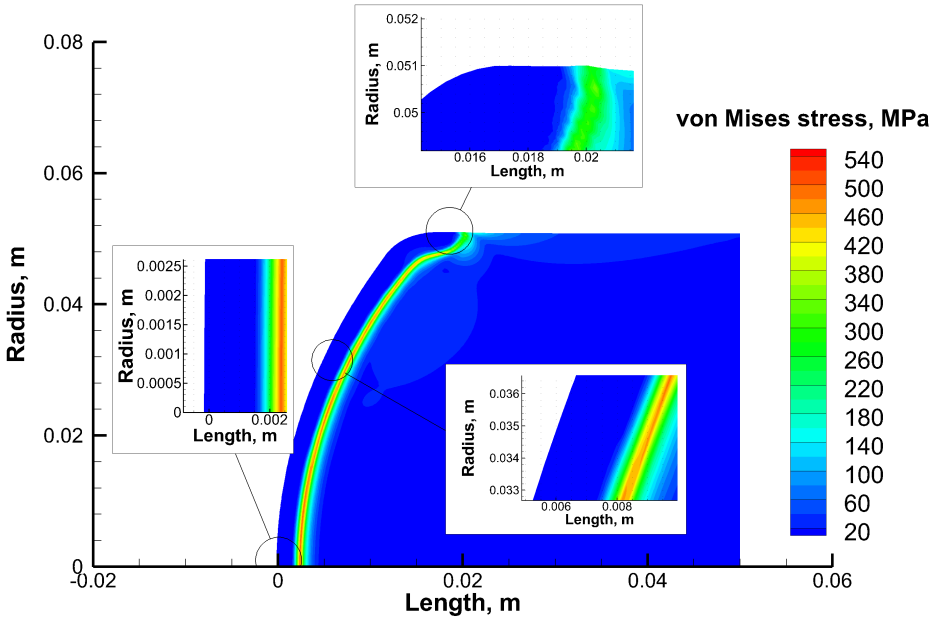

Figure 7.22: Von Mises stress results at $t = 1$ s

is shown in Fig. 7.23, where a PICA sample is being heated in an arc-jet facility at $t = 10, 17, 30$ and 59 s. It can be seen that the sample is expanding as time elapses. A very significant expansion – a "lip" – can be observed at the end of the run, at

$t = 59$ s. As the expanded material becomes weaker, it will be peeled off by shear stress on the edges, and depart the sample.

A similar behavior has also been reported in the literature when two different material are subjected to the same heating condition, but have different thermo-mechanical properties. If one material expands significantly compared to the other, the flow field on the surface can be affected. This type of behavior, called fencing, as been observed with the gap-filler used between the tiles of heat shields.[99]

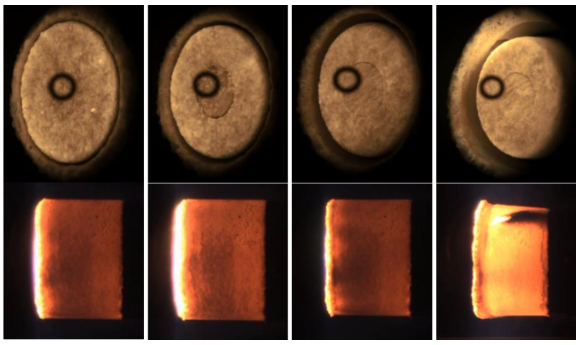

Figure 7.23: Hymets arc-jet facility testing results conducted by Martin A. et al. Image taken from Ref. [100]

7.6 Conclusion and outlook

In this study, the two-way thermo-mechanical coupling capabilities of KATS have been verified and demonstrated. Code-to-code comparison shows that the thermal expansion can be accurately predicted. 1D ablation cases shows that, grid deformation decreases the maximum temperature and smooths the distribution of the temperature. Meanwhile, strain effects on the conductivity increase the maximum value and make temperature gradient steeper or smoother for different part of the material. The results also demonstrate that for ablation modeling, thermal expansion and its impacts on the material properties should be considered.

The internal pressure test-case provides an insight into the influence of the pressure field on the stress experienced by the ablative material. Although the magnitude of

the pore pressure is not very large, under certain condition, such as a non-permeable cavity, localized stress may occur and cause damage. Finally, a two-way strong coupling for iso-Q sample shows a thermal expansion on the front surface and side wall. The deformation of the geometry leads to the formation of a "lip" that will eventually peel off, as is often seen in experimental results. The formation of this "lip" on ablative material often leads to material spallation.

The results presented here open the door for additional work on the topic. For instance, the material recession module would need to be coupled to the surface ablation computation. Or, even more interestingly, the effects of the strong coupling could be investigated using more parameters.

Chapter 8: Conclusions, Contributions and Future Work

8.1 Conclusions

This study focuses on the structural response of the TPS materials during atmospheric re-entry. In Chapter 2, mathematical foundations of thermo-mechanical coupling theories were investigated. The uniqueness of the coupled equations was proved. Discussions on inertial term and mechanical coupling term were also presented to show that in most situations, these two terms can be ignored. Based on the strict mathematical derivations, the coupled thermo-mechanical equations could then be simplified into a framework of quasi-static coupling system.

Based on the mathematical derivations, a structural response solver was developed in the Finite Volume Method in Chapter 3. Verification cases were conducted to show the accuracy and correctness of implementation of equations. Then, this solver was coupled with thermal response in KATS and applied to charring ablation problem. Results showed that, the produced thermal stress could be undesirably large up to 500 MPa, and was strongly related to temperature distribution and material properties such as the density, conductivity, CTE and Young's modulus.

Chapter 4 presented the results on the investigation of internal pressure within TPS material. The results showed that under the assumption that porous media was regarded as bulk material and isotropic properties, internal pressure played a negligible effects on stress and displacement. However, more detailed investigations were needed to study the possibility of the formation of impurity and micro-cracks in the TPS material.

Chapter 5 provided the process of development of moving mesh scheme in struc-

tural response module. The developed algorithm was based on the Finite Volume Method and was very flexible to couple with different modules. A series of demonstration cases showed the correctness of mesh handling and application cases showed the expected thermal expansion are captured.

In Chapter 6, as a continuation of the previous chapter, a 1D two-way thermo-mechanical solver was developed based on Finite Difference Method in Python. This rapidly developed code was then verified with ANSYS. By assuming a linear relationship between strain and conductivity, the strain effects was also studied to show that as the conductivity decreased, surface temperature increased and resulted in a larger local displacement. The results also revealed that the strain effects could play a major role on the temperature distribution in heat conduction since conductivity was a function of strain.

Finally in Chapter 7, as an integration of previously developed techniques and frameworks, the fully coupled two-way thermo-mechanical solver was developed. Thermal expansion and strain effect were captured during the charring ablation. The two-way results showed that the overall temperature was underestimated as well as the von Mises stress; the displacement was, however, overestimated in one-way coupling. The application case on the iso-Q sample showed that thermal expansion on the front surface and the joint area on the sample shoulder could be more easily peeled off from the sample. The geometric deformation also indicated that the geometry of the flow field should be changed according to the thermal expansion and the surface recession.

8.2 Original contributions

1. **Development of multi-dimensional structural response solver in Finite Volume Method (FVM) framework. (Chapter 2, 3)** Unlike most solid mechanics solvers which are most developed using Finite Element Method (FEM), the KATS uses an unified FVM framework. It solves either wave equa-

tions for transient problem or elliptic equations for static problem by discretization on cell centers of the computation grid . Demonstrated by the verification cases, the solver achieved equal accuracy and capability for various structural modeling problems compare to FEM. The same framework between among various components enabled KATS to be flexible enough to couple with other modules with ease.

2. **Development of thermo-mechanical coupling solver for charring ablation. (Chapter 3)** By coupling the developed structural solver with the existing thermal response solver, KATS is able to investigate thermal stress induced by high temperature and large temperature gradient within the TPS material. In a same FVM framework, a shared computation grid can be used for both codes and thus avoid multiple interpolations between cell center and cell node. Based on this coupled solver, the distribution of thermal stress is investigated for charring ablation during atmospheric re-entry. The resulted thermal stress concentrates in a banded area as ablation process continues and moves along with the ablation front. Thus, it is critical to ensure that the TPS material can withstand the stress induced by the heating process.

3. **Investigation on structural impacts of pyrolysis gas within TPS material. (Chapter 4)** Based on the same framework, the structural impacts of internal pressure induced by charring ablation pyrolysis gas are studied. Because of the isotropic material assumption, the resulted stress from internal pressure field is negligible for either permeable or impermeable walls cases. However, the investigation also reveals that the possibilities of the impurity and micro-cracks within the material and a rapidly building-up pressure, which can be disastrous for TPS material.

4. **Moving mesh scheme and two-way coupling of thermal expansion.**

(Chapter 5) Moving mesh scheme is now a necessary tool for multiphysics advanced modeling. By updating the node position using the calculated displacement on cell center, the computation grid is deformed in a physical way. Empowered by the developed moving mesh scheme, thermal expansion is captured in either a simple heat conduction problem, or charring ablation problem.

5. **Development of a 1D two-way thermo-mechanical coupling solver. (Chapter 6)** There exists very few available code can do a two-way thermo-mechanical coupling, especially for strain effects on material properties. A 1D prototype model is developed using a Finite Difference Method framework as an exploratory and verification tool. It is rapidly developed in Python with packages including Numpy and Pandas. The post-process of results are handled by Matplot for convenient visualization. The solver is verified by code-to-code comparisons among ANSYS and KATS for correct implementations of algorithm. This package is now used for verification for KATS especially for studying the strain effects on material properties.

6. **Development of a two-way thermo-mechanical coupling solver for charring ablation problem. (Chapter 7)** The developed two-way thermo-mechanical coupling solver can be regard as a collection of all the previous techniques and schemes. Geometry deformation caused by large temperature gradient is captured by moving mesh scheme and fed back to the thermal response solver. The large thermal strain, at the same time, is calculated by deformed grid and then is applied to material properties to see how it affects the overall performance. By analyzing the thermal expansion and strain effects on the charring ablative materials, the grid deformation and the thermal strain are supposed to be not negligible. It is also the first time to visualize the thermal expansion in charring ablation problems as well as the two-way strongly

coupled analysis for TPS material.

8.3 Future Work

1. **Material margin policy for TPS material.** The TPS material properties have significant impacts on both thermal and mechanical performance for atmospheric entry. As a continuation of this work, parametric studies on key properties such as the CTE, Young's modulus and Poisson ratio should be carefully investigated. Maximum allowable CTE should be examined with coupling effects on the conductivity. By doing so, a material margin policy can be established for different vehicles and various purposes. As a result, optimal material properties can be quantified to achieve a perfect balance between economy and safety.

2. **Non-linear structural response solver.** In either one-way and two-way thermal mechanical coupling studies for the charring ablation, the resulted strains are large enough so that the assumption of linear strain-stress may fail. Thus, it is necessary to develop the non-linear description on the stress-strain relation and coupled it into structural response code.

3. **Porous material model.** As showed in Chapter 4, the stress and strain caused by internal pressure are negligible if the porous material is isotropic and perfectly homogeneous with averaged, uniformly distributed pores. The reality, however, is far from these assumptions. Pores are different in sizes and the possibility of forming the local sealed chamber exists. Therefore, it is necessary to study how the internal pressure affects the TPS material if these defects exist.

Appendix

A sample input file for KATS thermo-mechanical coupling simulation is provided in the following list.

```
reference {
  Mach = 0.01;
  T    = 298;
}
time marching {
  step size = 1e-3;
  number of steps = 1000;
}
grid_1 {
        //file = plate100100.cgns;
        file = isoQ40000plate.cgns;
  //transform_1 (function = scale; anchor = [0, 0, 0]; factor = [1, 1,
    1]; );
  transform_1 (function = scale; anchor = [0, 0, 0]; factor = [1E-3, 1E
    -3, 1E-3];
    number of flaw face = 0;// one flaw face introduce two flaw cells
    number of flaw cell = 0;// one flaw cell brings multiple flaw faces
    !
    porosity = 0;// ZERO means pure solid !
    moving mesh = 1;//1 = move, 0 = noMovement !
    bcValue = 20;
  );
        equations = heat conduction;
        write output (
    volume variables = [T,rhost,rhos, p, phi, solidDisp, vonMisesStress,
    totalSolidDisp,volumeStrain,
```

```
23          youngsModulus, thermalExpansion, poissonRatio, rank, mass,
    volume];
24     surface variables = [p, rho, mdot, phi, V, T, hg, rhos, rhost,
    solidDisp];
25     volume plot frequency = 10;
26                 surface plot frequency = 400000000;
27         );
28   heat conduction (
29     // Number of ...
30     maximum iterations = 1000;
31     number of gas bulk = 1;
32     number of solid species = 3;
33     number of dimensions = 3;
34     number of energy equations = 1;
35     porous model = Weng14;//Forchheimer;//Weng15;//Suzuki04;//Weng14;//
    Ahn02//Chen13;
36   );
37   solid mechanics (
38     maximum iterations = 1500;
39     damping parameter = [0.25, 0.25, 0.];
40     convergence = 5E-6;
41     deformation magnifier = [1,1,1];
42     relaxation coefficient = 1;
43     // Number of ...
44     number of solid displacement equations = 3;
45   );
46   material = tacot/model.mat;
47     IC_1 (T = 298; solidDisp=[0, 0, 0];p = 101325;);
48   BC_3 (type = outlet;
49     p = 101325;
50     externalForce = [0, 0, 0];
51   );
52   BC_4 (type = outlet;
```

```
53      //T = 298;
54      p = 101325;
55      qdot = 7.5e5;
56      externalForce = [0, 0, 0];
57      );
58          BC_2 (type = wall;
59      //T = 298;
60      solidDisp = [0, 0, 0];
61      );
62    BC_1 (type = symmetry;
63      solidDisp = [0, 0, 0];
64      //externalForce = [0, 0, 0];
65    );
66    //BC_5 (type = symmetry;);
67  }
```

Listing 1: Sample Input File

Bibliography

[1] NASA, "Columbia Crew Survival Investigation Report," tech. rep., 2008.

[2] B.-a. Hamilton and C. Springs, "The DARPA/USAF Falcon Program Update and the SpaceX Maiden Launch, Mishap Investigation and Return to Flight," no. September, 2007.

[3] F. G. Jr and W. T. Fowlerf, "Thermal Protection System Weight Minimization for the Space Shuttle through Trajectory Optimization," *Journal of Spacecraft and Rockets*, vol. 11, no. 4, pp. 241–245, 1974.

[4] A. Bhungalia, C. Clewitt, H. Croop, and D. Brown, "Thermal Protection System (TPS) Optimization," in *Space 2004 Conference and Exhibit*, SPACE Conferences & Exposition, American Institute of Aeronautics and Astronautics, Sept 2004.

[5] Y. Wang, *Pattern Engineering for Functional Design of Tight-Fit Running Wear*. PhD thesis, The Hong Kong Polytechnic University, 2011.

[6] J. Snell, N. Glassey, S. Mockett, and K. Raynor, "Gore-tex bags versus traditional hand bandaging : A comparison of range of motion , sensation and function in healthy subjects," *Burns*, vol. 36, no. 5, pp. 722–731, 2010.

[7] A. Turchi, D. Bianchi, N. York, and F. Nasuti, "Radiation and Roughness Effects on Nozzle Thermochemical Erosion in Solid Rocket Motors," vol. 30, no. 2, 2014.

[8] J. R. Johnston, R. A. Signorezzi, and J. C. Freche, "Performance of Rocket Nozzle Materials with Several Solid Propellants," no. May 1966, 1966.

[9] U. Duzel, "The Effects of Static Aeroelasticity on the Performance of Supersonic / Hypersonic Nozzles," no. June, pp. 1–14, 2014.

[10] M. E. Ewing, T. S. Laker, and D. T. Walker, "Numerical Modeling of Ablation Heat Transfer," *Journal of Thermophysics and Heat Transfer*, vol. 27, no. 4, pp. 615–632, 2013.

[11] H. Weng, H.-B. Zhang, O. Khan, and A. Martin, "Multi-Dimensional Modeling of Charring Ablator," in *43rd AIAA Thermophysics Conference*, Fluid

Dynamics and Co-located Conferences, American Institute of Aeronautics and Astronautics, June 2012.

[12] C. A. Steeves and A. G. Evans, "Optimization of Thermal Protection Systems Utilizing Sandwich," *Journal of the American Ceramic Society*, vol. 61, 2011.

[13] C. J. Martin, "Parametric Weight Comparison of Advanced Metallic , Ceramic Tile , and Ceramic Blanket Thermal Protection Systems," no. June 2000, 2000.

[14] D. E. Glass, "Ceramic Matrix Composite (CMC) Thermal Protection Systems (TPS) and Hot Structures for Hypersonic Vehicles 1," No. March 2007, pp. 1–36, 2008.

[15] A. Science, *Thermal Management at Hypersonic Leading Edges*. PhD thesis, University of Virginia, 2013.

[16] A. Rehman, R. M. Sarviya, S. Dixit, and R. Kumar, "The Influence of Coolant Temperature on the Performance of a Four Stroke Spark Ignition Engine Employing a Dual Circuit Cooling System," *Agricultural Engineering International: the CIGR Ejournal*, vol. XII, no. x, pp. 1–10, 2010.

[17] C. A. Kluever and A. Editor, "Introduction," *Journal of Spacecraft and Rockets*, vol. 38, no. 2, pp. 294–297, 2001.

[18] D. M. Curry, "An Analysis of A Charring Ablation Thermal Protection System," tech. rep., NASA, Houston, Texas, 1965.

[19] E. W. Ungar, "Ablation Thermal Protection Systems," *Science*, vol. 158, 1967.

[20] P. O. F. Three, A. M. During, S. O. F. Long-duration, and A. Heating, "19960412 015," tech. rep., NASA, Hampton, VA, 1967.

[21] R. D. Patton, C. U. P. Jr, L. Wang, J. R. Hill, and A. Day, "Ablation , mechanical and thermal conductivity properties of vapor grown carbon fiber / phenolic matrix composites," *Composites: Part A*, vol. 33, 2002.

[22] B. A. Boley and J. H. Weiner, *Theory of Thermal Stress*. John Wiley & Sons, Inc., 1960.

[23] N. Winya, S. Chankapoe, and C. Kiriratnikom, "Ablation , Mechanical and Thermal Properties of Fiber / Phenolic Matrix Composites," *International Journal of Chemical, Molecular, Nuclear, Materials and Metallurgical Engineering*, vol. 6, no. 9, pp. 875–878, 2012.

[24] W. T. Engelke, C. M. Pyron, Jr. and C. D. Pears, "Thermophysical Properties of A Low-Density Phenolic-Nylon Ablation Material," tech. rep., Langley Research Center, 1967.

[25] G. D. Zhou and T. H. Yi, "A summary review of correlations between temperatures and vibration properties of long-span bridges," *Mathematical Problems in Engineering*, vol. 2014, 2014.

[26] S. Ahmad, N. Mandal, G. Chattopadhyay, and J. Powell, "Development of a unified railway track stability management tool to enhance track safety," *Proceedings of the Institution of Mechanical Engineers, Part F: Journal of Rail and Rapid Transit*, vol. 227, no. 5, pp. 493–516, 2013.

[27] W. F. McMichael and E. Al., "Automotive Emissions after Hot and Cold Starts in Summer and Winter," *Japca*, vol. 2470, no. June, 1966.

[28] A. Martin and I. Boyd, "Implicit Implementation of Material Response and Moving Meshes for Hypersonic Re-entry Ablation," in *47th AIAA Aerospace Sciences Meeting including The New Horizons Forum and Aerospace Exposition*, Aerospace Sciences Meetings, American Institute of Aeronautics and Astronautics, Jan 2009.

[29] B Prakash, "Metallurgy of Iron and Steel Making and Blacksimthy in Ancient India," 1991.

[30] F. H. Koenemann, "Cauchy's stress theory in a modern light," *European Journal of Physics*, vol. 35, p. 015010, 2014.

[31] R. B. Hetnarski and M. R. Eslami, "Thermal stresses - Advanced theory and applications," *Solid Mechanics and its Applications*, vol. 158, pp. 1–591, 2009.

[32] T. Belytschko, R. Gracie, and G. Ventura, "A review of extended/generalized finite element methods for material modeling," *Modelling Simul. Mater. Sci. Eng. Mater. Sci. Eng*, vol. 17, no. 17, pp. 43001–24, 2009.

[33] J. N. Reddy, *An introduction to nonlinear finite element analysis*. Oxford University Press, USA, illustrate ed., 2004.

[34] ANSYS, "ANSYS® Academic Research, Release 16.2," 2015.

[35] ALTASIM, "COSMOL Structural Mechanics," 2015.

[36] MSC-Software, "MSC Nastran 2016 Reference Manual," 2016.

[37] T. D. Kostka and J. A. Templeton, "Coupled Thermomechanical Modeling using Dissimilar Geometries in Arpeggio," tech. rep., 2010.

[38] Langley Research Center, "Thermophysical Properties of Six Charring Ablators from 140 K to 700 K and Two Chars from 800 to 3000 K," vol. 4, no. October, 1965.

[39] William L. Ko and Jerald M.Jenikins, "Thermal Stress Analysis of Space Shuttle Orbiter Wing Skin Panel and Thermal Protection System," no. March 1987, 2017.

[40] Abaqus, "Abaqus," 2015.

[41] W. H. Ng, P. P. Friedmann, and A. M. Waas, "Thermomechanical analysis of a thermal protection system with defects and heat shorts," *Collection of Technical Papers - AIAA/ASME/ASCE/AHS/ASC Structures, Structural Dynamics and Materials Conference*, vol. 10, no. May, pp. 7363–7385, 2006.

[42] M. A. Biot, "Theory of Propagation of Elastic Waves in a Fluid-Saturated Porous Solid. I. Low-Frequency Range," vol. 28, no. 2, pp. 168–178, 1956.

[43] M. a. Biot, "Theory of Propagation of Elastic Waves in a FluidSaturated Porous Solid. II. Higher Frequency Range," *J. Acoust. Soc. Am.*, vol. 28, no. 2, pp. 168–178, 1956.

[44] Q. Yang, S. Meng, W. Xie, H. Jin, C. Xu, and S. Du, "Effective mitigation of the thermal short and expansion mismatch effects of an integrated thermal protection system through topology optimization," *Composites Part B: Engineering*, vol. 118, pp. 149–157, 2017.

[45] P. G. Cross and I. D. Boyd, "Two-Dimensional Modeling of Ablation and Pyrolysis with Application to Rocket Nozzles," vol. 54, no. June, pp. 1–27, 1900.

[46] L. Chauvin, R. Erb, D. Greenshields, J. E. Pavlosky, and C. L. Statham, "Apollo thermal-protection system development," *Journal of Spacecraft and Rockets*, vol. 7, no. 6, pp. 727–734, 1970.

[47] W. H. Bowman and R. M. Lawrence, "Ablative materials for high-temperature thermal protection of space vehicles," *Journal of Chemical Education*, vol. 48, pp. 690–691, Oct 1971.

[48] r. S. C. Davuluri, A. Martin, H. Zhang, and A. Martin, "Numerical study of spallation phenomenon in an arc-jet environment," in *11th AIAA/ASME Joint Thermophysics and Heat Transfer Conference*, AIAA Aviation, pp. 1–10, American Institute of Aeronautics and Astronautics, June 2014.

[49] A. Martin, S. C. C. Bailey, F. Panerai, R. S. C. Davuluri, A. R. Vazsonyi, H. Zhang, Z. S. Lippay, N. N. Mansour, J. A. Inman, B. F. Bathel, S. C. Splinter, and P. M. Danehy, "Numerical and experimental analysis of spallation phenomena," *CEAS Space Journal*, vol. 8, Sept 2016.

[50] J. H. Lundell, "Spallation of the Galileo Probe Heat Shield," in *AIAA/ASME 3rd Joint Thermophysics and Heat Transfer Conference*, AIAA Paper 82-0852, (St. Louis, MO), Jan 1982.

[51] R. D. Mathieu, "Mechanical Spallation of Charring Ablators in Hyperthermal Environments," *AIAA Journal*, vol. 2, pp. 1621–1627, Sept 1964.

[52] C. Park, "Stagnation Region Heating Environment of Galileo Probe," in *40th AIAA Thermophysics Conference*, AIAA Paper 2008-4109, (Seattle, WA), June 2008.

[53] F. S. Milos, M. J. Gasch, and D. K. Prabhu, "Conformal Phenolic Impregnated Carbon Ablator (C-PICA) Arcjet Testing, Ablation and Thermal Response," in *53rd AIAA Aerospace Sciences Meeting*, AIAA Paper 2015-1448, (Kissimmee, FL), Jan 2015.

[54] H. K. Tran, C. E. Johnson, D. J. Rasky, F. C. L. Hui, M. T. Hsu, T. Chen, Y.-K. Chen, D. Paragas, and L. Kobayashi, "Phenolic Impregnated Carbon Ablators (PICA) as Thermal Protection Systems for Discovery Missions," Technical Memorandum NASA-TM-110440, NASA Ames Research Center, Moffett Field, CA, April 1997.

[55] D. R. Jenkins, "Protecting the Body: The Orbiter's Thermal Protection System," in *Space Shuttle Legacy*, Library of Flight, pp. 111–135, American Institute of Aeronautics and Astronautics, Inc., Jan 2013.

[56] J. M. Corum, R. L. Battiste, K. C. Liu, and M. B. Ruggles, "Basic Properties of Reference Crossply Carbon-Fiber Composite," Technical Report ORNL/TM-2000/29, Oak Ridge National Lab., 2000.

[57] P. Agrawal, J. F. Chavez-Garcia, and J. Pham, "Fracture in Phenolic Impregnated Carbon Ablator," *Journal of Spacecraft and Rockets*, vol. 50, pp. 735–741, June 2013.

[58] P. Agrawal, D. K. Prabhu, T. H. Squire, F. S. Milos, and M. Stackpoole, "Investigation of Performance Envelope for Phenolic Impregnated Carbon Ablator (PICA)," *54th AIAA Aerospace Sciences Meeting, AIAA Paper*, Jan.

[59] H. L. N. Mcmanus and G. S. Springer, "High Temperature Thermomechanical Behavior of Carbon-Phenolic and Carbon-Carbon Composites, I. Analysis," *Journal of Composite Materials*, vol. 26, pp. 206–229, Jan 1992.

[60] A. J. Amar, B. F. Blackwell, and J. R. Edwards, "Development and Verification of a One-Dimensional Ablation Code Including Pyrolysis Gas Flow," *Journal of Thermophysics and Heat Transfer*, vol. 23, no. 1, pp. 59–71, 2009.

[61] A. J. Amar, B. F. Blackwell, and J. R. Edwards, "One-Dimensional Ablation Using a Full Newton's Method and Finite Control Volume Procedure," *Journal of Thermophysics and Heat Transfer*, vol. 22, pp. 72–82, Jan 2008.

[62] J. Schijve, *Fatigue of structures and materials*. 2009.

[63] G. C. Jacob, J. M. Starbuck, J. F. Fellers, S. Simunovic, and R. G. Boeman, "Strain rate effects on the mechanical properties of polymer composite materials," *Journal of Applied Polymer Science*, vol. 94, pp. 296–301, Sept 2004.

[64] S. Bakhshian and M. Sahimi, "Computer simulation of the effect of deformation on the morphology and flow properties of porous media," *Physical Review E*, vol. 94, p. 42903, Oct 2016.

[65] M. E. Ewing and B. Pincock, "Heat Transfer Modeling of a Charring Material Using Isoconversional Kinetics," *Heat Transfer Engineering*, vol. 38, no. 13, 2017.

[66] P. Schrooyen, K. Hillewaert, T. E. Magin, and P. Chatelain, "Fully implicit Discontinuous Galerkin solver to study surface and volume ablation competition in atmospheric entry flows," *International Journal of Heat and Mass Transfer*, vol. 103, pp. 108–124, Dec 2016.

[67] J. Lachaud and N. N. Mansour, "Porous-Material Analysis Toolbox Based on OpenFOAM and Applications," *Journal of Thermophysics and Heat Transfer*, vol. 28, pp. 191–202, April 2014.

[68] A. J. Amar, B. Oliver, B. Kirk, G. Salazar, and J. Droba, "Overview of the CHarring Ablator Response (CHAR) Code," in *46th AIAA Thermophysics Conference*, AIAA Aviation, American Institute of Aeronautics and Astronautics, June 2016.

[69] F. S. Milos, M. J. Gasch, and D. K. Prabhu, "Conformal Phenolic Impregnated Carbon Ablator (C-PICA) Arcjet Testing, Ablation and Thermal Response," *Journal of Spacecraft and Rockets*, vol. 52, pp. 804–812, May 2015.

[70] H. Weng, S. C. C. Bailey, and A. Martin, "Numerical study of iso-Q sample geometric effects on charring ablative materials," *International Journal of Heat and Mass Transfer*, vol. 80, pp. 570–596, Jan 2015.

[71] H. Weng and A. Martin, "Multidimensional modeling of pyrolysis gas transport inside charring ablative materials," *Journal of Thermophysics and Heat Transfer*, vol. 28, no. 4, pp. 583–597, 2014.

[72] H. Weng and A. Martin, "Numerical Investigation of Thermal Response Using Orthotropic Charring Ablative Material," *Journal of Thermophysics and Heat Transfer*, vol. 29, pp. 429–438, Jan 2015.

[73] A. Martin and I. D. Boyd, "Non-{D}arcian behavior of pyrolysis gas in a thermal protection system," *Journal of Thermophysics and Heat Transfer*, vol. 24, no. 1, pp. 60–68, 2010.

[74] A. Amar, N. Calvert, and B. Kirk, "Development and Verification of the Charring Ablating Thermal Protection Implicit System Solver," in *49th AIAA Aerospace Sciences Meeting including the New Horizons Forum and Aerospace Exposition*, Aerospace Sciences Meetings, American Institute of Aeronautics and Astronautics, Jan 2011.

[75] Z. Cai, J. E. Jones, S. F. McCormick, and T. F. Russell, "Control volume mixed finite element methods," *Computational Geosciences*, vol. 1, no. 3, pp. 289–315, 1997.

[76] J. E. Wiebenga, *High-Fidelity Material Response Modeling as Part of an Aerothermoelastic Framework for Hypersonic Flows*. PhD thesis, 2014.

[77] I. Bijelonja, I. Demirdžić, and S. Muzaferija, "A finite volume method for incompressible linear elasticity," *Computer Methods in Applied Mechanics and Engineering*, vol. 195, pp. 6378–6390, Sept 2006.

[78] I. Demirdžić and S. Muzaferija, "Numerical method for coupled fluid flow, heat transfer and stress analysis using unstructured moving meshes with cells of arbitrary topology," *Computer Methods in Applied Mechanics and Engineering*, vol. 125, no. 1-4, pp. 235–255, 1995.

[79] N. A. Fallah, C. Bailey, M. Cross, and G. A. Taylor, "Comparison of finite element and finite volume methods application in geometrically nonlinear stress analysis," *Applied Mathematical Modelling*, vol. 24, pp. 439–455, June 2000.

[80] H. Jasak and H. G. Weller, "Application of the Finite Volume Method and Unstructured Meshes to Linear Elasticity," *Int. J. Numer. Meth. Engng*, vol. 48, no. July 1999, pp. 267–287, 2000.

[81] A. J. Culler, A. R. Crowell, and J. J. Mcnamara, "Studies on Fluid-Structural Coupling for Aerothermoelasticity in Hypersonic Flow," *AIAA Journal*, vol. 48, no. May, pp. 1721–1738, 2009.

[82] H. Zhang, *High Temperature Flow Solver For Aerothermodynamics Problems*. Ph.d. thesis, University of Kentucky, Lexington, KY, jul 2015.

[83] Z. Li, H. Zhang, J. B. Hoagg, S. C. C. Bailey, and A. Martin, "Turbulence Simulation Using Direct Gradient Adaptive k-ω Model," in *54th AIAA Aerospace Sciences Meeting*, AIAA Paper 2016-0587, (San Diego, CA), Jan 2016.

[84] Z. Li, H. Zhang, S. C. C. Bailey, J. B. Hoagg, and A. Martin, "A Data-Driven RANS k-ω approach for modeling turbulent flows," *Journal of Computational Physics*, vol. 345, pp. 111–131, Sept 2017.

[85] G. Karypis and V. Kumar, "A Fast and Highly Quality Multilevel Scheme for Partitioning Irregular Graph," *SIAM Journal on Scientific Computing*, vol. 20, no. 1, pp. 359–392, 1998.

[86] E. G. Bosilca, G. E. Fagg, George, , Jeffrey, T. Angskun, J. J. Dongarra, M. S. Kambadur, V. Sahay, Prabhanjan, , Ralph, B. Barrett, A. Lumsdaine, H. C. Graham, D. J. Daniel, R. L., Woodall, and T. S., "Open MPI: Goals, Concept, and Design of a Next Generation MPI Implementation," 2004.

[87] R. J. LeVeque, *Finite Volume Methods for Hyperbolic Problems*. Cambridge, United Kingdom: Cambridge University Press, 2002.

[88] B. Lachaud, J., Martin, A., Cozmuta, I., and Laub, "Ablation test-case series #1," *4th AFOSR/SNL/NASA Ablation Workshop*, no. Albuquerque, NM,, 2010.

[89] C. Pradere and C. Sauder, "Transverse and longitudinal coefficient of thermal expansion of carbon fibers at high temperatures (300 to 2500K)," *Carbon*, vol. 46, pp. 1874–1884, nov 2008.

[90] COMSOL, "The Structural Mechanics Module User's Guide," no. 1215, pp. 137–150, 2012.

[91] R. S. C. Davuluri, H. Zhang, and A. Martin, "Numerical Study of Spallation Phenomenon in an Arc-Jet Environment," *Journal of Thermophysics and Heat Transfer*, vol. 30, no. 1, pp. 32–41, 2016.

[92] J. Scoggins and H. Hassan, "Pyrolysis Mechanism of PICA," in *10th AIAA/ASME Joint Thermophysics and Heat Transfer Conference*, Fluid Dynamics and Co-located Conferences, American Institute of Aeronautics and Astronautics, June 2010.

[93] J. Lachaud, T. E. Magin, I. Cozmuta, and N. N. Mansour, "A SHORT REVIEW OF ABLATIVE-MATERIAL RESPONSE MODELS AND SIMULATION TOOLS,"

[94] A. Rashid and N. Strömberg, "Sequential simulation of thermal stresses in disc brakes for repeated braking," *Proceedings of the Institution of Mechanical Engineers, Part J: Journal of Engineering Tribology*, vol. 227, no. 8, pp. 919–929, 2013.

[95] R. Fu, H. Weng, J. Wenk, and A. Martin, "Application of A New Thermal-Mechanical Coupling Solver for Ablation," in *AIAA Aviation 2016*, no. June, p. 4432, 2016.

[96] M. A. Covington, J. M. Heinemann, H. E. Goldstein, Y. K. Chen, I. Terrazas-Salinas, J. A. Balboni, J. Olejniczak, and E. R. Martinez, "Performance of a Low Density Ablative Heat Shield Material," *Journal of Spacecraft and Rockets*, vol. 45, no. 2, pp. 237–247, 2008.

[97] NASA, "Arc Test of IsoQ model," 2014.

[98] R. Fu, H. Weng, J. F. Wenk, and A. Martin, "Thermomechanical Coupling for Charring Ablators," *Journal of Thermophysics and Heat Transfer*, pp. 1–11, Oct 2017.

[99] A. Alunni and T. Gokcen, "Assessment of Fencing on the Orion Heatshield," *46th AIAA Thermophysics Conference*, no. June, pp. 1–6, 2016.

[100] B. D. Butler, M. Winter, F. Panerai, A. Martin, S. C. Bailey, M. Stackpoole, P. M. Danehy, and S. Splinter, "Characterization of Candidate Materials for Remote Recession Measurements of Ablative Heat Shield Materials," in *54th AIAA Aerospace Sciences Meeting*, (San Diego, California), AIAA Paper, 2016-1516, 2016.

Rick Fu

Education

- Ph.D. in Mechanical Engineering, University of Kentucky, August 2012 - Current
- B.Sc. in Thermal Energy & Power Engineering, Xihua University, August 2007 - June 2011

Professional Experience

Private Equity Fund - ***Contract Quantitatve Developer & Analyst***

Quantitative Research July 2017 - Current

Infrastructure Development January 2017 - Current

Xihua University - ***Research Assistant***

Numerical Modeling of Diesel Particulate Filter June 2011 - July 2012

Academic Research

Advanced Modeling for Thermal Protection System February 2017 - July 2017

- Developed adaptive meshing approach (C++) to model the material loss during re-entry ablation process.
- Developed a new grid labeling algorithm in a Finite Volume Method framework to better represent the porous material structure.
- Coupled this algorithm into thermo-mechanical solver for more simulation and research purposes.

Two-way Strong Coupling for Re-entry Space Vehicle June 2016 - January 2017

- Developed and coded massively paralleled advanced algorithm (C++) to analyze the thermal stress and expansion of space vehicle heat shield.
- Improved the accuracy and fidelity of the modeling by creatively transferring grid deformation and strain effects among different modules.
- Incorporated this algorithm into the existing software framework with flexibility and consistency.

Thermo-Mechanical Coupling for Space Vehicle Heat Shield May 2015 - October 2015

- Developed, verified and implemented advanced high-fidelity algorithm (C++) for space vehicle heat shield.
- Massively paralleled this algorithm in HPC cluster to run at 128+ cores simultaneously.
- Estimated mission risk by assessing thermal stress and expansion due to extreme heating.

Publications

Journal Articles

- Omidy, A. D., Cooper, J. M., Fu, R., Weng, H., and Martin, A., "VISTA, An Open-Source Material Model for Avcoat," Journal of Spacecraft and Rockets, 2017, Submitted.
- Fu, R., Weng, H., Wenk, J. F., , and Martin, A., "Thermo-mechanical coupling for charring ablators," Journal of Thermophysics and Heat Transfer, 2017, In press.
- Fu, R., Weng, H., Wenk, J. F., , and Martin, A., "Two-way coupled thermo-mechanical solver for ablation problems," Journal of Thermophysics and Heat Transfer, 2017, In preparation.

Conference Articles

- Omidy, A. D., Cooper, J. M., Fu, R., Weng, H., and Martin, A., "Development Of An Open-Source Avcoat Material Database, VISTA," 47th AIAA Thermophysics Conference, AIAA Paper 2017-3356, Denver, CO, June 2017.
- Fu, R., Weng, H., Wenk, J. F., and Martin, A., "Development of a Coupled Elastic Solver for Ablation Problems," 55th AIAA Aerospace Sciences Meeting and Exhibit, AIAA Paper 2017-0439, Grapevine, TX, 01 2017.